EFFECTS OF LOADING RATE ON TRIAXIAL COMPRESSIVE STRENGTH AND DEFORMABILITY OF ROCK SALT UNDER ELEVATED TEMPERATURES

Komkrit Phatthaisong

A Thesis Submitted in Partial Fulfillment of the Requirements for the Degree of Doctor of Philosophy of Engineering in Geotechnology

Suranaree University of Technology

Academic Year 2014

ผลกระทบของอัตราการให้แรงกดต่อความแข็งและการเปลี่ยนแปลงรูปร่างในสามแกนของเกลือหินภายใต้อุณหภูมิสูง

นายคมกริช ผาดไธสง

วิทยานิพนธ์นี้เป็นส่วนหนึ่งของการศึกษาตามหลักสูตรปริญญาวิศวกรรมศาสตรดุษฎีบัณฑิต
สาขาวิชาเทคโนโลยีธรณี
มหาวิทยาลัยเทคโนโลยีสุรนารี
ปีการศึกษา 2557

EFFECTS OF LOADING RATE ON TRIAXIAL COMPRESSIVE STRENGTH AND DEFORMABILITY OF ROCK SALT UNDER ELEVATED TEMPERATURES

Suranaree University of Technology has approved this thesis submitted in partial fulfillment of the requirements for the Degree of Doctor of Philosophy.

Thesis Examining Committee

_____

(Dr. Decho Phueakphum)

Chairperson

_____

(Prof. Dr. Kittitep Fuenkajorn)

Member (Thesis Advisor)

_____

(Dr. Prachya Tepnarong)

Member

_____

(Dr. Anisong Chitnarin)

Member

_____

(Assoc. Prof. Ladda Wannakao)

Member

_____ _____

(Prof. Dr. Sukit Limpijumnong) (Assoc. Prof. Flt. Lt. Dr. Kontorn Chamniprasart)

Vice Rector for Academic Affairs and Innovation

Dean of Institute of Engineering

คมกริช ผาดไธสง : ผลกระทบของอัตราการให้แรงกดต่อความแข็งและการเปลี่ยนแปลงรูปร่างในสามแกนของเกลือหินภายใต้อุณหภูมิสูง (EFFECTS OF LOADING RATE ON TRIAXIAL COMPRESSIVE STRENGTH AND DEFORMABILITY OF ROCK SALT UNDER ELEVATED TEMPERATURES) อาจารย์ที่ปรึกษา : ศาสตราจารย์ ดร.กิตติเทพ เฟื่องขจร, 100 หน้า.

วัตถุประสงค์ของงานวิจัยเพื่อศึกษาผลกระทบของอัตราการให้แรงต่อกำลังรับแรงกดและการเปลี่ยนแปลงรูปร่างของเกลือหินภายใต้อุณหภูมิ 303 ถึง 473 เคลวิน การทดสอบกำลังรับแรงกดได้ใช้ตัวอย่างเกลือหินจากเกลือชั้นล่าง ของเกลือหินชุดมหาสารคราม โดยใช้อัตราการกดอยู่ระหว่าง 0.001 ถึง 0.1 เมกกะปาสคาลต่อวินาที ภายใต้ความดันล้อมรอบ 0 ถึง 12 เมกกะปาสคาล ผลการศึการะบุว่าค่าสัมประสิทธิ์ความยืดหยุ่นและกำลังรับแรงกดเพิ่มตามอัตราการกดและลดลงเมื่ออุณหภูมิเพิ่มขึ้น เกณฑ์การแตกในหลายแกนได้ถูกพัฒนาขึ้น โดยมีการรวมผลกระทบของอัตราการกดและอุณหภูมิเข้าอยู่ในสูตร ผลการศึกษาระบุว่าโพรงกักเก็บในชั้นเกลือหินที่ความลึก 500 เมตร การจำลองถูกดำเนินการภายใต้วัฏจักร 1 รอบต่อเดือน ถึง 6 รอบต่อปี เกณฑ์การแตกพลังงานความเครียดเบี่ยงเบนในฟังก์ชั่นของพลังงานความเครียดเฉลี่ยที่พิจารณาความเค้นและความเครียดแล้วผลรวมที่จุดบวมตัวของเกลือหินจะให้ผลในเชิงอนุรักษ์มากที่สุด เมื่อเปรียบเทียบเกณฑ์การแตกเดิมที่ใช้ออกแบบที่ไม่พิจารณา ผลกระทบของอัตราการกดและอุณหภูมิ

สาขาวิชา เทคโนโลยีธรณี ลายมือชื่อนักศึกษา _____

ปีการศึกษา 2557 ลายมือชื่ออาจารย์ที่ปรึกษา_____

KOMKRIT PHATTHAISONG : EFFECTS OF LOADING RATE ON TRIAXIAL COMPRESSIVE STRENGTH AND DEFORMABILITY OF ROCK SALT UNDER ELEVATED TEMPERATURES. THESIS ADVISOR : PROF. KITTITEP FUENKAJORN, Ph.D., P.E., 107 PP.

ROCK SALT/STRAIN ENERGY/TRIAXIAL/SHEAR STRESS/WITHDRAWAL RATES/SALT CAVERNS

The objective of this study is to experimentally determine the effects of loading rate on triaxial compressive strengths and deformability of rock salt under temperatures of up to 473 K. The compression tests have been performed on the Lower Salt member of the Maha Sarakham salt using a polyaxial load frame with the loading rates ranging from 0.001 to 0.1 MPa/s and confining pressures up to 12 MPa. The results indicate that the salt elasticity and strength increase with the loading rates and decrease with temperatures. Various multi-axial formulations of loading rate and temperature dependent strength and deformability are derived. Based on this study, the storage caverns at 500 m depth should be operated under 1 cycle/month up to 6 cycles/year. The strain energy criterion that considers both distortional and mean stress-strains at dilation tends to give the most conservative results as compared to the conventional design where the effects of loading rate and temperature have never been considered.

School of Geotechnology Student's Signature_____

Academic Year 2014 Advisor's Signature_____

ACKNOWLEDGMENTS

I wish to acknowledge the funding support from Suranaree University of Technology (SUT).

I would like to express my sincere thanks to Prof. Dr. Kittitep Fuenkajorn, thesis advisor, who gave a critical review and constant encouragement throughout the course of this research. Further appreciation is extended to Dr. Decho Phueakphum : Chairman, School of Geotechnology, Prof. Dr. Kittitep Fuenkajorn, thesis advisor, School of Geotechnology, Dr. Anisong Chitnarin, School of Geotechnology, Dr. Prachya Tepnarong, School of Geotechnology, Suranaree University of Technology (SUT) and Assoc. Prof. Ladda Wannakao, Department of Geotechnology, Faculty of Technology, Khon Kaen Unviersity (KKU) who are member of my examination committee. Grateful thanks are given to all staffs of Geomechanics Research Unit, Institute of Engineering who supported my work.

Finally, I most gratefully acknowledge my parents and friends for all their supported throughout the period of this study.

Komkrit Phatthaisong

TABLE OF CONTENTS

Page

TABLE OF CONTENTS (Continued)

Page

TABLE OF CONTENTS (Continued)

Page

LIST OF TABLES

Table **Page**

LIST OF TABLES (Continued)

Table **Page**

LIST OF FIGURES

Figure **Page**

LIST OF FIGURES (Continued)

Figure **Page**

SYMBOLS AND ABBREVIATIONS

$\partial\sigma_1/\partial t$	=	Loading rates
σ_1	=	Major principal stress
σ_2	=	Intermediate principal stress
σ_3	=	Minor principal stress
σ_m	=	Mean stress
ε_1	=	Major principal strains
ε_2	=	Intermediate principal strains
ε_3	=	Minor principal strains
ε_m	=	Mean strains
$\tau_{oct,f}$	=	Octahedral shear stresses at failure
$\gamma_{oct,f}$	=	Octahedral shear strains at failure
$\tau_{oct,d}$	=	Octahedral shear stresses at dilation
$\gamma_{oct,d}$	=	Octahedral shear strains at dilation
E, E_1	=	Elastic modulus
E_2	=	Spring constant in visco-elastic phase
η_1	=	visco-plastic coefficient in steady-state phase
η_2	=	visco-elastic coefficient in transient phase
ν	=	Poisson's ratio
G	=	Shear modulus

SYMBOLS AND ABBREVIATIONS (Continued)

$\partial\tau_{oct}/\partial t$	=	Octahedral shear stress rate
W_d	=	Distortional strain energy
W_m	=	Mean strain energy
T	=	Absolute temperature
t	=	Time
α	=	Empirical constant for equation (6.2)
α'	=	Empirical constant for equation (6.3)
β	=	Empirical constant for equation (6.4)
β'	=	Empirical constant for equation (6.5)
κ	=	Empirical constant for equation (6.2)
κ'	=	Empirical constant for equation (6.3)
λ	=	Empirical constant for equation (6.2)
λ'	=	Empirical constant for equation (6.3)
ψ	=	Empirical constant for equation (6.4)
ψ'	=	Empirical constant for equation (6.5)
δ	=	Empirical constant for equation (6.2)
δ'	=	Empirical constant for equation (6.3)
ω	=	Empirical constant for equation (6.4)
ω'	=	Empirical constant for equation (6.5)
η	=	Empirical constant for equation (6.4)
η'	=	Empirical constant for equation (6.5)

SYMBOLS AND ABBREVIATIONS (Continued)

ι	=	Empirical constant for equation (6.4)
ι′	=	Empirical constant for equation (6.5)

CHAPTER I

INTRODUCTION

1.1 Background and rationale

Temperature exerts an effect on deformability and strength of rocks. It has been found that rock strength and elastic properties decrease as the temperature increases (Shimada and Liu 2000). Studies on the temperature effect on rock salt have focused on the time-dependent deformation where the results are specifically applied to assess the long-term performance of nuclear waste repositories. Several complex formulations have been proposed to describe the thermomechanical behaviour of rock salt under the repository environments. Such formulations require several material parameters that are difficult to obtain, making their applications unpractical for the mining industry. In addition, experimental and theoretical studies on the effect of temperature on rock salt strength have been rare. Such knowledge is necessary for the design and stability analysis of salt around compressed-air and natural gas storage caverns. During injection period a storage cavern may subject to temperatures as high as 140 °C (414 K), depending on the injection rate and the maximum storage volume and pressure.

1.2 Research objectives

The objective of this study is to laboratory determine the effect of stress rate on the triaxial compressive strength and deformability of rock salt under temperatures of 303, 343, 373, 423 and 473 K. This selected range of testing temperatures covers

those likely occurred around the storage caverns under operation. Uniaxial and triaxial compression tests are performed on the Maha Sarakham salt using a polyaxial load frame (Fuenkajorn and Kenkhunthod, 2010). The stress rates are from 0.001 to 0.1 MPa/s and confining pressures from 0 to 12 MPa. Mathematical relationships between the salt strength, deformability, loading rate and temperatures are derived from the test data. Multi-axial empirical criteria that can take loading rate effect into consideration are proposed to describe the dilation and failure of the salt.

1.3 Research methodology

The research methodology shown in Figure 1.1 comprises 7 steps; including literature review, sample preparation, Triaxial loading rate under various temperatures, Derivation of the Relationships between Thermal and Loadings Rate with Salt Behavior, computer simulation, discussions and conclusions and thesis writing.

1.3.1 Literature review

Literature review is carried out to study the previous researches on effect of loading rate testing of rock under confining pressure and effect of temperature of salt knowledge. The sources of information are from text books, journals, technical reports and conference papers. A summary of the literature review will be given in the thesis.

1.3.2 Sample preparation

Rock samples used here have been obtained from the Maha Sarakham formation in the northeastern Thailand. The rock salt is relatively pure halite. Sample preparation will be carried out in the laboratory at the Suranaree University of

Technology. Samples prepared for Triaxial loading rate under various temperatures are 5.8×5.8×5.8 cm^3.

1.3.3 Triaxial tests under various temperatures and loading rates

The laboratory testing is divided into two groups; i.e. uniaxial compressive strength and triaxial compressive strength tests. The rock strengths and elasticity are determined in the laboratory under various loading rates ranging from 0.001, 0.01, 0.1, to 1 MPa per second with the confining pressures varying from 0, 3, 7 to 12 MPa and temperature varying from 303 , 343 ,373, 423 to 473 K. The sample preparation, test methods and calculation follow relevant ASTM standard practices, as much as practical. The elastic modulus and compressive strength are determined.

1.3.4 Derivation of the relationships between thermal and loadings rate with salt behavior

The mathematical relationship between the rock mechanical properties, the loading rate and temperatures are determined. A strength criterion with loading rate parameters is developed from the test results for use to predict the rock strengths and deformations that are subjected to the three-dimensioned stress under in-situ condition.

1.3.5 Computer simulations

Computer simulation describes an application of the rate-dependent dilation criteria derived earlier. They are used to determine the safe maximum withdrawal rate of a storage caverns in the Maha Sarakham salt formation under temperatures. The finite difference program FLAC (Itasca, 1992) is used in the simulations of the single isolated cavern in axial symmetry. The principal stresses and

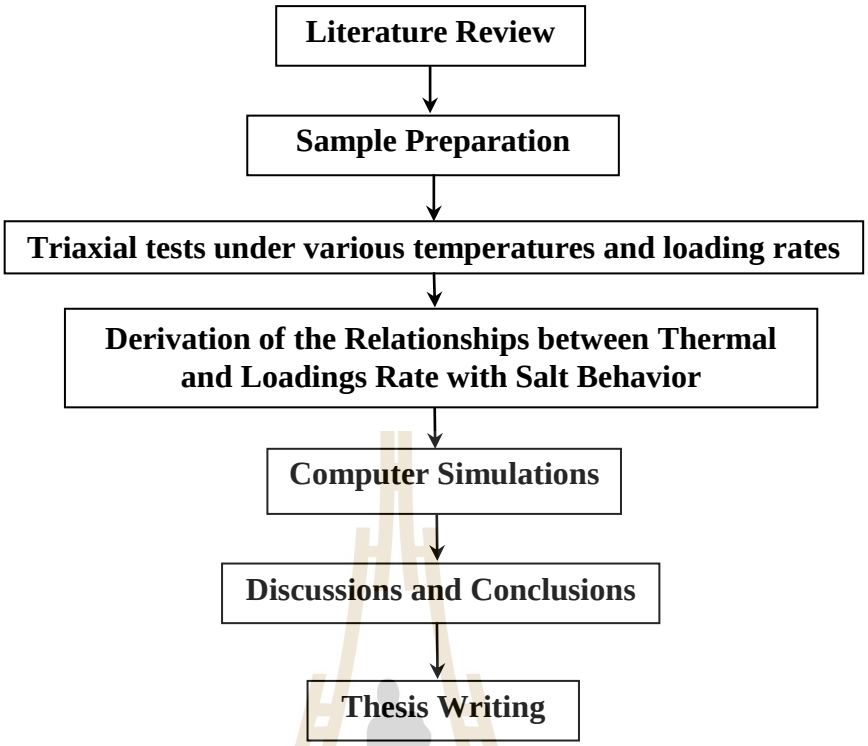

Figure 1.1 Research methodology.

strains induced in the surrounding salt under various air withdrawal rates are calculated and compared against the dilation criteria developed above.

1.3.6 Conclusion and thesis writing

All research activities, methods, and results will be documented and complied in the thesis. The research or findings will be published in the conference proceedings or journals.

1.4 Scope and limitations

The scope and limitations of the research include as follows.

1. Laboratory experiments are conducted on rock salt specimens from the Maha Sarakham formation.

2. Laboratory testing is made under various loading rates ranging from 0.001, 0.01 to 0.1 MPa per second with the confining pressures varying from 0, 3, 7 to 12 MPa.

3. Laboratory testing is performed under various temperatures ranging from 303 to 473 K

4. Up to 60 samples are tested, with the nominal sizes of 5.8×5.8×5.8 cm^3.

5. Testing is made under dry condition.

6. The research findings are published in a journal.

1.5 Thesis contents

This research thesis is divided into seven chapters. The first chapter includes background and rationale, research objectives, research methodology, and scope and limitations. **Chapter II** presents results of the literature review to improve an understanding of rock salt on behavior. **Chapter III** describes the sample preparation. **Chapter IV** describes Triaxial tests under various temperatures and loading rates. **Chapter V** presents derivation of the relationships between thermal and loadings rate with salt behavior. **Chapter VI** presents results computer simulations. **Chapter VII** is the discussions, conclusions and recommendations for future studies.

CHAPTER II

LITERATURE REVIEW

2.1 Introduction

This chapter summarizes the results of literature review carried out to improve an understanding of rock salt behaviour. The topics reviewed here include factors affecting rock salt behavior and thermomechanical effects of salt rocks.

2.2 Factors affecting rock salt behavior

The mechanical behavior of rock salt is complex and is affected by many factors, such as grain size, bonding between grains, time, temperature, humidity, and inclusions, and more. The effects on rock salt characteristics by these factors are normally shown by the differences in deformation and creep properties.

The effects of grain size on the creep behavior and strength of rock salt in laboratory and field conditions are described by Fokker (1998). The average grain size of salt visually observed from the core and post-failure specimens is 5×10×10 millimeters. It is concluded that the large size of the salt crystals increases the effect of the crystallographic features (i.e., cleavage planes) on the mechanics of deformation and failure of the samples. This also agrees with the finding by Aubertin (1996). The dislocations and plastic flows in single crystals of halite are studied by several researchers (Franssen and Spiers, 1990; Raj and Pharr, 1992; Senseny et al., 1992; Wanten et al., 1996). They conclude that the shear strength and deformation of

halite crystals are orientation-dependent. The small size of the sample may not provide good representative test results. This also reflects on the specifications by ASTM (ASTM D2664, D2938, and D3967). The ASTM standard methods specify that to minimize the effect of grain size the sample diameter should be at least ten times the average grain size.

Bonding between grains can affect the creep rate and the strength of salt. Allemandou and Dusseault (1996) observed the post-failure from the Brazilian strength tests and uniaxial compressive strength tests. They report that strength depends on the boundary between grains. This also agrees with the laboratory results obtained by Fuenkajorn and Daemen (1988) who report that weakness or brittleness of the crystal boundary of salt is observed during sample preparation. It is unlikely that a long intact core can drill through the salt formation.

The time-dependent behavior of salt under differential stress raises the question of the significance of time-related test parameters such as loading rate, testing period, and loading sequence. The effects of stress rate and strain rate on the deformation and strength of salt samples have long been recognized (Farmer and Gilbert, 1984; Dusseault and Fordham, 1993). The loading rate must be maintained constant and measured as precisely as possible during the test. The loading sequence and the duration for which each load is sustained by the salt specimens are important since salt tends to behave as a plastic creep material with low yield stress. This situation is found in the triaxial compressive strength test where the confining pressure is applied to the salt cylinder prior to the axial load. Due to the nonlinear behavior of salt, the analysis of stress induced in a salt specimen is complex and the Boltzmann law of superposition cannot be used.

Samsri et al. (2010) determined the effect of the intermediate principal stress on the time-dependent behavior of rock salt obtained from the Maha Sarakham formation. A polyaxial creep frame applies constant principal stresses to cubical shaped specimens with a nominal dimension of 5.4×5.4×5.4 cm^3. The applied octahedral shear stresses (τ_{oct}) vary from 5, 8, 11 to 14 MPa while the mean stress (σ_m) is maintained constant at 15 MPa for all specimens. The loading conditions range from the triaxial ($\sigma_1 \neq \sigma_2 = \sigma_3$) to the polyaxial ($\sigma_1 \neq \sigma_2 \neq \sigma_3$ and $\sigma_1 = \sigma_2 \neq \sigma_3$) stress states. The Burgers model is used to describe the elastic, visco-elastic (transient) and visco-plastic (steady-state) behavior of the salt. The specimen deformations are monitored along the three principal axes for up to 21 days. Regression analyses on the octahedral shear strain - time curves suggest that the salt elastic modulus tends to be independent of the intermediate principal stress (σ_2). It however tends to increase as the applied τ_{oct} increases. Under the same magnitude of τ_{oct} the visco-elastic and visco-plastic parameters increases when σ_2 increases from the triaxial condition, $\sigma_2 = \sigma_3$, to the condition where $\sigma_2 = \sigma_1$.

Fuenkajorn and Phueakphum (2010) performed cyclic loading tests on the Maha Sarakham salt. Their results indicated that the salt compressive strength decreases with increasing number of loading cycles, which can be best represented by a power equation. The salt elastic modulus decreases slightly during the first few cycles, and tends to remain constant until failure. It seems to be independent of the maximum loads. Axial strain–time curves compiled from loci of the maximum load of each cycle apparently show a time-dependent behavior similar to that of creep tests under static loading. In the steady-state creep phase, the visco-plastic coefficients calculated from the cyclic loading test are about an order of magnitude lower than

those under static loading. The salt visco-plasticity also decreases with increasing loading frequency. Surface subsidence and cavern closure simulated using parameters calibrated from cyclic loading test results are about 40% greater than those from the static loading results. This suggests that application of the property parameters obtained from the conventional static loading creep test to assess the long-term stability of storage caverns in salt with internal pressure fluctuation may not be conservative.

Sriapai et al. (2011) studied the uniaxial and triaxial compression tests have been performed on Maha Sarakham salt to assess the influence of loading rate on the compressive strength of the rock. The salt specimens with a nominal dimension of 5.4×5.4×5.4 cm^3 are compressed to failure using a polyaxial load frame. The lateral confining pressures are maintained constant at 0, 3, 7, 12, 20 and 28 MPa while the axial stresses are applied at constant rates of 0.001, 0.01, 0.1, 1.0 and 10 MPa/s. The salt strengths exponentially increase with the loading rates. The effect is more pronounced under high confining pressures.

Temperature or heating affects the creep deformation, because they increase the plastic property of salt and long-term deformation (Pudewills et al., 1995). Jeremic (1994) postulates that rock salts lose their brittleness after extension tempering at approximately 600 °C and exhibit a critical shear stress up to 1 MPa. Hamami et al. (1996) study the effect of temperature and conclude that the temperature increase, as for the deviatoric stress, results in an increase of the material deformation. Cristescu and Hunsche (1996) study the temperature effect on the strain rate suitable for laboratory testing. They suggest that the appropriate strain rate for

testing at 100 °C and 200 °C is 10^{-8} s^{-1} and 10^{-7} s^{-1} because the temperature can affect the creep deformation and strength of salt under high temperatures.

Yavuz et al. (2010) study the thermal effect on the physical properties of carbonate rocks. The effect of thermal damage on the physical properties of five carbonate rocks has been investigated. The tests were con ducted on two marbles and three limes tones, mainly composed of calcite but with different grain sizes, porosities, structural and textural characteristics. Cubic samples prepared from these rocks were gradually heated to a specific temperature level of 100, 200, 300, 400 and 500 °C, and gradually cooled down to room temperature without causing thermals hock in order to investigate the effect of heating temperature on physical properties such as microstructure, bulk density, effective porosity and P-wave velocity. Microscopic investigations from thin sect ions showed that damage in rock s at elevated temperatures was induced in different severity depending on grain size, porosity, structural and textural characteristics. Color changes were also ob served in porous limes tones (Lymra and Travertine) due to organic material. In accordance with the degree of calcite dilation depending on heating temperature and in turn new microcrack occurrence, separation along intragrain and/or intergrain boundaries and widening of existing cracks, P-wave velocity decreased to various levels of the initial value, whereas porosity increased. Microscopic analyses and P-wave velocity measurements indicate that compaction of rock structure up to 150 °C occurred and induced calcite dilation had no significant damage effect on the rock material. Compact ion of rock structure led to an increase in P-wave velocity and slight decrease in porosity. Most of the damage occurred within 24 h of heating time and further heating treatments brought relatively minor changes in physical properties.

Damage intensity was well explained with P-wave velocity and effective porosity values depending on temperature increase.

Humidity affects salt properties by reducing the strength of rock salt (Hunsche and Schulze, 1996; Cleach et al., 1996). Hydrated reaction between water and salt occurs when salt contacts with air humidity. The temperature effects can catalyze the hydration. They find that when subjecting to air humidity, the strength of salt can be decreased by up to 1 MPa (normally, strength of 30 MPa).

Inclusions and impurities in salt have an effect on to the creep deformation and strength of salt. The degree of impurity is varying for different scales of the rock salt. On a small scale, such as for laboratory specimens, the impurities of salt involve ferruginous inclusions and thin clay seams along grain boundaries or bedding planes. The impurities distribute uniformly in the salt may affect the strength of rock salt. This can decrease the creep deformation and strength of rock salt. These phenomena have been reported by Franssen and Spiers (1990), Raj and Pharr (1992) and Senseny et al. (1992).

Kensakoo (2006) study the relationship between the uniaxial compressive and Brazilian tensile strengths, elastic modulus and visco-plasticity coefficient of rock salt specimens and their mineralogical compositions and petrographic features. The main inclusions for the salt specimens tested here are anhydrite and clay minerals. The anhydrite inclusions appear as thin seams or beds perpendicular to the core axis with thickness varying from few millimeters to several centimeters. The clay minerals (about 1-5% by weight) scatter between the salt crystals of some specimens. The compressive strength of the salt specimens linearly increases from 27 MPa to about 40 MPa as the anhydrite inclusion increases in the range from 0% to nearly 100%.

This is primarily because the anhydrite inclusion makes the salt portion shorter, creates the end effect, and hence increasing the specimen strength. The combined effect between the salt and anhydrite properties also causes the increase of the specimen elasticity from 22 GPa to as high as 36 GPa. Tensile strengths of the salt specimens will also increase with the anhydrite inclusion if the inclusion is beyond 50% by weight. The clay content of less than 4% has no significant impact on the salt tensile strength. The effect of clay content beyond 5% in the salt specimens remains unclear because the range of the clay contents among different specimens are relatively low and narrow (0- 5%).

Fuenkajorn et al. (2011) study the intrinsic variability of rock salt specimens obtained from the Middle and Lower members of the Maha Sarakham formation in the Khorat basin. Prior to the mechanical tests, the types and amount of inclusions were identified by visual examination and after testing by X-ray diffraction and dissolution methods. The uniaxial compressive strength of the specimens linearly increases from 27 MPa to about 40 MPa as the anhydrite content (by weight) increases from 0% (pure halite) to 100% (pure anhydrite). The combined stiffness of the salt and the anhydrite causes an increase of specimen elasticity from 22 GPa (pure salt) to as high as 36 GPa (pure anhydrite). Tensile strengths increase with increasing anhydrite content, particularly when the content is above 60% by weight. Below this limit the anhydrite has an insignificant impact on the specimen tensile strength. The tensile strength of salt crystals can be as high as 2 MPa, whereas that of the inter-crystalline boundaries is 1 MPa. The visco-plasticity increases exponentially with crystal size, as dislocation glide mechanisms become predominant for the specimens

comprising large crystals. Salt specimens with fine crystals deform by dislocation climb mechanisms, and hence reduce the specimen's visco-plasticity.

2.3 Thermomechanical effects

Pudewills and Droste (2003) study the numerical simulation of the thermal and thermomechanical response of the large-scale in situ experiment ''thermal simulation of drift emplacement'', which was carried out in the Asse salt mine in Germany, is presented. The analyses concern the modeling of the temperature fields, thermally induced drift closure followed by the consolidation of backfill material and the distribution of the stresses. Finite element codes (ADINA and MAUS) specially developed for the repository structures as well as a general-purpose code have been used. The primary objective of the investigations is to evaluate the capability of these codes to simulate the thermomechanical behavior of rock salt and backfill material under representative conditions of a waste repository by comparing of calculated results with in situ measurements. An overall good agreement between modeling and in situ measured results indicates that most thermomechanical effects are fairy well represented by the numerical models.

The thermomechanical behavior of rock salt was described in the finite element analyses by a thermoelastic material model with a temperature-dependent steady- state creep and based on the experimental results. According to this model, the total strain rate is given as the sum of elastic, thermal, and steady-state creep rates. This constitutive relation governing the creep strain rate of rock salt is described as follows:

$$\varepsilon_{ef} = A\sigma^{5}_{ef} \exp(-Q/(RT)) \quad (2.1)$$

Dwivedi et al. (2008) study the thermo-mechanical and transport properties of granites which is required to understand and model a number of processes in the earth crust such as folding, geothermal activity, magmatic intrusions, plate tectonics and nuclear waste disposal. Thermo-mechanical properties of Indian granite (IG) is studied various at high temperatures in the range of 30–160 °C, keeping in view the highest temperatures expected in underground nuclear waste repositories. These properties are Young's modulus, uniaxial compressive strength, tensile strength, Poisson's ratio, coefficient of linear thermal expansion, creep behaviour and the development of micro-crack on heating using scanning electron microscope (SEM). The results is indicate that the temperature effect on creep under atmospheric pressure condition (0.1 MPa) was not observed up to 160 °C in the duration of 4 months for Indian pink granite. Permeability decreases with increase in temperature. Thermal conductivity and thermal diffusivity both decrease with increase in temperature. The de crease in thermal conductivity with temperature is high on increase of the confining pressure. On the other hand, specific heat increases with increase in temperature and pressure up to 600 °C and the coefficient of linear thermal expansion increases with temperature up to 470 °C. Viscosity of molten granite decreases with increase in temperature. Ultimate compressive strength increases with increase in confining pressure. On the other hand, tensile strength of all granites decreases with increase in temperature for the reported temperature range 30–1050 °C. Normalized cohesion (c/c_0) and normalized angle of internal friction (ϕ/ϕ_0) both decrease with increase in temperature for all granites.

CHAPTER III

SAMPLE PREPARATION

This chapter describes sample preparation and specifications of the tested rock salt specimens. The method follows as much as practical the standard practices. The salt specimens tested here are obtained from a borehole. They are from the lower members of the Maha Sarakham formation in Khammouan, Laos. This salt member has long been considered as a host rock for compressed-air energy storage by the Thai Department of Energy. The core specimens are dry cut and ground, as shown in Figure 3.1. The core specimens with a nominal diameter of 100 mm were drilled from depths ranging between 170 and 270 m. The salt specimens have nominal dimensions of 5.8×5.8×5.8 cm^3, as shown in Figure 3.2. The rock salt is relatively pure halite with slight amount (less than 1-2%) of anhydrite, clay minerals and ferrous oxide. The average crystal (grain) size is about 5×5×10 mm^3. Warren (1999) gives detailed descriptions of the salt and geology of the basin. Sample preparation is conducted in the laboratory facility at the Suranaree University of Technology. A total of 80 specimens were prepared for testing.

Figure 3.1 A salt specimen is dry cut by a cutting machine.

Figure 3.2 Some salt specimens prepared for true triaxial cyclic loading test.

The nominal dimensions are 5.4×5.4×5.4 cm^3.

Table 3.1 Specimen dimensions prepared for triaxial test.

Specimen	Width (mm)	Length (mm)	Height (mm)	Weight (g)	Density (g/cc)
LS-TRILT-01	58.92	58.40	59.28	432.41	2.12
LS-TRILT-02	59.64	60.56	60.32	479.31	2.20
LS-TRILT-03	56.24	56.44	58.03	407.11	2.21
LS-TRILT-04	58.30	56.65	57.72	438.44	2.30
LS-TRILT-05	56.65	56.24	58.03	399.35	2.16
LS-TRILT-06	57.37	57.99	60.32	437.48	2.18
LS-TRILT-07	58.61	56.86	59.70	423.69	2.13
LS-TRILT-08	56.96	56.65	57.72	400.43	2.15
LS-TRILT-09	58.50	59.53	59.28	452.17	2.19
LS-TRILT-10	58.71	58.61	59.80	454.73	2.21
LS-TRILT-11	56.65	58.50	59.07	415.05	2.12
LS-TRILT-12	57.06	55.93	57.20	396.13	2.17
LS-TRILT-13	56.96	58.30	57.72	408.25	2.13
LS-TRILT-14	57.99	59.53	57.20	440.36	2.23
LS-TRILT-15	57.47	56.65	57.41	409.34	2.19
LS-TRILT-16	55.93	56.75	57.51	396.14	2.17
LS-TRILT-17	57.58	58.40	60.22	443.43	2.19
LS-TRILT-18	58.92	58.92	59.80	437.98	2.11
LS-TRILT-19	57.99	55.62	57.41	390.69	2.11
LS-TRILT-20	57.89	58.50	57.10	411.86	2.13
LS-TRILT-21	56.75	57.68	57.72	404.35	2.14
LS-TRILT-22	57.47	58.92	60.22	444.50	2.18
LS-TRILT-23	58.61	59.02	58.97	434.45	2.13
LS-TRILT-24	56.96	57.68	57.41	405.51	2.15
LS-TRILT-25	57.37	58.61	60.32	444.17	2.19
LS-TRILT-26	58.61	59.74	59.49	460.30	2.21
LS-TRILT-27	57.47	58.09	56.37	398.98	2.12
LS-TRILT-28	56.96	59.64	59.59	439.26	2.17
LS-TRILT-29	57.78	56.96	57.20	400.99	2.13
LS-TRILT-30	58.92	57.58	57.62	435.84	2.23
LS-TRILT-31	59.10	58.52	59.81	453.04	2.19
LS-TRILT-32	61.29	60.69	60.86	491.24	2.17

Table 3.1 Specimen dimensions prepared for triaxial test (cont.).

Specimen	Width (mm)	Length (mm)	Height (mm)	Weight (g)	Density (g/cc)
LS-TRILT-33	57.12	56.56	58.55	414.27	2.19
LS-TRILT-34	57.33	56.76	58.24	399.90	2.11
LS-TRILT-35	56.91	56.35	58.55	396.23	2.11
LS-TRILT-36	58.68	58.10	60.86	437.90	2.11
LS-TRILT-37	57.54	56.97	60.23	420.55	2.13
LS-TRILT-38	57.33	56.76	58.24	405.58	2.14
LS-TRILT-39	60.25	59.65	59.81	468.63	2.18
LS-TRILT-40	59.31	58.72	60.34	447.63	2.13
LS-TRILT-41	59.21	58.62	59.60	444.77	2.15
LS-TRILT-42	56.60	56.04	57.71	400.92	2.19
LS-TRILT-43	59.00	58.41	58.24	443.57	2.21
LS-TRILT-44	60.25	59.65	57.71	477.08	2.30
LS-TRILT-45	57.33	56.76	57.92	407.16	2.16
LS-TRILT-46	57.43	56.87	58.03	413.17	2.18
LS-TRILT-47	59.10	58.52	60.76	447.58	2.13
LS-TRILT-48	59.62	59.03	60.34	456.61	2.15
LS-TRILT-49	56.29	55.73	57.92	397.94	2.19
LS-TRILT-50	59.21	58.62	57.61	441.88	2.21
LS-TRILT-51	58.37	57.80	58.24	416.54	2.12
LS-TRILT-52	59.62	59.03	60.76	464.06	2.17
LS-TRILT-53	59.73	59.14	59.50	447.63	2.13
LS-TRILT-54	58.37	57.80	57.92	433.83	2.22
LS-TRILT-55	59.31	58.72	60.86	481.20	2.27
LS-TRILT-56	60.46	59.86	60.02	475.71	2.19
LS-TRILT-57	58.79	58.21	56.88	434.02	2.23
LS-TRILT-58	60.35	59.76	60.13	487.91	2.25
LS-TRILT-59	57.64	57.07	57.71	413.92	2.18
LS-TRILT-60	58.27	57.69	58.13	416.26	2.13
LS-TRILT-61	60.32	56.91	59.65	440.29	2.15
LS-TRILT-62	59.49	58.68	56.76	433.98	2.19
LS-TRILT-63	56.37	57.54	56.87	407.60	2.21
LS-TRILT-64	59.59	57.33	58.52	423.83	2.12

Table 3.1 Specimen dimensions prepared for triaxial test (cont.).

Specimen	Width (mm)	Length (mm)	Height (mm)	Weight (g)	Density (g/cc)
LS-TRILT-65	57.20	60.25	59.03	441.47	2.17
LS-TRILT-66	57.62	59.31	55.73	405.65	2.13
LS-TRILT-67	59.81	59.21	58.62	460.86	2.22
LS-TRILT-68	60.86	56.60	57.80	451.95	2.27
LS-TRILT-69	58.55	59.00	59.03	430.30	2.11
LS-TRILT-70	58.24	60.25	59.14	441.98	2.13

CHAPTER IV

TRIAXIAL TESTS UNDER VARIOUS TEMPERATURES AND LOADING RATES

4.1 Introduction

The objective of the laboratory testing is to determine the effect of temperatures on strengths and loading rates of rock salt. This chapter describes the method.

4.2 Test equipment

Steel platens with heater coil are the key component for this experiment. Its are shown in Figure 4.1. The heater coil is wrapped around the steel platen Electric heating is through a resistor converts electrical energy into heat energy. Electric heating devices use Nichrome (Nickel-Chromium Alloy) wire supported by heat resistant. A thermostat (Figure 4.2) is a component of a control system which senses the temperature of a system so that the system's temperature is maintained near a desired setpoint. A heating element converts electricity into heat through the process of resistive. Electric current passing through the element encounters resistance, resulting in heating of the element. The thermostat is SHIMAX MAC5D-MCF-EN Series DIGITAL CONTROLLER. The digital controller is 48×48 mm with panel depth of 62-65 mm. Power supply is a 100-240V ± 10%AC on security surveillance

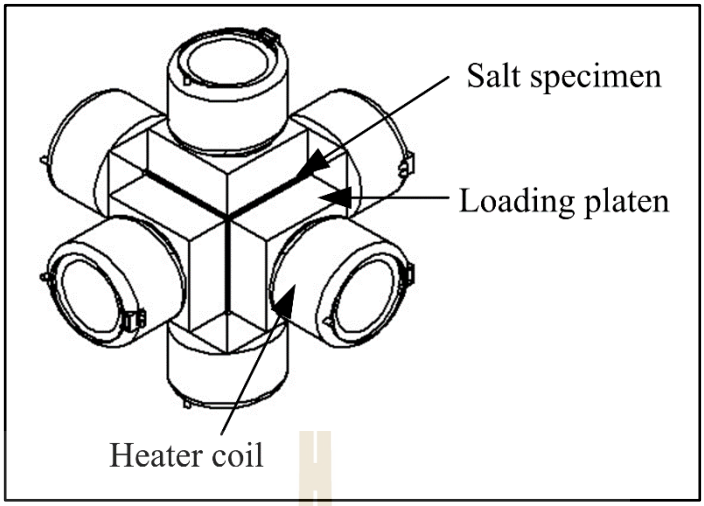

Figure 4.1 Steel platen.

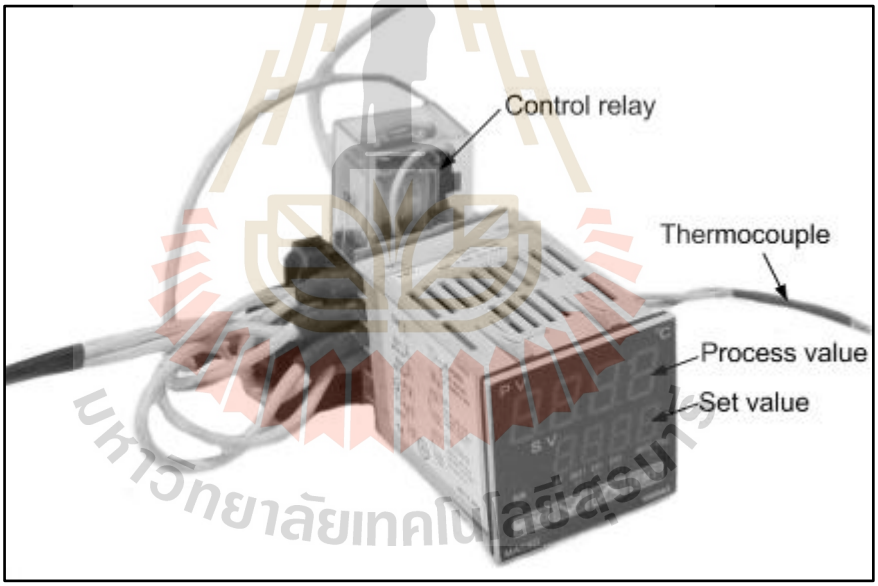

Figure 4.2 Thermostat with digital controller.

system. The accuracy is ± 0.3%FS + 1digit. The thermocouple is type E1 that can measure the temperatures ranging of 0-700°C.

4.3 Test method

4.3.1 Heating method

To test the salt specimens under elevated temperatures, the prepared specimens and loading platens are heated by heater coil, thermocouple and thermostat for 24 hours before testing at 303, 323, 373, 423 and 473 Kelvin (Figure 4.3). The temperature is measured and regulated by using thermocouple and thermostat. A digital temperature regulator is used to maintain constant temperature to the specimen. The changes of specimen temperatures between before and after testing are less than 5 kelvin. As a result the specimen temperatures are assumed to be uniform and constant with time during the mechanical testing (i.e., isothermal condition).

4.3.2 Uniaxial and triaxial compression tests

The uniaxial and triaxial compression tests are performed to determine the compressive strength and deformation of salt specimen under various confining pressure and temperature. A polyaxial load frame (Figure 4.4) (Fuenkajorn and Kenkhunthod, 2010) has been used to apply axial stress and lateral stresses to the granite specimens. The test frame utilizes two pairs of cantilever beams to apply lateral stresses to the specimen while the axial stress is applied by a hydraulic cylinder connected to an electric pump. The uniform lateral stresses on the specimens range from 0, 3, 7 to 12 MPa, and the constant axial stress rate of 0.1, 0.01 and 0.001 MPa/s until failure occurs. The specimen deformation monitored in the three principal

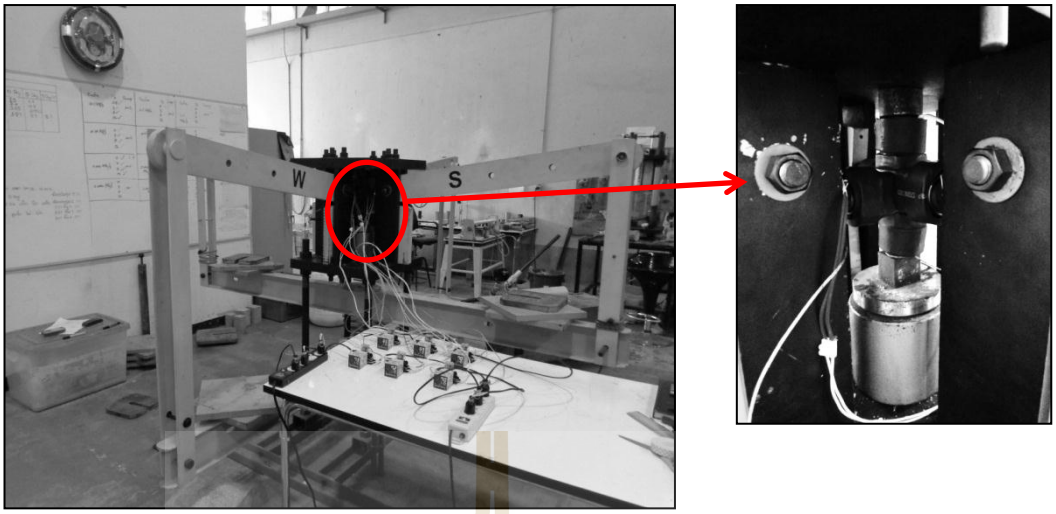

Figure 4.3 Temperatures measured and regulated by thermocouples and thermostats while the specimen installed in polyaxial load frame.

directions is used to calculate the principal strains during loading. The failure stresses are recorded and mode of failure examined. The frame has an advantage over the conventional triaxial (Hoek) cell because it allows a relatively quick installation of the test specimen under triaxial condition, and hence the change of the specimen temperature during testing is minimal.

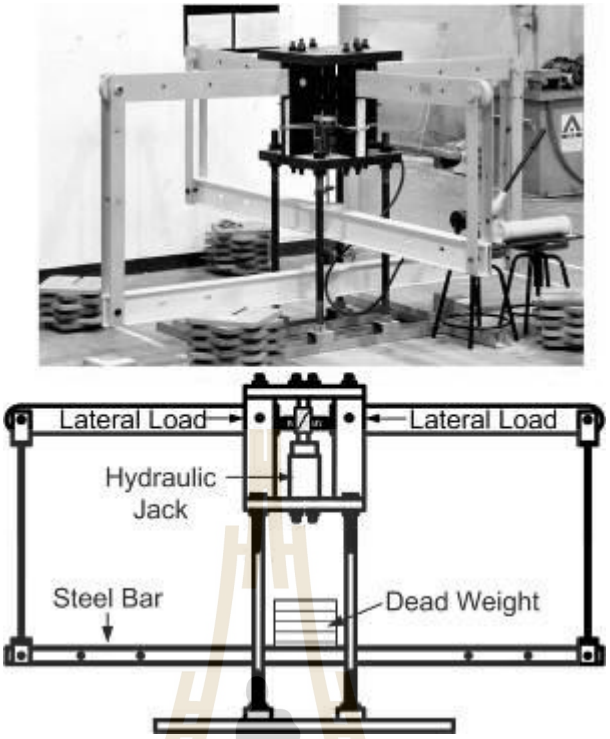

Figure 4.4 Polyaxial load frame **(**Fuenkajorn and Kenkhunthod, 2010).

CHAPTER V

TESTS RESULTS

5.1 Introduction

This chapter describes test results in terms of strength and elasticity of salt specimen. The measured deformations are used to determine the strains along the principal axes during loading. The failure stresses are recorded and mode of failure examined. The salt strength are also presented in the multi axial form for multi-axial strength analysis.

5.2 Stress-strain curves

Appendix A shows the stress-strain curves from the start of loading to failure for the salt specimens in triaxial stress states. Figure 5.1 shows example the stress–strain curves of some salt specimens. Each salt specimen shows virtually identical lateral strains measured from the two mutually perpendicular directions ($\varepsilon_2=\varepsilon_3$). The specimens tend to show nonlinear behavior, particularly under high temperatures and low loading rates. The results indicate that the strengths of salt decrease with increasing temperature and decreasing loading rate. Under the same confining pressure (σ_3), the maximum principal strains at failure (σ_1) increase with increasing specimen temperature and decreasing loading rate.

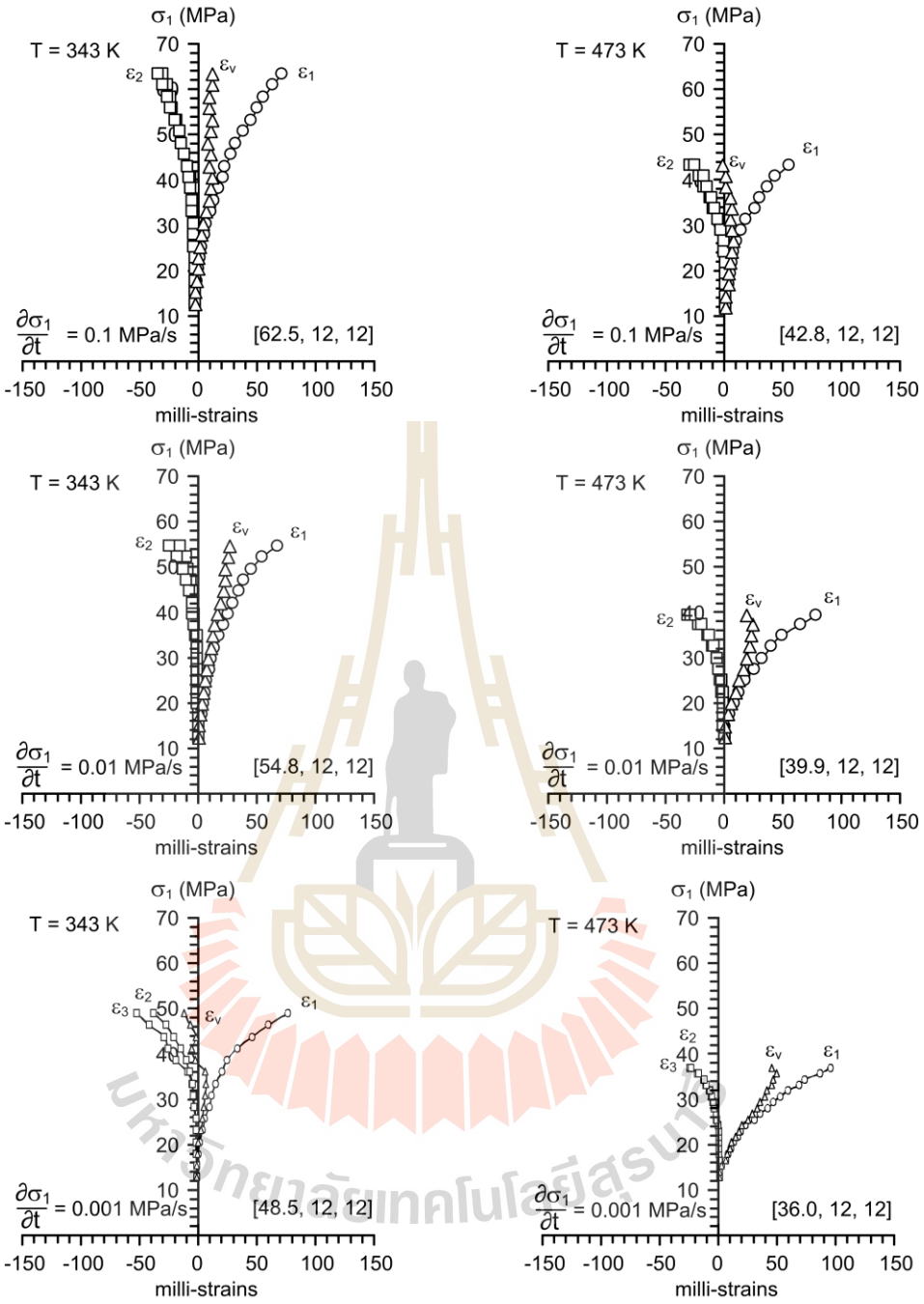

Figure 5.1 Axial, lateral and volumetric strains measured from various temperatures with confining pressures. Numbers in brackets indicate [σ_1, σ_2, σ_3] at failure.

5.3 Mode of failure

Post-failure observations suggest that (Figure 5.2) mode of failure are longitudinal spitting, densified compressive shear planes and no shear damage plane.

Under σ_3= 0 MPa, all loading rate and low temperature specimens show mode of failure of longitudinal spitting. The salt samples have brittle behavior and show clear mode of failure. Under σ_3 = 3-12 MPa, salt specimens under all loading rate and low temperatures show compressive shear plane. Under high temperatures (σ_3 = 3-7 MPa) no shear damage plane is observed.

5.4 Octahedral shear stress-strain relations

An attempt is made here to compare the stress-strain relations obtained from different rates and temperatures. To combine the principal stresses and strains, a muti-axial form of stress-strain relation is needed. Here the octahedral shear stress (τ_{oct}) are calculated as a function of octahedral shear strain (γ_{oct}) (Jaeger et al., 2007) as follows.

$$\tau_{oct} = (1/3)[(\sigma_1 - \sigma_2)^2 + (\sigma_1 - \sigma_3)^2 + (\sigma_2 - \sigma_3)^2]^{1/2} \quad (5.1)$$

$$\gamma_{oct} = (1/3)[(\varepsilon_1 - \varepsilon_2)^2 + (\varepsilon_1 - \varepsilon_3)^2 + (\varepsilon_2 - \varepsilon_3)^2]^{1/2} \quad (5.2)$$

Figure 5.3 plots octahedral shear stresses (τ_{oct}) as a function of octahedral shear strains (γ_{oct}). The specimens tend to show nonlinear behavior, particularly under high confining pressures and temperatures. Higher strengths are obtained under lower temperatures and higher loading rate. Increasing the temperatures from 303 K to 473 K can reduce the salt strengths by as much as 50%.

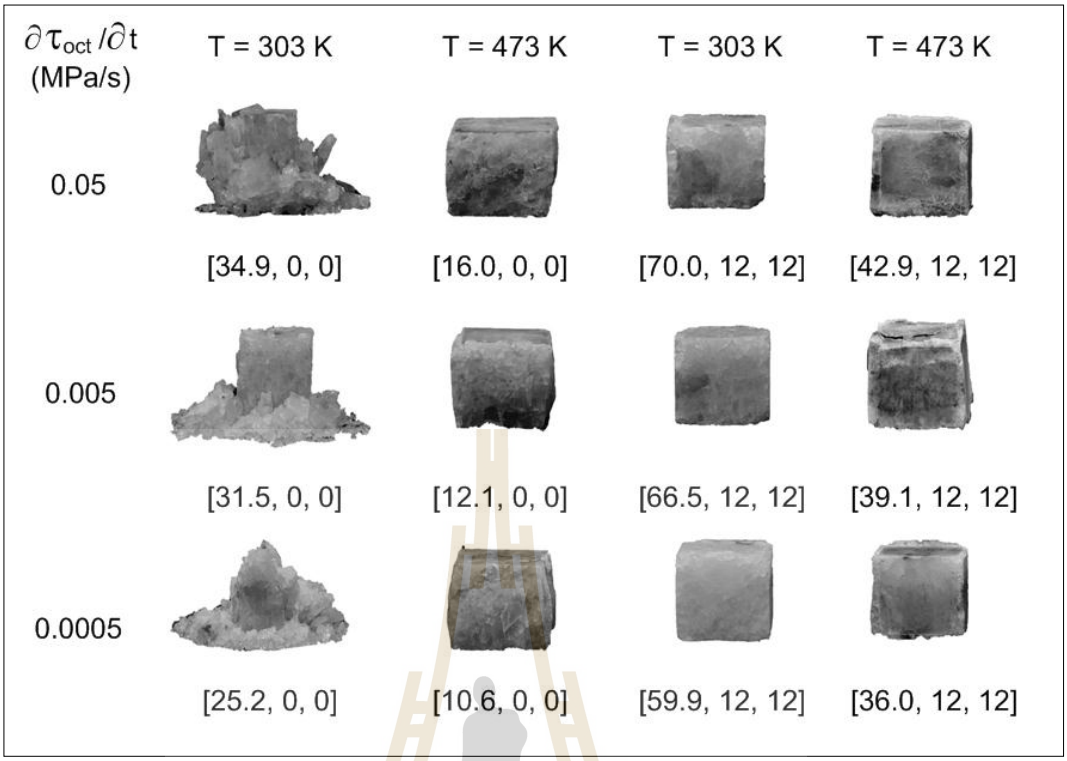

Figure 5.2 Some post-test specimens of Maha Sarakham salt. Number in brackets indicate $[\sigma_1, \sigma_2, \sigma_3]$ at failure.

The strains at failure clearly. The effects of loading rates within the rage of testing do not have significant impact on the salt strengths.

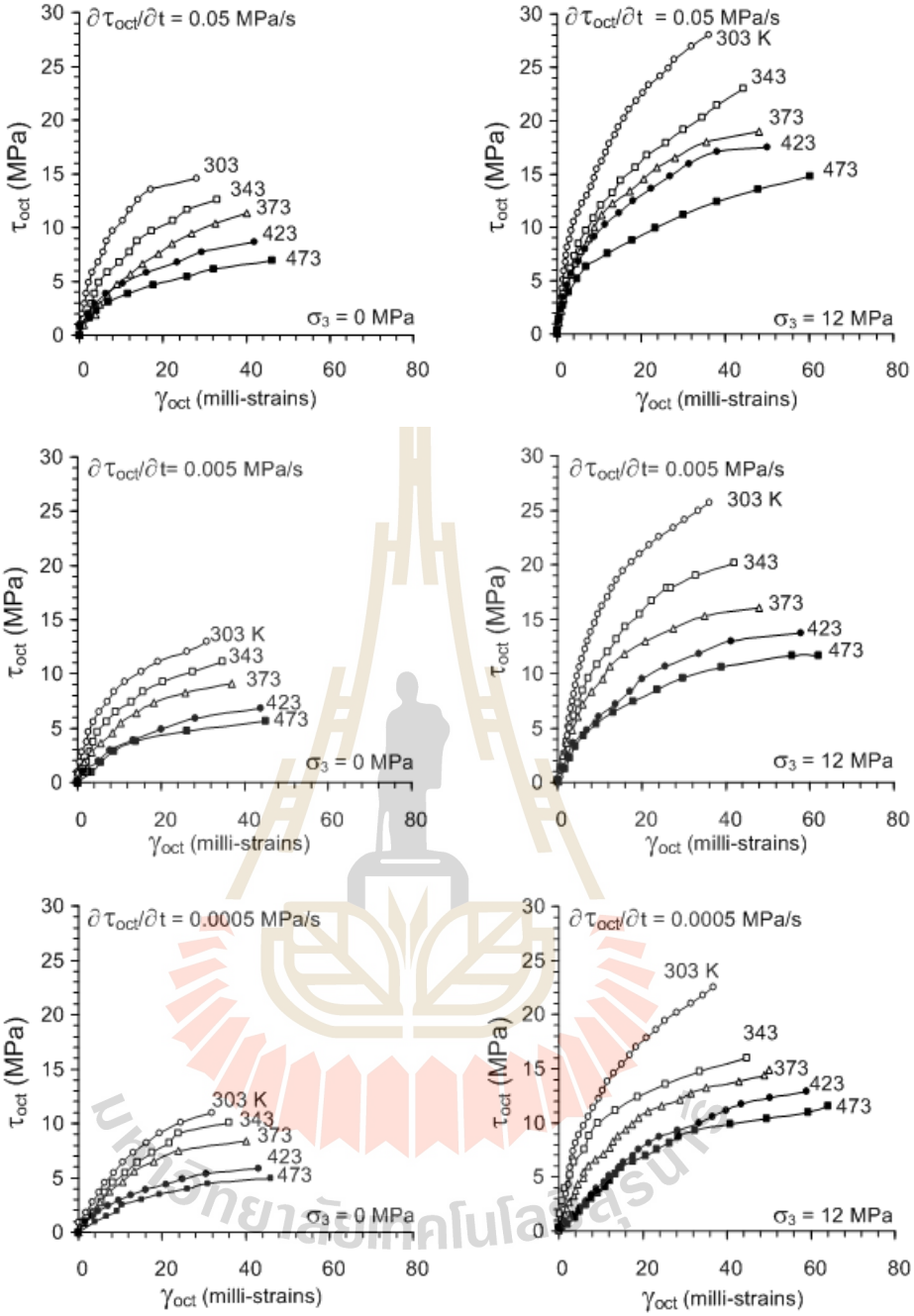

Figure 5.3 Octahedral shear stress (τ_{oct}) as a function of octahedral shear strain (γ_{oct}) until failure.

5.5 Octahedral shear strengths

For each specimen the octahedral shear stress at failure ($\tau_{oct,f}$) and at dilation ($\tau_{oct,d}$) can be calculated from the principal stresses as follows:

$$\tau_{oct,f} = (1/3)[(\sigma_{1,f} - \sigma_{2,f})^2 + (\sigma_{1,f} - \sigma_{3,f})^2 + (\sigma_{2,f} - \sigma_{3,f})^2]^{1/2} \quad (5.3)$$

$$\tau_{oct,d} = (1/3)[(\sigma_{1,d} - \sigma_{2,d})^2 + (\sigma_{1,d} - \sigma_{3,d})^2 + (\sigma_{2,d} - \sigma_{3,d})^2]^{1/2} \quad (5.4)$$

$$\sigma_m = (\sigma_1 + \sigma_2 + \sigma_3) / 3 \quad (5.5)$$

where $\sigma_{1,f}$, $\sigma_{2,f}$ and $\sigma_{3,f}$ are the major, intermediate and minor principal stresses at the point where the failure occurs, and $\sigma_{1,d}$, $\sigma_{2,d}$ and $\sigma_{3,d}$ are the major, intermediate and minor principal stresses at the point where the dilation occurs.

Table 5.1 summarizes the results from all specimens, listing the major principal (vertical) stresses (σ_1) at failure for each lateral confining pressure (σ_3), temperatures and loading rate. Three principal stresses equivalent to the dilation point are represented by $\sigma_{1,d}$, $\sigma_{2,d}$ and $\sigma_{3,d}$. Figure 5.4 shows how to determine the $\sigma_{1,d}$, $\sigma_{2,d}$ and $\sigma_{3,d}$ from the test results.

The shear rate is determined by taking a derivative of Eq. (6.1) with respect to time (t). Since σ_3 is constant with time here, the following relation is obtained:

$$\tau_{oct} = \left(\sqrt{2}/3\right)\partial\sigma_1/\partial t \quad (5.6)$$

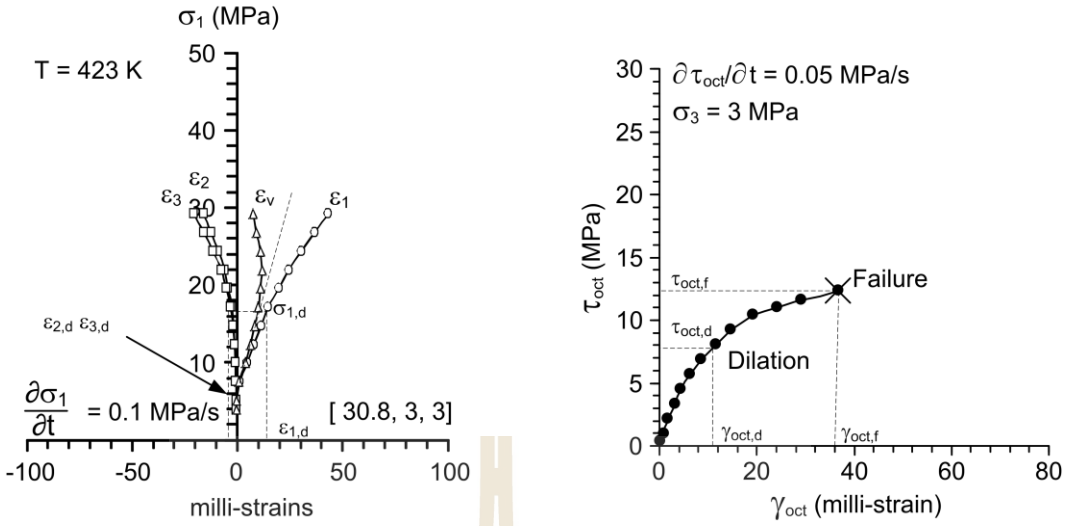

Figure 5.4 An example showing how principal stresses and strains at dilation are determined from the test results (left), and their corresponding octahedral shear stress and shear strain at dilation (right).

For each specimen, the octahedral shear stresses at failure and at dilation are plotted as a function of mean stress in Figure 5.5. The octahedral shear strength linearly increases with the mean stress for both failure and dilation.

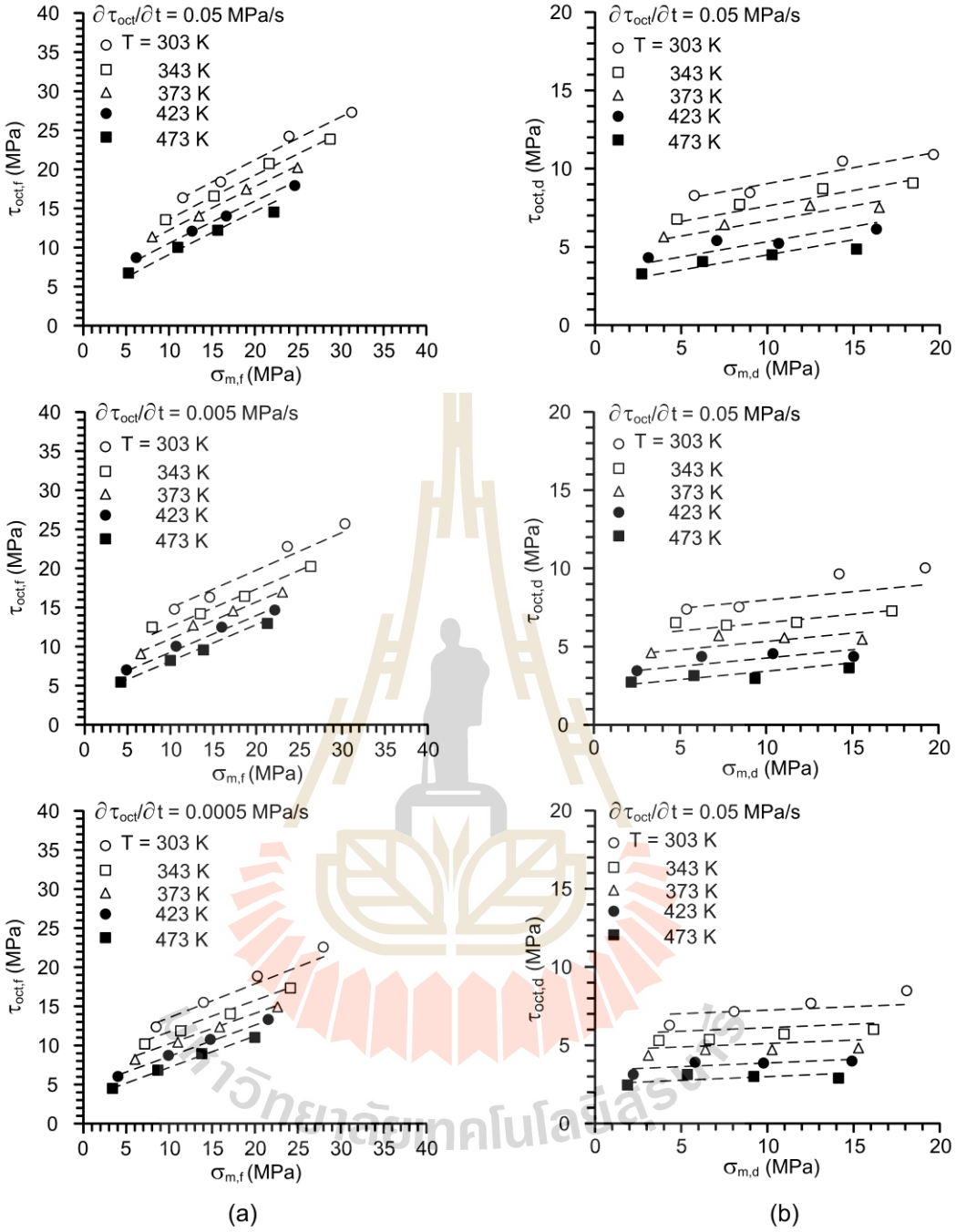

Figure 5.5 Octahedral shear stress (τ_{oct}) at failure (a) and at dilation (b) as a function of mean stress (σ_m) for various temperatures (T) and shear rate ($\partial\tau_{oct}/\partial t$).

Table 5.1 Salt strengths under various loading rates, confining pressures and temperatures.

T (K)	$\partial\sigma_1/\partial t$ (MPa/s)	$\partial\tau_{oct}/\partial t$ (MPa/s)	σ_3 (MPa)	σ_1 (MPa)	σ_m (MPa)	ε_{m_3} (10^{-3})	$\tau_{oct,f}$ (MPa)	$\gamma_{oct,f}$ (10^{-3})
303	0.1	0.05	0	34.96	11.65	2.01	16.48	38.85
			3	42.00	16.00	1.96	18.38	24.30
			7	58.30	24.10	2.35	24.18	29.09
			12	70.00	31.33	3.05	27.34	31.73
	0.01	0.005	0	31.50	10.50	0.19	14.85	49.76
			3	37.90	14.63	3.96	16.45	24.31
			7	56.60	23.53	2.50	23.38	35.62
			12	66.50	30.17	2.50	25.69	36.09
	0.001	0.0005	0	25.22	8.41	4.29	11.89	51.44
			3	36.05	14.02	2.54	15.58	32.10
			7	46.55	20.18	1.77	18.65	33.14
			12	59.90	27.97	1.38	22.58	36.82
343	0.1	0.05	0	28.79	9.60	4.35	13.57	37.08
			3	38.61	15.24	3.99	16.53	31.03
			7	50.99	21.66	2.06	20.74	43.42
			12	62.59	28.86	4.97	23.85	49.25
	0.01	0.005	0	27.56	7.88	0.43	12.99	34.72
			3	33.06	13.39	6.52	13.91	30.56
			7	41.68	18.56	12.24	16.35	45.53
			12	54.84	26.28	8.83	20.19	42.07
	0.001	0.0005	0	21.34	7.11	4.17	10.06	32.87
			3	26.97	11.36	5.86	11.04	36.59
			7	37.14	17.05	8.20	14.21	41.47
			12	48.48	24.16	2.67	17.19	57.24
373	0.1	0.05	0	24.05	8.02	2.30	11.34	39.77
			3	33.27	13.49	3.40	13.99	33.42
			7	46.86	19.02	6.36	18.79	51.09
			12	51.14	25.05	3.16	18.45	35.49
	0.01	0.005	0	19.37	6.46	0.58	9.13	34.51
			3	30.74	12.65	3.73	12.80	38.73
			7	37.66	17.22	11.76	14.45	50.76
			12	44.50	22.83	2.40	15.32	40.91
	0.001	0.0005	0	17.78	5.93	1.12	8.38	30.47
			3	25.86	10.99	2.96	10.52	39.35
			7	33.06	15.69	2.00	12.28	62.06
			12	43.68	22.56	0.11	14.94	52.56

Table 5.1 Salt strengths under various loading rates, confining pressures and temperatures (cont.).

T (K)	$\partial\sigma_1/\partial t$ (MPa/s)	$\partial\tau_{oct}/\partial t$ (MPa/s)	σ_3 (MPa)	σ_1 (MPa)	σ_m (MPa)	ε_{m_3} (10^{-3})	$\tau_{oct,f}$ (MPa)	$\gamma_{oct,f}$ (10^{-3})
423	0.1	0.05	0	18.43	6.14	5.34	8.69	39.64
			3	30.76	12.65	4.04	12.81	29.04
			7	36.16	16.72	13.92	13.75	36.42
			12	50.12	24.71	3.76	17.97	43.28
	0.01	0.005	0	14.51	4.84	1.33	6.84	43.87
			3	24.67	10.62	4.38	9.93	30.89
			7	33.50	15.83	6.08	12.49	61.80
			12	42.02	22.01	2.62	14.15	57.78
	0.001	0.0005	0	12.44	4.15	3.78	5.86	38.59
			3	22.44	9.85	3.35	8.90	23.50
			7	30.15	14.72	20.80	10.92	52.03
			12	40.72	21.57	8.02	13.54	67.55
473	0.1	0.05	0	16.04	5.35	2.08	7.56	36.33
			3	25.60	10.93	8.66	10.37	27.00
			7	33.26	15.75	4.72	12.38	37.96
			12	42.87	22.29	2.03	14.55	38.82
	0.01	0.005	0	12.06	4.02	2.01	5.68	43.76
			3	22.17	9.79	0.03	8.75	22.75
			7	27.07	13.69	10.41	9.46	23.60
			12	39.91	21.30	7.87	13.16	51.06
	0.001	0.0005	0	10.56	3.52	13.87	4.98	40.70
			3	19.35	8.82	5.81	7.45	32.20
			7	26.68	13.56	11.67	9.28	32.38
			12	36.03	20.01	16.18	11.33	56.28

5.6 Elastic parameters

Assuming that the salt specimens are linearly elastic that the salt the elastic parameters are calculated for the three-dimensional principal stress-strain relations, given by Jaeger et.al. (2007). The relation can be simplified to obtain a set of governing equations for an isotropic material as follows:

$$G = (1/2)\ (\tau_{oct,e}/\gamma_{oct,e}) \tag{5.7}$$

$$3\sigma_{m,e} = (3\lambda + 2G)\ \Delta \tag{5.8}$$

$$E = 2G\ (1 + \nu) \tag{5.9}$$

$$\nu = \lambda / 2(\lambda + G) \tag{5.10}$$

where $\tau_{oct,e}$, $\gamma_{oct,e,}$ $\sigma_{m,e}$ and Δ are octahedral shear stress and strain, mean stress, and volumetric. Table 5.2 summarizes these stress and strain values and their corresponding elastic parameters. The calculations of the elastic parameters are made at 30-40% of the maximum principal stress as shown in Table 4.3. Based on this calculation the elastic modulus of the salt appears to increase with loading rate and decrease with temperature. It ranges from 9 to 24 GPa. The Poisson's ratios of the salt range from 0.37 to 0.47, and tend to be independent of the loading rate and temperature (Figures 5.6). The elastic parameters tend to be independent of the confining pressures. The elastic modulus and Poisson's ratio increase with loading rate. The poisson's ratio tends to be independent of the loading rate, the poisson's ratio tends to be independent of the temperatures. Their results agree reasonably well

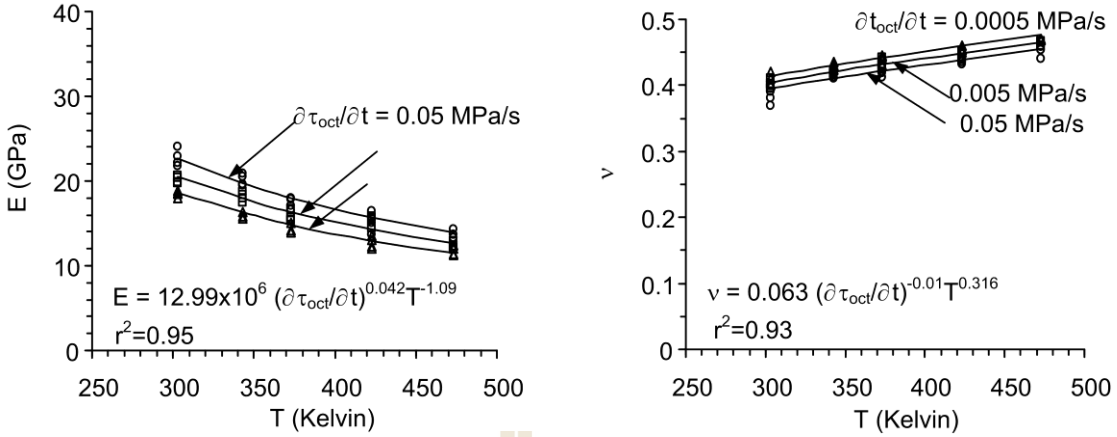

Figure 5.6 Elastic parameters of salt as a function of temperature.

with the results obtained here. The elastic modulus and Poisson's ratio between loading rate and temperature can be best represented by:

$$E = 12.99\times10^{6}\cdot(\partial\tau_{oct}/\partial t)^{0.042}T^{1.09} \tag{5.11}$$

$$\nu = 0.063\cdot(\partial\tau_{oct}/\partial t)^{-0.01}T^{0.316} \tag{5.12}$$

where E is the compressive elastic modulus, ν is $\partial\tau_{oct}/\partial t$ is the Poisson's ratio, the octahedral shear stress rate (in MPa/s) and T is temperature.

Table 5.2 Summarizes stress and strain values and their corresponding elastic parameters.

T (K)	$\partial\tau_{oct}/\partial t$ (MPa/s)	σ_3 (MPa)	$\sigma_{1,d}$ (MPa)	$\tau_{oct,d}$ (MPa)	$\gamma_{oct,d}$ (10^{-3})	$\sigma_{m,d}$ (MPa)	$\varepsilon_{m,d}$ (10^{-3})	E (GPa)	ν (GPa)	K (GPa)	G (GPa)
		3	21.0	8.5	12.2	9.0	1.4	22.9	0.43	58.6	13.19
		7	29.2	10.4	14.5	14.4	1.6	21.7	0.39	32.9	13.95
		12	35.0	10.8	15.9	19.7	2.1	22.2	0.38	30.8	14.61
	0.005	0	15.8	7.4	24.9	5.3	0.8	19.6	0.40	32.8	12.31
		3	19.0	7.5	12.2	8.3	2.8	19.8	0.43	47.3	11.55
		7	28.3	10.0	17.8	14.1	1.7	20.3	0.38	28.2	13.39
		12	33.3	10.0	18.0	19.1	1.7	20.5	0.40	34.3	12.86
	0.0005	0	12.6	5.9	25.7	4.2	3.0	18.6	0.37	23.8	12.58
		3	18.0	7.1	16.1	8.0	1.8	17.9	0.42	37.4	10.71
		7	23.3	7.7	16.6	12.4	1.2	18.8	0.43	44.9	10.96
		12	30.0	8.5	18.4	18.0	1.0	18.4	0.41	34.2	11.26
343	0.05	0	14.4	6.8	18.5	4.8	3.0	20.8	0.42	43.5	12.41
		3	19.3	7.7	15.5	8.4	2.8	20.5	0.42	41.0	12.31
		7	25.5	8.7	21.7	13.2	1.4	19.5	0.39	29.6	12.56
		12	31.3	9.1	24.6	18.4	3.5	19.4	0.41	36.0	11.86
	0.005	0	13.8	6.5	17.4	4.6	2.4	18.4	0.37	24.3	12.31
		3	16.5	6.4	15.3	7.5	4.6	18.7	0.43	44.5	10.92
		7	20.8	6.5	22.8	11.6	8.6	18.0	0.41	33.4	11.00
		12	27.4	7.3	21.0	17.1	6.2	17.4	0.45	58.2	9.70
	0.0005	0	10.7	5.0	16.4	3.6	2.9	16.2	0.43	38.0	9.50
		3	13.5	4.9	18.3	6.5	4.1	16.3	0.45	54.6	9.10
		7	18.6	5.5	20.7	10.9	5.7	15.8	0.43	39.9	9.11
		12	24.2	5.8	28.6	16.1	1.9	15.5	0.42	33.7	9.20
373	0.05	0	12.0	5.7	19.9	4.0	1.6	17.9	0.46	67.9	9.82
		3	16.6	6.4	16.7	7.5	2.4	17.1	0.46	78.3	9.22
		7	23.4	7.7	25.5	12.5	4.5	17.8	0.46	74.2	9.73
		12	25.6	6.4	17.7	16.5	2.2	16.5	0.44	46.0	9.42
	0.005	0	9.7	4.6	17.3	3.2	1.1	15.6	0.41	28.7	9.57
		3	15.4	5.8	19.4	7.1	2.6	15.3	0.44	42.6	8.73
		7	18.8	5.6	25.4	10.9	8.2	16.6	0.43	39.7	9.70
		12	22.3	4.8	20.5	15.4	1.7	15.4	0.44	42.8	8.77
	0.0005	0	8.9	4.2	15.2	3.0	0.8	14.1	0.43	33.6	8.21
		3	12.9	4.7	19.7	6.3	2.1	14.1	0.42	30.7	8.39
		7	16.5	4.5	31.0	10.2	1.4	15.0	0.45	50.2	8.37
		12	21.8	4.6	26.3	15.3	0.8	12.1	0.43	28.9	7.07

Table 5.2 Summarizes stress and strain values and their corresponding elastic parameters (cont.).

T (K)	$\partial\tau_{oct}/\partial t$ (MPa/s)	σ_3 (MPa)	$\sigma_{1,d}$ (MPa)	$\tau_{oct,d}$ (MPa)	$\gamma_{oct,d}$ (10^{-3})	$\sigma_{m,d}$ (MPa)	$\varepsilon_{m,d}$ (10^{-3})	E (GPa)	ν (GPa)	K (GPa)	G (GPa)
423	0.05	0	9.2	4.3	19.8	3.1	3.7	15.5	0.39	24.1	9.91
		3	15.4	5.8	14.5	7.1	2.8	16.5	0.45	56.2	9.14
		7	18.1	5.2	18.2	10.7	9.7	15.0	0.47	74.7	8.06
		12	25.1	6.2	21.6	16.4	2.6	13.6	0.46	64.6	7.37
	0.005	0	7.3	3.4	21.9	2.4	0.9	14.3	0.44	39.9	8.17
		3	12.3	4.4	15.4	6.1	3.1	15.7	0.45	57.4	8.66
		7	16.7	4.6	30.9	10.2	4.3	15.3	0.45	46.7	8.64
		12	21.0	4.2	28.9	15.0	1.8	15.8	0.47	82.0	8.48
	0.0005	0	6.2	2.9	19.3	2.1	2.6	14.2	0.45	47.4	7.90
		3	11.2	3.9	11.7	5.7	2.3	14.2	0.42	29.9	8.44
		7	15.1	3.8	26.0	9.7	14.6	14.2	0.43	34.0	8.30
		12	20.4	3.9	33.8	14.8	5.6	14.8	0.44	41.2	8.43
473	0.05	0	8.0	3.8	18.2	2.7	1.5	13.2	0.46	55.2	7.20
		3	12.8	4.6	13.5	6.3	6.1	13.6	0.45	49.4	7.53
		7	16.6	4.5	19.0	10.2	3.3	13.6	0.45	49.4	7.53
		12	21.4	4.4	19.4	15.1	1.4	10.4	0.47	50.4	5.63
	0.005	0	6.0	2.8	21.9	2.0	1.4	12.2	0.45	40.9	6.82
		3	11.1	3.8	11.4	5.7	2.1	14.6	0.45	52.4	8.09
		7	13.5	3.1	11.8	9.2	7.3	14.7	0.44	40.8	8.39
		12	20.0	3.7	25.5	14.7	5.5	13.1	0.45	46.9	7.26
	0.0005	0	5.3	2.5	20.4	1.8	9.7	8.4	0.47	46.9	4.49
		3	9.7	3.1	16.1	5.2	4.1	11.8	0.46	51.6	6.40
		7	13.3	3.0	16.2	9.1	8.2	9.9	0.46	46.9	5.32
		12	18.0	2.8	28.1	14.0	11.3	9.1	0.48	76.0	4.76

CHAPTER VI

STRENGTH CRITERIA

6.1 Introduction

The purpose of this chapter is to describe the strength and dilation criteria under various stress rates and temperatures. Two criteria are proposed: the octahedral shear stress and stress rate relation and the strain energy criteria.

6.2 Octahedral shear strength and stress rate relation

The test results obtained here are under a simplified condition where the stress increment is applied only along the major principal direction. Under in-situ conditions however the change with time of the stresses may occur in all three principal directions. An attempt is made to represent the effect of the loading rate under multiaxial conditions. For each specimen the octahedral shear stress rate is calculated as shown in equation (5.1). The octahedral shear stress and shear strains at dilation can also be calculated from the major principal stresses and the three principal strains at dilation as shown in equation (5.2).

Here the octahedral shear stresses at failure ($\tau_{oct,f}$) and at dilation ($\tau_{oct,d}$) are plotted as a function of the mean stresses in Figure 6.1 and octahedral shear stresses at failure ($\tau_{oct,f}$) and at dilation ($\tau_{oct,d}$) are plotted as a function of the shear rate ($\partial\tau_{oct}/\partial t$) in Figure 6.2.

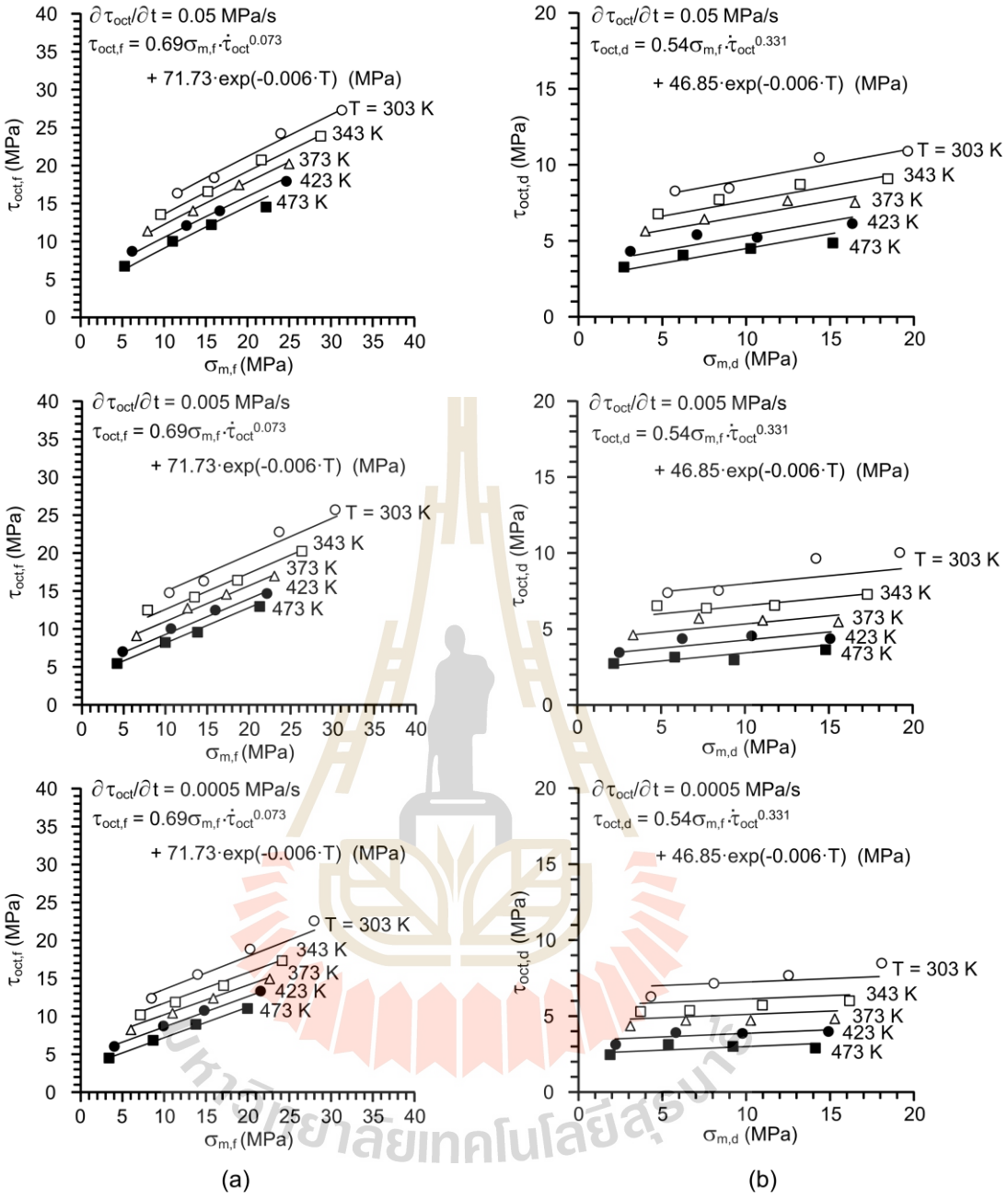

Figure 6.1 Octahedral shear stresses (τ_{oct}) at failure (a) and at dilation (b) as a function of mean stress (σ_m) for various temperatures (T) and shear rate ($\partial\tau_{oct}/\partial t$).

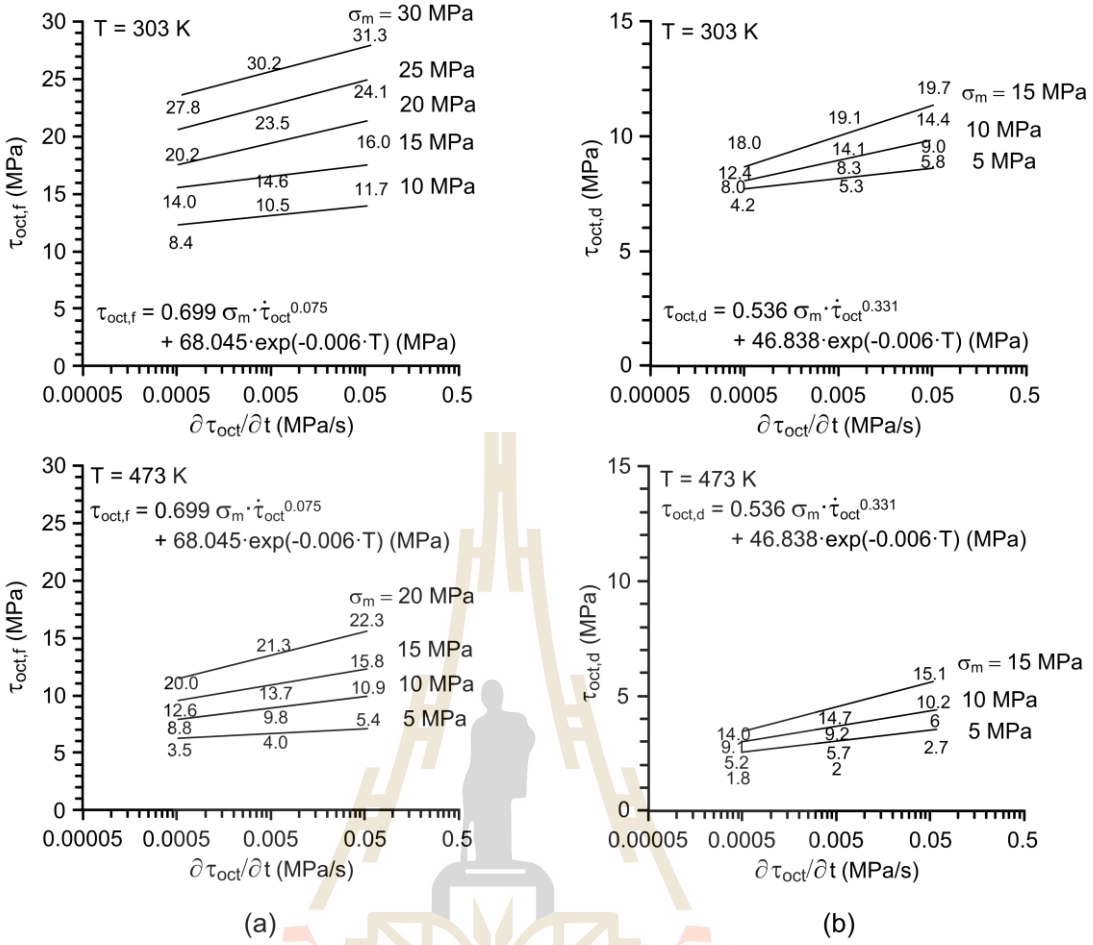

Figure 6.2 Octahedral shear stresses (τ_{oct}) at failure (a) and at dilation (b) as a function of shear rate ($\partial\tau_{oct}/\partial t$) for various mean stresses (σ_m).

The shear rate is determined by taking a derivative of Eq. (6.1) with respect to time (t). Since σ_3 is constant with time here, the following relation is obtained:

$$\tau_{oct} = \left(\sqrt{2}/3\right)\partial\sigma_1/\partial t \tag{6.1}$$

The numbers in Figure 6.2 represent the magnitudes of σ_m where their locations in the diagram indicate the corresponding magnitudes of shear rate and the octahedral shear stress at failure ($\tau_{oct,f}$) and at dilation ($\tau_{oct,d}$). Interpolation between these σ_m points allows derivation of the $\tau_{oct,f}$ and $\tau_{oct,d}$ as a function of $\partial\tau_{oct}/\partial t$ under the selected magnitudes of σ_m (5, 10, 15, 20 , 25 and 30 MPa), which can be best represented by:

$$\tau_{oct,f} = \alpha \cdot \sigma_m \cdot \dot{\tau}_{oct}^{\ \kappa} + \lambda \cdot \exp(\delta \cdot T) \quad \text{(MPa)} \tag{6.2}$$

$$\tau_{oct,d} = \alpha' \cdot \sigma_m \cdot \dot{\tau}_{oct}^{\ \kappa'} + \lambda' \cdot \exp(\delta' \cdot T) \quad \text{(MPa)} \tag{6.3}$$

where α, α', β, β', κ, κ', λ, λ',δ and δ' are empirical constants for the salt at failure and at dilation. The unit of shear rate ($\partial\tau_{oct}/\partial t$) and temperature (T) are MPa/s and Kelvin. The empirical constants are defined by regression analysis. Table 6.1 lists empirical constants from regression analysis of octahedral shear strength and shear rate relation at failure and at dilation. These empirical criteria may be used to predict a long-term strength and dilation of the salt under a given mean stress, shear rate and temperature.

Table 6.1 Empirical constants from regression analysis of octahedral shear strength and shear rate relation at failure and at dilation.

	$\tau_{oct,f} = \alpha \cdot \sigma_m \cdot \dot{\tau}_{oct}^{\ \kappa} + \lambda \cdot \exp(\delta \cdot T)$ (MPa)				R^2
At failure	α	κ	λ	δ	0.970
	0.699	0.075	68.045	-0.006	
	$\tau_{oct,d} = \alpha' \cdot \sigma_m \cdot \dot{\tau}_{oct}^{\ \kappa'} + \lambda' \cdot \exp(\delta' \cdot T)$ (MPa)				0.918
At dilation	α'	κ'	λ'	δ'	
	0.536	0.331	46.838	-0.006	

6.3 Octahedral shear strength and shear strain relation

The above criterion have been derived without taking the induced strains into consideration. Due to nonlinear behavior of the salt they may not be adequate to predict the rock strength or dilation under very low loading rates and high temperatures. This section proposes the shear strength and dilation criteria that take the corresponding shear strains into consideration. From the test results the octahedral shear stress can be calculated as a function of shear strain at failure and at dilation for various mean stress magnitudes, as shown in Figure 6.3.

The numbers in Figure 6.3. represent the magnitudes of σ_m where their locations indicate the corresponding magnitudes of the octahedral shear stress and strain at failure ($\tau_{oct,f}$) and at dilation ($\tau_{oct,d}$). Sets of empirical equations can be used to determine the variation of the octahedral shear stress with the octahedral shear strain at failure and at dilation for the selected σ_m magnitudes of 5, 10, 15, 20 and 25 MPa. The empirical equations can be written as:

$$\tau_{oct,f} = \psi \cdot \sigma_m^{\ \beta} \cdot \gamma_{oct}^{\ \omega} \cdot T^{\iota} \cdot (\partial \tau_{oct} / \partial t)^{\eta} \qquad \text{(MPa)} \qquad (6.4)$$

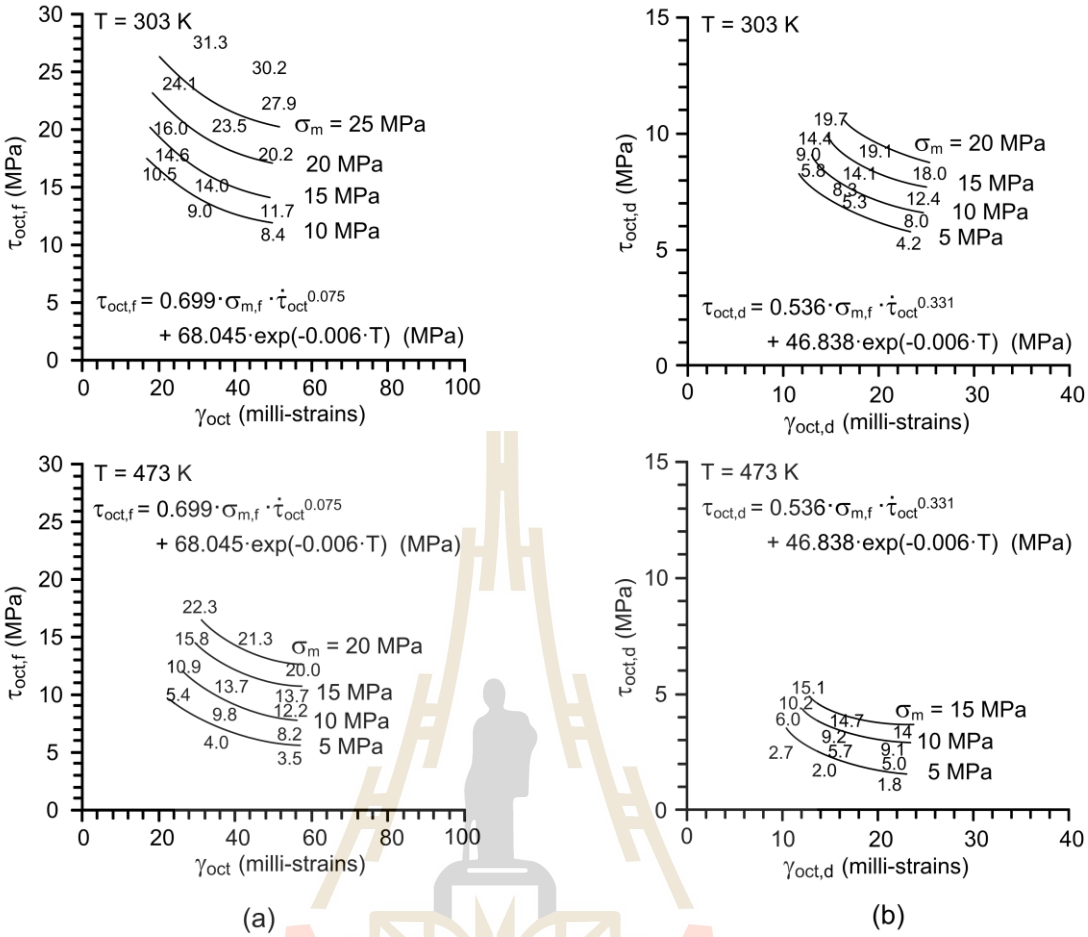

Figure 6.3 Octahedral shear stresses (τ_{oct}) at failure (a) and at dilation (b) as a function of shear strain (γ_{oct}) for various mean stresses (σ_m).

$$\tau_{oct,d} = \psi' \cdot \sigma_m^{\beta'} \cdot \gamma_{oct}^{\omega'} \cdot T^{\iota'} \cdot (\partial\tau_{oct}/\partial t)^{\eta'} \quad \text{(MPa)} \quad (6.5)$$

where ψ, ψ', β, β', ω, ω', ι, ι', η and η' are empirical constants for the salt at failure and at dilation. The unit of shear strain (γ_{oct}), shear rate ($\partial\tau_{oct}/\partial t$) and temperature (T) are strain, MPa/s and Kelvin. The empirical constants are defined as shown in Table 6.2. listing empirical constants from regression analysis of octahedral shear strength and shear strain relation at failure and at dilation.

Table 6.2 Empirical constants from regression analysis of octahedral shear strength and shear strain relation at failure and at dilation.

	$\tau_{oct,f} = \psi \cdot \sigma_m^{\beta} \cdot \gamma_{oct}^{\omega} \cdot T^{\iota} \cdot (\partial\tau_{oct}/\partial t)^{\eta}$ (MPa)					R^2
At failure	ψ	β	ω	ι	η	0.982
	2.81×10^3	0.493	0.037	-1.105	0.045	
	$\tau_{oct,d} = \psi' \cdot \sigma_m^{\beta'} \cdot \gamma_{oct}^{\omega'} \cdot T^{\iota'} \cdot (\partial\tau_{oct}/\partial t)$					0.950
At dilation	ψ'	β'	ω'	ι'	η'	
	276.86×10^3	0.170	-0.018	-1.818	0.068	

6.4 Strain energy density criterion

The strain energy density principle is applied here to describe the salt strength and deformability under different loading rates and temperatures. A similar approach was used by Fuenkajorn et al. (2012) to derive a loading rate-dependent strength criterion for salt. The distortional strain energy at failure (W_d) and at dilation ($W_{d,d}$) can be calculated from the octahedral shear stresses and strains for each salt specimen (Table 6.3) using the relations given by Jaeger et al. (2007):

$$W_d = (3/2)\cdot \tau_{oct,f} \cdot \gamma_{oct,f} \tag{6.6}$$

$$W_{d,d} = (3/2)\cdot \tau_{oct,d} \cdot \gamma_{oct,d} \tag{6.7}$$

The distortion strain energy at failure (W_d) and at dilation ($W_{d,d}$) can also be derived as a function of the mean strain energy density at dilation ($W_{m,d}$). They can be calculated from $\sigma_{1,d}$, $\varepsilon_{1,d}$, $\varepsilon_{2,d}$ and $\varepsilon_{3,d}$ as follows.

$$W_m = (3/2)\cdot \sigma_m \cdot \varepsilon_m \tag{6.8}$$

$$W_{m,d} = (3/2)\cdot \sigma_{m,d} \cdot \varepsilon_{m,d} \tag{6.9}$$

$$\sigma_{m,d} = (1/3)\cdot (\sigma_{1,d} + 2\sigma_3) \tag{6.10}$$

$$\varepsilon_{m,d} = (1/3)\cdot (\varepsilon_{1,d} + \varepsilon_{2,d} + \varepsilon_{3,d}) \tag{6.11}$$

Figure 6.4 shows a linear relation of $W_{d,d}$ -$W_{m,d}$ which can be represented by:

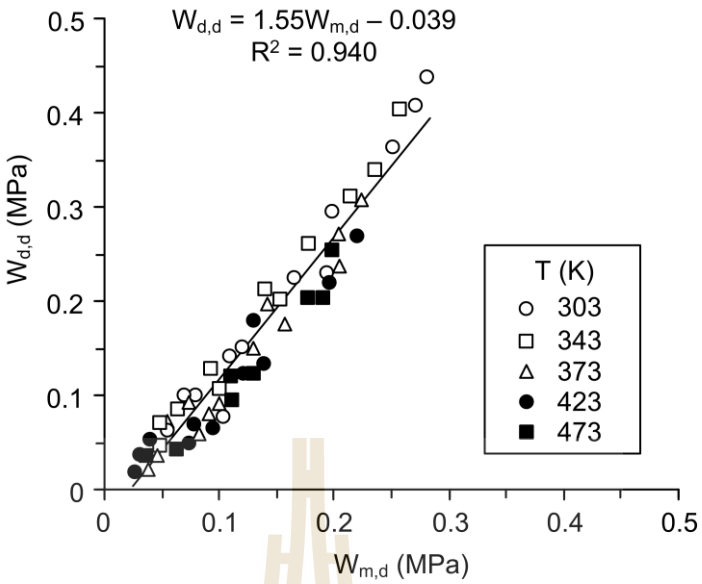

Figure 6.4 Distortional strain energy at dilation ($W_{d,d}$) as a function mean strain energy at dilation ($W_{m,d}$).

$$W_{d,d} = 1.55W_{m,d} - 0.039 \quad \text{(MPa)} \tag{6.12}$$

This criterion considers both stress and strain at dilation, and hence isolating the effect of stress rate and temperature. If the salt temperature is known, its strength can be determined from equation (6.12) regardless the loading rate. The derived criteria will be used to evaluate the mechanical stability of compress-air storage cavern to be presented in the following chapter.

Table 6.3 Strain energy density at failure and at dilation under various loading rates and temperatures.

T (K)	$\partial\tau_{oct}/\partial t$ (MPa/s)	σ_3 (MPa)	W_d (MPa)	W_m (MPa)	$W_{d,d}$ (MPa)	$W_{m,d}$ (MPa)
303	0.05	0	0.96	0.04	0.24	0.01
		3	0.67	0.05	0.17	0.02
		7	1.06	0.09	0.26	0.04
		12	1.30	0.14	0.33	0.06
	0.005	0	1.11	0.02	0.28	0.01
		3	0.60	0.09	0.15	0.03
		7	1.25	0.09	0.31	0.04
		12	1.39	0.11	0.35	0.05
	0.0005	0	0.92	0.05	0.23	0.02
		3	0.75	0.05	0.19	0.02
		7	0.93	0.05	0.23	0.02
		12	1.25	0.06	0.31	0.03
343	0.05	0	0.75	0.06	0.19	0.02
		3	0.77	0.09	0.19	0.04
		7	1.35	0.07	0.34	0.03
		12	1.76	0.22	0.44	0.10
	0.005	0	0.68	0.04	0.17	0.02
		3	0.64	0.13	0.16	0.05
		7	1.12	0.34	0.28	0.15
		12	1.27	0.35	0.32	0.16
	0.0005	0	0.50	0.04	0.12	0.02
		3	0.61	0.10	0.15	0.04
		7	0.88	0.21	0.22	0.09
		12	1.48	0.10	0.37	0.05
373	0.05	0	0.68	0.03	0.17	0.01
		3	0.70	0.07	0.18	0.03
		7	1.44	0.18	0.36	0.08
		12	0.98	0.12	0.25	0.05
	0.005	0	0.47	0.02	0.12	0.01
		3	0.74	0.07	0.19	0.03
		7	1.10	0.30	0.28	0.14
		12	0.94	0.08	0.24	0.04
	0.0005	0	0.38	0.01	0.10	0.00
		3	0.62	0.05	0.16	0.02
		7	1.14	0.05	0.29	0.02
		12	1.18	0.04	0.29	0.02

Table 6.3 Strain energy density at failure and at dilation under various loading rates and temperatures (cont.).

T (K)	$\partial\tau_{oct}/\partial t$ (MPa/s)	σ_3 (MPa)	W_d (MPa)	W_m (MPa)	$W_{d,d}$ (MPa)	$W_{m,d}$ (MPa)
423	0.05	0	0.52	0.05	0.13	0.02
		3	0.56	0.08	0.14	0.03
		7	0.75	0.35	0.19	0.16
		12	1.17	0.14	0.29	0.06
	0.005	0	0.45	0.01	0.11	0.01
		3	0.46	0.07	0.12	0.03
		7	1.16	0.14	0.29	0.07
		12	1.23	0.09	0.31	0.04
	0.0005	0	0.34	0.02	0.08	0.01
		3	0.31	0.05	0.08	0.02
		7	0.85	0.46	0.21	0.21
		12	1.37	0.26	0.34	0.12
473	0.05	0	0.41	0.02	0.10	0.01
		3	0.42	0.14	0.10	0.06
		7	0.70	0.11	0.18	0.05
		12	0.85	0.07	0.21	0.03
	0.005	0	0.37	0.01	0.09	0.01
		3	0.30	0.04	0.07	0.02
		7	0.33	0.21	0.08	0.10
		12	1.01	0.25	0.25	0.12
	0.0005	0	0.30	0.07	0.08	0.03
		3	0.36	0.08	0.09	0.03
		7	0.45	0.24	0.11	0.11
		12	0.96	0.49	0.24	0.24

CHAPTER VII

COMPUTER SIMULATIONS

7.1 Introduction

This chapter describes the method and results of finite difference analysis using FLAC (Itasca, 1992) to simulate single isolated CAES caverns in the Maha Sarakham salt. The objective is to apply the criteria derived in the preview chapter to determine the safe maximum withdrawal rate of the compressed-air from the salt caverns. The principal stresses and strains induced in the surrounding salt under various air withdrawal rates are calculated and compared against the criteria. The results can determine the safe maximum withdrawal rate of compressed-air energy storage (CAES) caverns in the Maha Sarakham salt formation.

7.2 Numerical simulation

Finite difference analyses (FLAC 4.0) are performed to determine the stresses and strains at the boundaries of CAES caverns for various reduction rates of the internal pressures. Figure 7.1 shows the mesh modal representing the cavern from the ground surface to the depth of 1000 m. The cavern is up-right cylinder with the casing shoe (cavern top) at 500 m. The cavern diameter and height are 50 m and 500 m. These cavern shape and depth have been under consideration by the Thailand office of energy.

The in-situ stress is assumed to be hydrostatic. Before cavern development the salt stress at the casing shoe depth (σ_{cs}) is calculated as 10.8 MPa for casing shoe

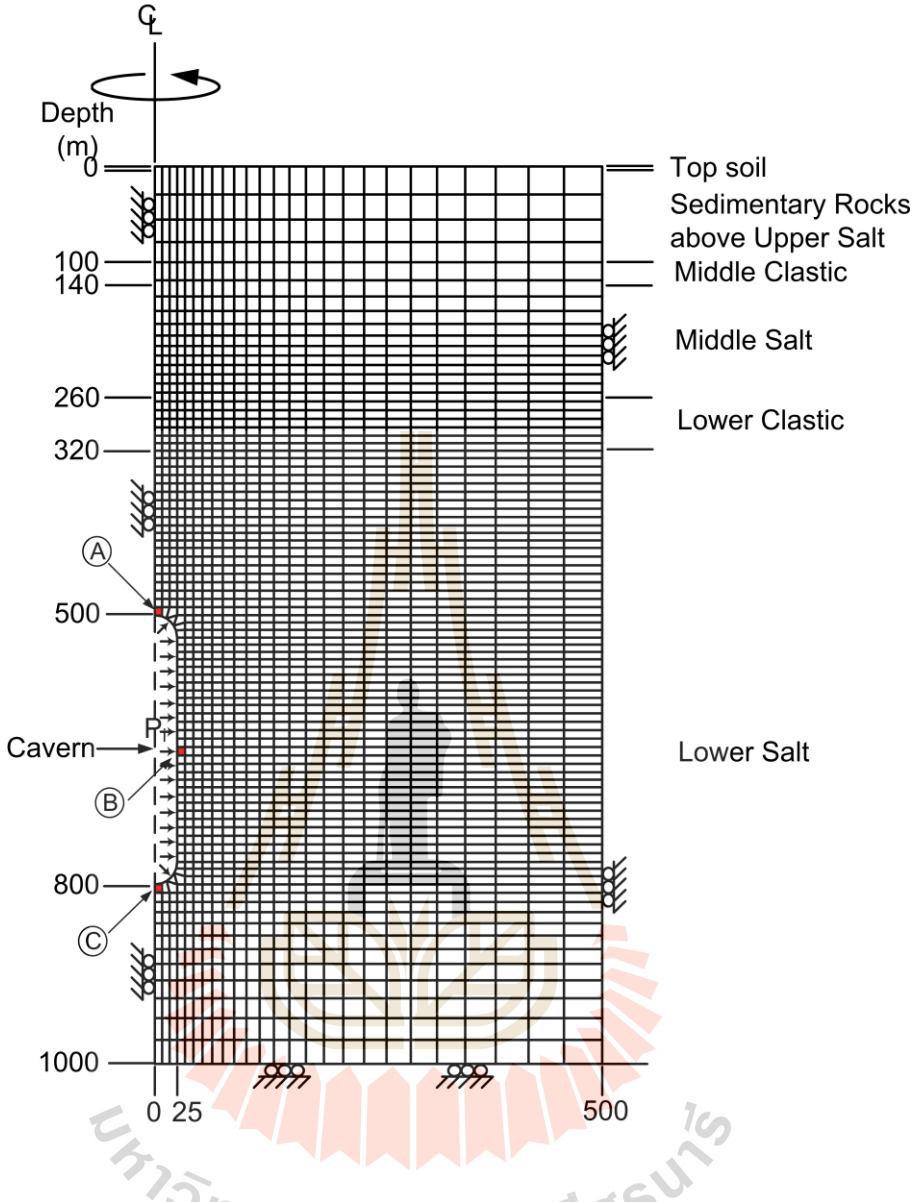

Figure 7.1 Finite difference mesh developed for FLAC simulation of CAES cavern.

at 500 m. The maximum cavern pressure is defined as $0.9\sigma_{cs}$ minimum (90% of the in situ-stress at casing shoe) the minimun cavern pressure is $0.1\sigma_{cs}$ (10% of the in situ stress at casing shoe).

Several cases are simulated for four different rates of cavern pressure withdrawal. The equivalent pressure schemes are calculated by assuming that the air injection and retrieval periods are equal.

The Maha Sarakham salt is assumed to behave as the Burgers material. The Burgers constitutive equation is a built-in program in FLAC (Itasca, 1992); as follows:

$$\gamma_{oct} = \tau_{oct}\left[\left(\frac{t}{\eta_1}+\frac{1}{E_1}+\frac{\eta_1}{\eta_2 E_2}\right)-\left(\frac{\eta_1}{\eta_2 E_2}\exp\left(\frac{-E_2 t}{\eta_2}\right)\right)\right] \quad (7.1)$$

where τ_{oct} is octahedral shear stresses (MPa), t is time (day), E_1 is elastic modulus (GPa), E_2 is spring constant in visco-elastic phase (GPa), η_1 is visco-plastic coefficient in steady-state phase (GPa.day) and η_2 is visco-elastic coefficient in transient phase (GPa.day).

Figure 7.2 shows the modular components of the Burgers model. The Burgers parameters for the Maha Sarakham salt are obtained from the calibration results of creep tests of Samsri (2010). The parameters are given in Table 7.1.

Tables 7.2 and 7.3 give the simulation results in terms of the mean stresses and strains, octahedral shear stresses and strains and distortional and mean strain energy at the roof, side wall and floor of the cavern (points A, B and C - Figure 7.1) under ambient temperature and 200 ºC. For all cases the magnitudes of the mean and shear stresses and strains decrease with the withdrawal rate.

7.3 Factor of safety calculation

For a conservative design the surrounding salt is not allowed to dilate during the withdrawal period. This is to ensure the long-term stability of the storage cavern under loading. As a result the three dilation criteria are used here to calculate the factor of safety (FS) of the salt at the bottom of the cavern. These include

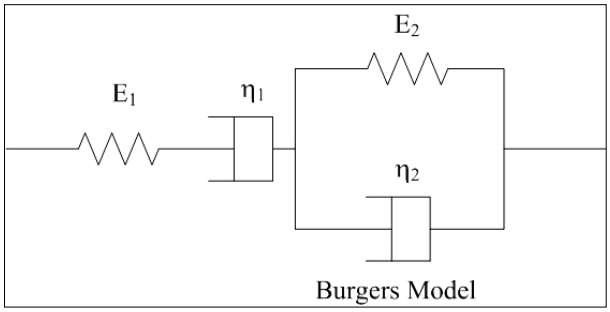

Figure 7.2 Modular components of the Burgers model.

Table 7.1 Material parameters used in FLAC simulations.

Parameters	Symbols	Units	Values
Elastic modulus	E_1	GPa	1.183
Spring constant in visco-elastic phase	E_2	GPa	3.109
visco-plastic coefficient in steady-state phase	η_1	GPa.day	64.593
visco-elastic coefficient in transient phase	η_2	GPa.day	0.647

Table 7.2 Stressed, strains and strains energy at cavern roof, side wall and floor based on criteria for all under ambient temperature.

	Pressure scheme	**Pressure withdrawal rate (MPa/day)**	**σ_m (MPa)**	**ε_m (10^{-3})**	**τ_{oct} (MPa)**	**γ_{oct} (10^{-3})**	**W_d (MPa)**	**W_m (MPa)**
Roof	1 cycle/day	8.64	12.1	6.7	3.2	74.5	0.36	0.12
	15cycles/month	4.32	12.0	5.9	3.1	41.0	0.19	0.11
	1 cycle/month	0.28	10.9	5.3	2.9	17.3	0.08	0.09
	6 cycles/year	0.14	10.0	5.0	2.5	12.0	0.05	0.08
Side Wall	1 cycle/day	8.64	14.1	10.0	5.4	95.7	0.77	0.21
	15cycles/month	4.32	14.0	9.9	5.2	66.4	0.52	0.21
	1 cycle/month	0.28	13.6	7.9	4.8	25.0	0.18	0.16
	6 cycles/year	0.14	13.3	5.0	4.5	12.0	0.08	0.10
Floor	1 cycle/day	8.64	18.9	7.7	6.5	68.2	0.67	0.22
	15cycles/month	4.32	18.8	5.9	6.3	47.4	0.45	0.17
	1 cycle/month	0.28	17.5	4.9	5.5	18.6	0.16	0.13
	6 cycles/year	0.14	16.6	4.3	5.1	14.1	0.11	0.11

Table 7.3 Stressed, strains and strains energy at cavern roof, side wall and floor based on criteria under 200ºC.

	Pressure scheme	**Pressure withdrawal rate (MPa/day)**	**σ_m (MPa)**	**ε_m (10^{-3})**	**τ_{oct} (MPa)**	**γ_{oct} (10^{-3})**	**W_d (MPa)**	**W_m (MPa)**
Roof	1 cycle/day	8.64	12.92	7.04	3.87	79.80	0.46	0.14
	15cycles/month	4.32	12.69	6.51	3.60	49.68	0.27	0.12
	1 cycle/month	0.28	12.48	6.38	3.31	23.12	0.12	0.12
	6 cycles/year	0.14	10.66	4.74	2.98	12.69	0.06	0.08
Side Wall	1 cycle/day	8.64	14.31	10.24	5.61	101.4	0.86	0.22
	15cycles/month	4.32	14.15	10.06	5.37	69.83	0.56	0.21
	1 cycle/month	0.28	13.90	8.16	5.07	25.69	0.20	0.17
	6 cycles/year	0.14	13.64	7.11	4.67	20.32	0.14	0.15
Floor	1 cycle/day	8.64	19.48	8.34	84.90	84.90	0.80	0.24
	15cycles/month	4.32	19.46	7.84	70.86	70.86	0.68	0.23
	1 cycle/month	0.28	18.59	5.15	19.56	19.56	0.18	0.14
	6 cycles/year	0.14	17.91	4.53	15.32	15.32	0.13	0.12

$\tau_{oct,d}$ - $\tau_{oct,d}$ - $\gamma_{oct,d}$ criterion and $W_{d,d} - W_{m,d}$ criterion. The two temperatures are used under isothermal condition ambient temperature and 200 ºC.

The FS calculation methods and results for all pressure schemes are shown in Tables 7.4 for ambient temperature, and in Tables 7.5 for temperature at 200 ºC. The three criteria give different FS values. The $\tau_{oct,d}$ - $\gamma_{oct,d}$ criterion tends to give the largest FS values for all cases. This criterion does not consider the mean stresses and strains induced around the cavern. The FS values obtained from applying the $\tau_{oct,d}$ - $\partial\tau_{oct}/\partial t$ criterion are lower than the previous criterion. This criterion does not consider the mean stresses and strains induced around the cavern. The simulation results indicate that the safety withdrawal rates are increase with decreasing withdrawal rate. As shown in Tables7.3 for all criteria the factors of safety.

The $W_{d,d} - W_{m,d}$ criterion gives the most conservative results. It shows the FS values lower than 1.0 for the withdrawal rates of 1 cycle/day and 15 cycles/month. This criterion is perhaps the most appropriate for use in the design of the withdrawal rate because it incorporates both shear and mean stresses and strains.

Table 7.4 Factor of safety at cavern roof, sidewall and floor for all under ambient temperature.

Criterion	Pressure scheme	Factor of Safety		
		Roof	**Side wall**	**Floor**
$\tau_{oct,d} - \gamma_{oct,d}$	1 cycle/day	1.54	1.16	0.99
	15cycles/month	1.60	1.21	1.11
	1 cycle/month	1.86	1.52	1.35
	6 cycles/year	2.07	1.68	1.42
$\tau_{oct,d} - \partial\tau_{oct}/\partial t$	1 cycle/day	2.48	1.42	1.26
	15cycles/month	2.54	1.47	1.29
	1 cycle/month	2.66	1.59	1.40
	6 cycles/year	3.11	1.70	1.53
$W_{d,d} - W_{m,d}$	1 cycle/day	0.55	0.48	0.45
	15cycles/month	0.65	0.55	0.49
	1 cycle/month	1.26	1.18	1.03
	6 cycles/year	1.72	1.40	1.20

Table 7.5 Factor of safety at cavern roof, sidewall and floor for all under 200 ºC.

Criterion	Pressure scheme	Factor of Safety		
		Roof	Side wall	Floor
$\tau_{oct,d} - \gamma_{oct,d}$	1 cycle/day	1.45	1.06	0.87
	15cycles/month	1.53	1.11	0.97
	1 cycle/month	1.76	1.20	1.15
	6 cycles/year	1.94	1.28	1.22
$\tau_{oct,d} - \partial\tau_{oct}/\partial t$	1 cycle/day	2.10	1.36	1.11
	15cycles/month	2.20	1.42	1.26
	1 cycle/month	2.33	1.50	1.28
	6 cycles/year	2.58	1.63	1.35
$W_{d,d} - W_{m,d}$	1 cycle/day	0.37	0.35	0.43
	15cycles/month	0.57	0.52	0.46
	1 cycle/month	1.27	1.15	1.01
	6 cycles/year	1.39	1.31	1.13

CHAPTER VIII

DISCUSSIONS, CONCLUSIONS AND RECOMMENDATIONS FOR FUTURE STUDIES

8.1 Discussions

- The numbers of the test specimens seem adequate, as evidenced by the good coefficients of correlation for all loading rate and temperatures.

- The test results in terms of the stress-strain relations and strengths are believed to be reliable. They are agreed reasonably well with the related test results on the Maha Sarakham salt obtained by Sriapai et al. (2012), Sriapai et al. (2013) Sartkaew (2013).

- A difficulty is the control rate of the applied principal stresses to obtain the desired test. High precision electronic pressure gage is used here while the pressures in the hydraulic load cells are manually controlled. Results of the specimens that are subjected to the stresses that deviate for the designed schemes have been discarded.

- A difficulty is the controlling the temperatures to obtain the desired test. A thermostat (Figure 4.2) is a component of a control system which senses the temperature of a system so that the system's temperature is maintained near a desired setpoint. . The accuracy is ± 0.3%FS + 1digit.

- The specimens size used in this study are relatively small. Recognizing the size effects on the rock strengths (Jaeger et al., 2007), larger specimens should be used. In summary the strengths obtained here under all test schemes would

overestimate the strength of the salt under in-situ condition due to the scale effect. Nevertheless, the issue of the size effect would not change the main conclusions drawn here that the failure stresses increase with the loading rates and decreases of the compressive strengths with increasing temperatures.

- The advantage of the application of the stain energy criterion over the octahedral shear-mean stress criterion is that it considers both stress and strain at failure, and hence their results would be more comprehensive than the octahedral shear-mean stress criterion.

8.2 Conclusions

The failure stresses increase with the loading rates, which agree with the experimental results on rock salt performed by Fuenkajorn et al., (2012) and Dubey and Gairola (2005). The testing is assumed to be under isothermal conditions (constant temperature with time during loading). The decreases of the compressive strengths with increasing temperatures agree with the experimental results Sriapai et al.,(2012) Vosteen and Schellschmidt, (2003) and Adhikary, (2010). Their results indicate that the compressive strengths of the salt decrease with increasing temperatures. The decrease of the salt strength as the temperature increases suggests that the applied thermal energy before the mechanical testing makes the salt weaker, and more plastic, failing at lower stress and higher strain with lower elastic moduli. The salt elastic modulus varies from 9 to 24 GPa. The Poisson's ratio from 0.37 to 0.47, and tend to be independent of the loading rate and temperature.

Several forms of the strength and dilation criteria have been derived. The $\tau_{oct,f}$ - $\partial\tau_{oct}/\partial t$ and $\tau_{oct,d}$ - $\partial\tau_{oct}/\partial t$ criteria are the simplest. They do not consider the induced

strains, but incorporate the effects of the shear rate and temperature into their formulation. The shear strain induced at dilation and failure are added into the formulation of the $\tau_{oct,f}$ - $\gamma_{oct,f}$ and $\tau_{oct,d}$ - $\gamma_{oct,d}$ criteria to implicitly consider the rate and temperature effects.

Assuming that the rock salt is linearly elastic before failure, the distortional strain energy ($W_{d,d}$) at dilation can be calculated as a function of mean strain energy ($W_{m,d}$). For a given $W_{m,d}$ the $W_{d,d}$ decreases with increasing temperature. The strain energy criterion agrees well with the strength results from different temperature.

The criteria proposed above can be used in the calculation of factor of safety of salt cavern. The Burgers model has been used in the FLAC simulation to determine the stresses and strains around the CAES cavern. The results are compared against criteria developed above for calculate the maximum withdrawal rate of the compressed-air storage cavern. The $W_{d,d} - W_{m,d}$ criterion gives the most conservative results. It shows the FS values lower than 1.0 for the withdrawal rates of 1 cycle/day and 15 cycles/month. This criterion is perhaps the most appropriate for use in the design of the withdrawal rate because it incorporates both shear and mean stresses and strains.

8.3 Recommendations for future studies

The test specimens here are relatively small. Testing on larger specimens is desirable to confirm the research findings. Verification of the compression test proposed concept should be tested under a wider range of salt from other sources. The effect of cyclic thermal and mechanical loading should be assessed. More testing is needed

to confirm the applicability and limitations of the proposed, such as true triaxial test, multi-step triaxial loading, and triaxial cyclic loading test.

REFERENCES

Allemandou, X. and Dusseault, M.B. (1996). Procedures for cyclic creep testing of salt rock, results and discussions. In **Proceedings of the Third Conference on the Mechanical Behavior of Salt** (pp. 207-218). Clausthal-Zellerfeld, Germany: Trans Tech Publications.

ASTM D2664. Standard test method for triaxial compressive strength of undrained rock core specimens without pore pressure measurements. In **Annual Book of ASTM Standards** (Vol. 04.08). Philadelphia: American Society for Testing and Materials.

ASTM D2938. Standard test method for unconfined compressive strength of intact rock core specimens. In **Annual Book of ASTM Standards** (Vol. 04.08). Philadelphia: American Society for Testing and Materials.

ASTM D3967. Standard test method for splitting tensile strength of intact rock core specimens. In **Annual Book of ASTM Standards** (Vol. 04.08). Philadelphia: American Society for Testing and Materials.

ASTM D4405. Standard test method for creep of cylindrical soft rock core specimens in uniaxial compressions. In **Annual Book of ASTM Standards** (Vol. 04.08). Philadelphia: American Society for Testing and Materials.

ASTM D4543. Standard practice for preparing rock core specimens and determining dimensional and shape tolerances. In **Annual Book of ASTM Standards** (Vol. 04.08). Philadelphia: American Society for Testing and Materials.

Aubertin, M. (1996). On the physical origin and modeling of kinematics and isotropic hardening of salt. In **Proceedings of the Third Conference on the Mechanical Behavior of Salt** (pp. 1-18). Clausthal-Zellerfeld, Germany: Trans Tech Publications.

Aubertin, M., Gill, D. E. and Ladanyi, B. (1992). Modeling the transient inelastic flow of rock salt. In **Proceedings of the Seventh Symposuim on Salt** (vol. 1, pp. 93-104). Elsevier Science Pub.

Aubertin, M., Julien M. R., Servant, S. and Gill, D. E. (1999). A rate-dependent model for the ductile behavior of salt rocks. **Canadian Geotechnical Journal.** 36(4): 660-674.

Aubertin, M., Sgaoula, J. and Gill, D. E. (1992). A damage model for rock salt: Application to tertiary creep. In **Proceedings of the Seventh Symposuim on Salt** (vol. 1, pp. 117-125). Elsevier Science Pub.

Aubertin, M., Sgaoula, J. and Gill, D. E. (1993). Constitutive modeling of rock salt: Basic considerations for semi-brittle behavior. In **Proceedings of the Fourth International Symposuim on Plasticity and It's Current Applications** (pp. 92). Baltimore.

Aubertin, M., Sgaoulla, J., Servant, S., Julien, M. R., Gill, D. E. and Ladanyi, B. (1998). An upto-date version of SUVIC-D for modeling the behavior of salt. In **Proceedings of the Fourth Conference on the Mechanical Behavior of Salt** (pp. 205-220). Clausthal,Germany: Trans Tech Publications.

Chokski, A. H. and Langdon, T. G. (1991). Characteristics of creep deformation in ceramics. **Materails Science and Technology** 7: 577-584.

Cleach, J.M.L., Ghazali, A., Deveughele, H., and Brulhet, J. (1996). Experimental study of the role of humidity on the thermomechanical behavior of various halitic rocks. In **Proceedings of the Third Conference on the Mechanical Behavior of Salt** (pp. 231-236). Clausthal-Zellerfeld, Germany: Trans Tech Publications.

Cristescu, N. and Hunsche, U. (1996). A comprehensive constitutive equation for rock salt determination and application. In **Proceedings of the Third Conference on the Mechanical Behavior of Salt** (pp. 191-205). Clausthal-Zellerfeld, Germany: Trans Tech Publications.

Dusseault, M.B. and Fordham, C.J. (1993). Time-dependent behavior of rocks. **Comprehensive Rock Engineering Principles, Practice and Project: Rock Testing and Site Characterization** (Vol. 3, pp. 119-149). London, Pergamon.

Dwivedi, R.D., Goel, R.K., Prasada, V.V.R. and Sinhab, A. (2008). Thermo-mechanical properties of Indian and other granites. **International Journal of Rock Mechanics and Mining Sciences** 45 (2008): 303-315.

Farmer, I.W. and Gilbert, M.J. (1984). Time dependent strength reduction of rock salt. In **Proceedings of the First Conference on the Mechanical Behavior of Salt** (pp. 3-18). Clausthal-Zellerfeld, Germany: Trans Tech Publications.

Fokker, P. A. (1995). **The behavior of salt and salt caverns**. Ph.D Thesis, Delft University of Technolgoy.

Fokker, P. A. (1998). The micro-mechanics of creep in rock salt. In **Proceedings of the Fourth Conference on the Mechanical Behavior of Salt** (pp. 49-61). Clausthal-Zellerfeld, Germany: Trans Tech Publications.

Fokker, P. A. and Kenter, C. J. (1994). The micro mechanical description of rock salt plasticity. In **Eurock'94** (pp. 705-713). Rotterdam: Balkema.

Franssen, R.C.M. and Spiers, C.J. (1990). Deformation of polycrystalline salt in compression and in shear at 250-350°C. Deformation Mechanisms, Rheology and Tectonics, **Geological Society Special Publication** (Vol. 45, pp. 201-213).

Fuenkajorn, K, Sriapai, T., and Samsri, P. (2012). Effects of loading rate on strength and deformability of Maha Sarakham salt. **Engineering Geology**, 135-136(2012): 10-23**.**

Fuenkajorn, K. and Daemen, J. J. K. (1988). **Boreholes closure in salt**. Technical Report Prepared for The U.S. Nuclear Regulatory Commission. Report No. NUREG/CR-5243 RW. University of Arizona.

Fuenkajorn, K. and Phueakphum, D. (2010). Effects of cyclic loading on mechanical properties of Maha Sarakham salt. **Engineering Geology**. 112 (1-4) 43-52.

Fuenkajorn, K., Walsri, C., and P hueakphum, D. (2011). Intrinsic variability of the mechanical properties of Maha Sarakham salt. **Quarterly Journal of Engineering Geology and Hydrogeology** 44 : 445-456.

Hamami, M., Tijani, S.M., and Vouille, G. (1996). A methodology for the identification of rock salt behavior using multi-step creep tests. In **Proceedings of the Third Conference on the Mechanical Behavior of Salt** (pp. 53-66). Clausthal-Zellerfeld, Germany: Trans Tech Publications.

Hunsche, U. and Schulze, O. (1996). Effect of humidity and confining pressure on creep of rock salt. In **Mechanical Behavior of salt, Series on Soil and Rock Mechanics** (Vol. 20, pp. 237-248). Trans Tech Publications.

Inada, Y., Kinoshita, N., Ebisawa, A., and Gomi, S. (1997). Strength and deformation characteristics of rocks after undergoing thermal hysteresis of high and low temperatures. **International Journal of Rock Mechanics and Mining Sciences** 34 (3-4): 688-702.

Jeremic, M. L. (1994). **Rock mechanics in salt mining** (530 pp.). Rotherdam: A. A. Balkema.

Kensakoo, T. (2006). Relationship between mineralogy and engineering properties of rock salt. M.S. Thesis, Suranaree University of Tehnolgy, Thailand.

Knowles, M. K., Borns, D., Fredrich, J., Holcomb, D., Price, R. and Zeuch, D. (1998). Testing the disturbed zone aroud a rigid inclusion in salt. In **Proceedings of the Fourth Conference on the Mechanical Behavior of Salt** (pp. 175-188). Clausthal, Germany: Trans Tech Publications.

Munson, D. E. and Wawersik, W. R. (1993). Constitutive modeling of salt behavior – State ofthe technology. In **Proceedings of the Seventh International Congess on Rock Mechanics** (vol. 3, pp. 1797-1810). Balkema.

Pudewills, A. and DrostePapp, J. (2003). Numerical modeling of the thermomechanical behavior of a large-scale underground experiment. **Computers & Structures** (81 (2003): 911-918).

Raj, S.V. and Pharr, G.M. (1992). Effect of temperature on the formation of creep substructure in sodium chloride single crystal. **American Ceramic Society** 75 (2): 347-352.

Samsri, P. Sriapai, T. Walsri C. and Fuenkajorn K., 2011. Polyaxial creep testing of rock salt. **Proceedings of the Second Thailand Rock Mechanics Symposium**. Nakhon Ratchasima: Suranaree University of Technology.

Samsri, P., Sriapai, T., Walsri ,C. and Fuenkajorn, K. (2010). Polyaxial creep testing of rock salt. In **Proceedings of the Third Thailand Symposium on Rock Mechanicson** (pp. 125-132). Thailand.

Senseny, P.E., Handin, J.W., Hansen, F.D., and Russell, J.E. (1992). Mechanical behavior of rock salt: phenomenology and micro-mechanisms. **International Journal of Rock Mechanics and Mining Sciences** 29 (4): 363-378.

Sriapai, T., Samsri, P. and Fuenkajorn, K. (2011). Influence of loading rate on compressive strength of rock salt. In **Proceedings of the Third Thailand Symposium on Rock Mechanicson** (pp. 117-124). Thailand.

Sriapai, T., Walsri, C. and Fuenkajorn, K. (2012). Effect of temperature on compressive and tensile strengths of salt. **ScienceAsia,** 38(2012): 166-174.

Wanten, P.H., Spiers, C.J., and Peach, C.J. (1996). Deformation of NaCl single crystals at 0.27Tm < T < 0.44Tm. In **Proceedings of the Third Conference on the Mechanical Behavior of Salt** (pp. 117-128). Clausthal-Zellerfeld, Germany: Trans Tech Publications.

Warren, J. (1999). **Evaporites: Their evolution and economics** (pp. 235-239). Philadelphia: Blackwell Science.

Yang, C. and Daemen, J. J. K. (1997). Temperature effects on creep of tuff and its time-dependent damage analysis. **International Journal of Rock Mechanics and Mining Sciences** 34 (3-4): 383-395.

Yavuz, H., Demirdag, S., and Caran, S. (2010). Thermal effect on the physical properties of carbonate rocks. **International Journal of Rock Mechanics and Mining Sciences** 47: 94-103.

APPENDIX

STRESS-STRAIN CURVES

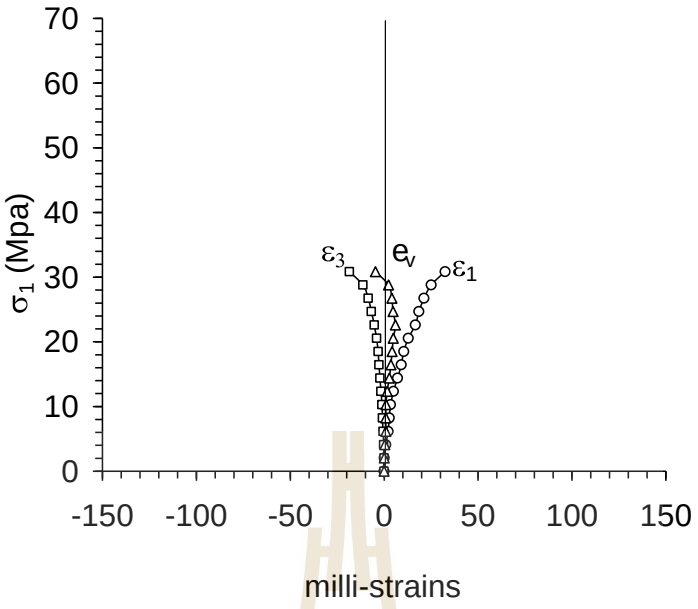

Figure A-1 Stress-strain curves of salt tested under σ_2 temperatures = σ_3 = 0 MPa, $\partial\sigma_1/\partial t$ = 0.1MPa/s and temperatures is 303 K.

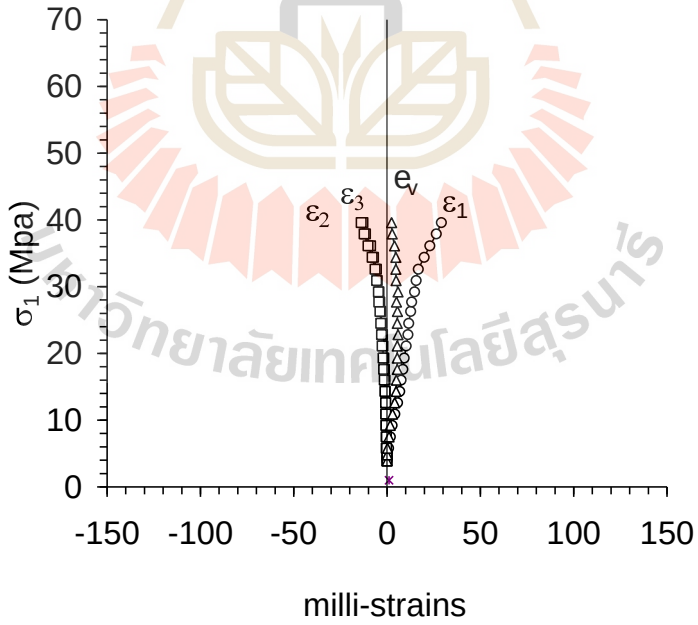

Figure A-2 Stress-strain curves of salt tested under σ_2 temperatures = σ_3 = 3 MPa, $\partial\sigma_1/\partial t$ = 0.1MPa/s and temperatures is 303 K.

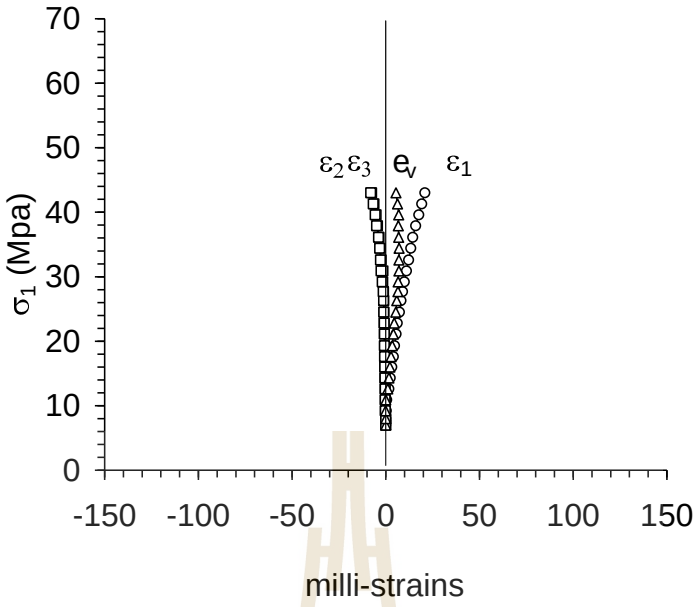

Figure A-3 Stress-strain curves of salt tested under σ_2 temperatures = σ_3 = 7 MPa, $\partial\sigma_1/\partial t$ = 0.1MPa/s and temperatures is 303 K.

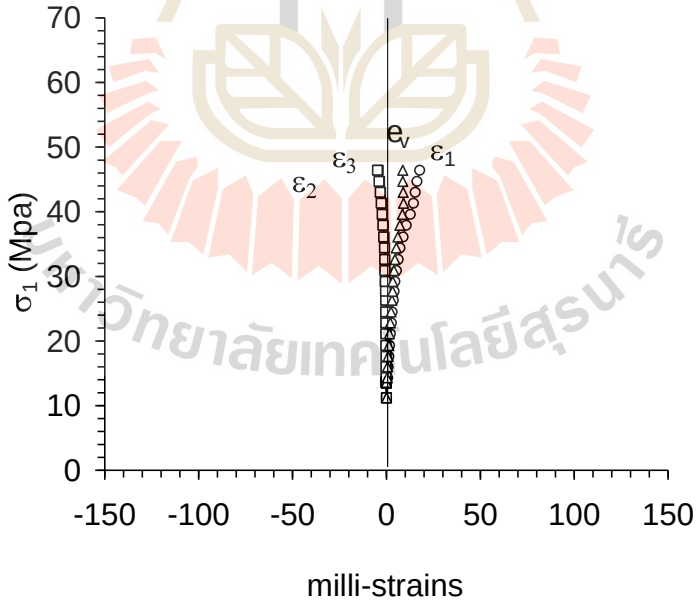

Figure A-4 Stress-strain curves of salt tested under σ_2 temperatures = σ_3 = 12 MPa, $\partial\sigma_1/\partial t$ = 0.1MPa/s and temperatures is 303 K.

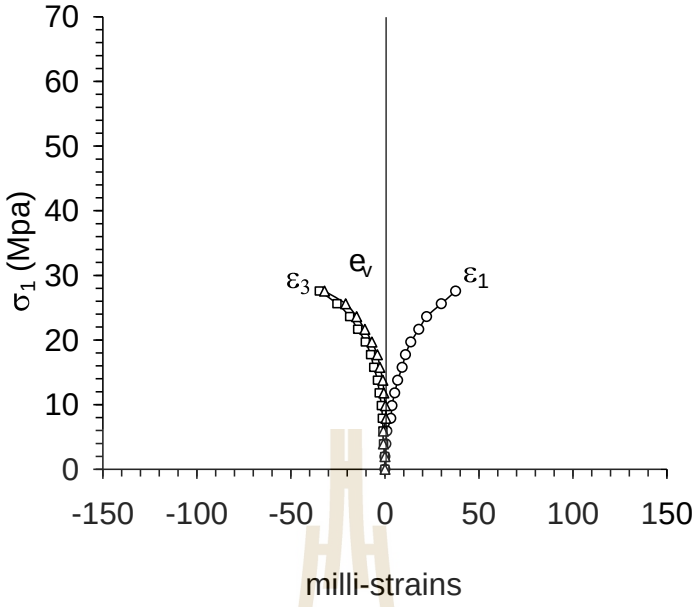

Figure A-5 Stress-strain curves of salt tested under σ_2 temperatures = σ_3 = 0 MPa, $\partial\sigma_1/\partial t$ = 0.01MPa/s and temperatures is 303 K.

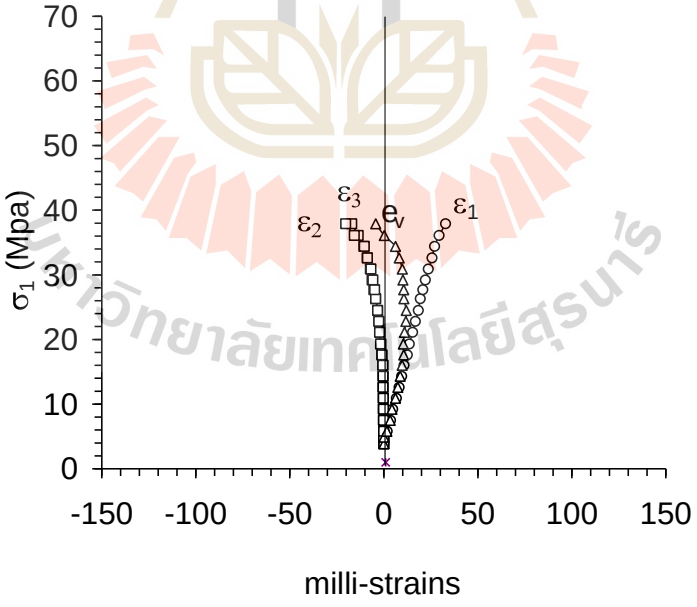

Figure A-6 Stress-strain curves of salt tested under σ_2 temperatures = σ_3 = 3 MPa, $\partial\sigma_1/\partial t$ = 0.01MPa/s and temperatures is 303 K.

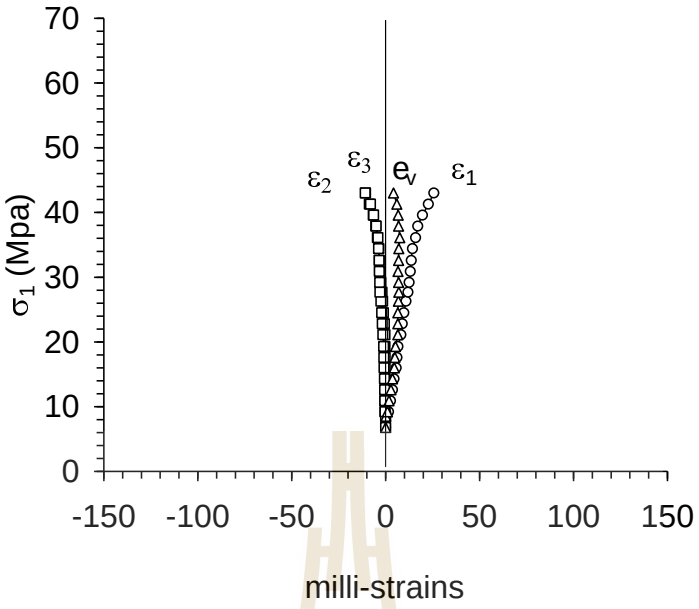

Figure A-7 Stress-strain curves of salt tested under σ_2 temperatures = σ_3 = 7 MPa, $\partial\sigma_1/\partial t$ = 0.01MPa/s and temperatures is 303 K.

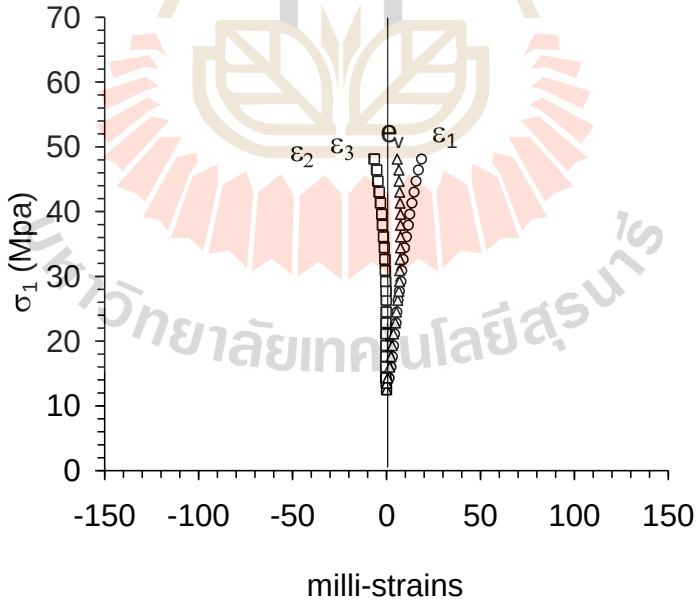

Figure A-8 Stress-strain curves of salt tested under σ_2 temperatures = σ_3 = 12 MPa, $\partial\sigma_1/\partial t$ = 0.01MPa/s and temperatures is 303 K.

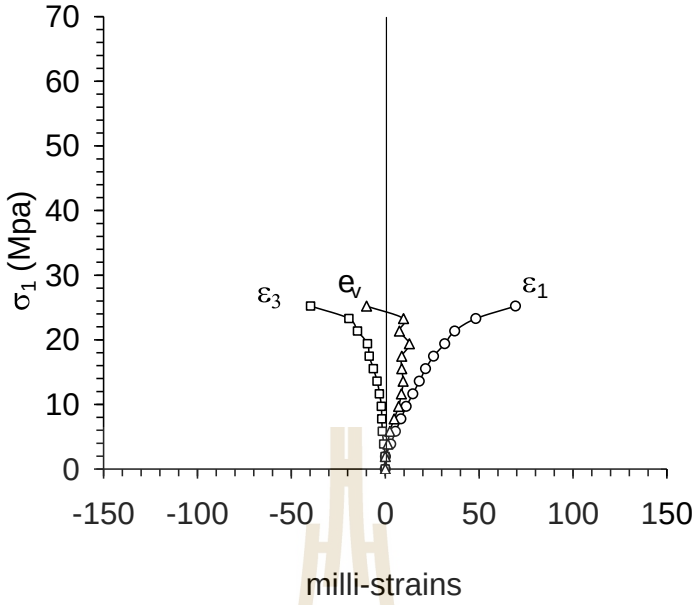

Figure A-9 Stress-strain curves of salt tested under σ_2 temperatures = σ_3 = 0 MPa, $\partial\sigma_1/\partial t$ = 0.001MPa/s and temperatures is 303 K.

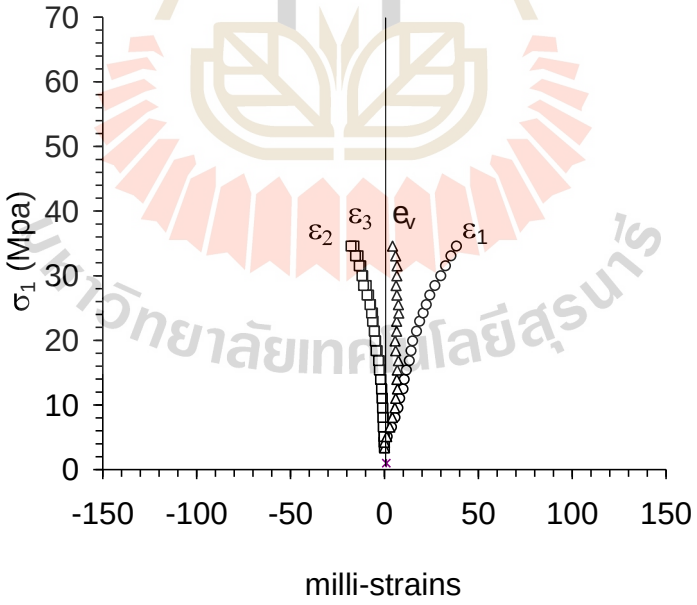

Figure A-10 Stress-strain curves of salt tested under σ_2 temperatures = σ_3 = 3 MPa, $\partial\sigma_1/\partial t$ = 0.001MPa/s and temperatures is 303 K.

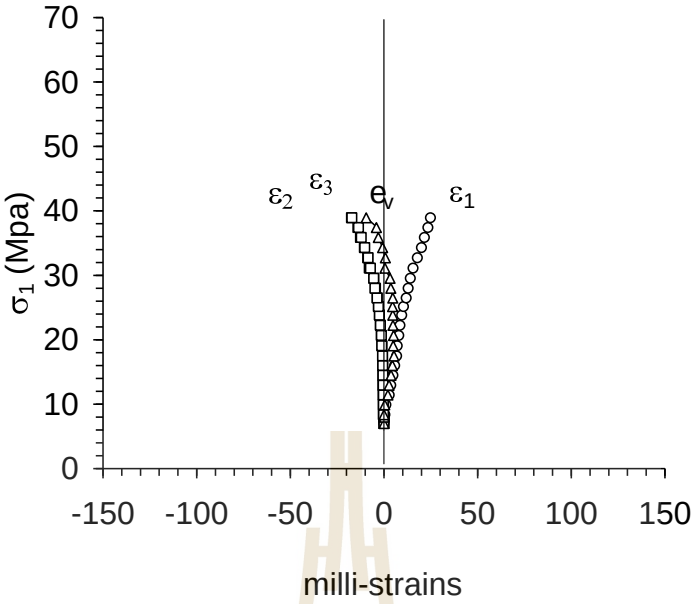

Figure A-11 Stress-strain curves of salt tested under σ_2 temperatures = σ_3 = 7MPa, $\partial\sigma_1/\partial t$ = 0.001MPa/s and temperatures is 303 K.

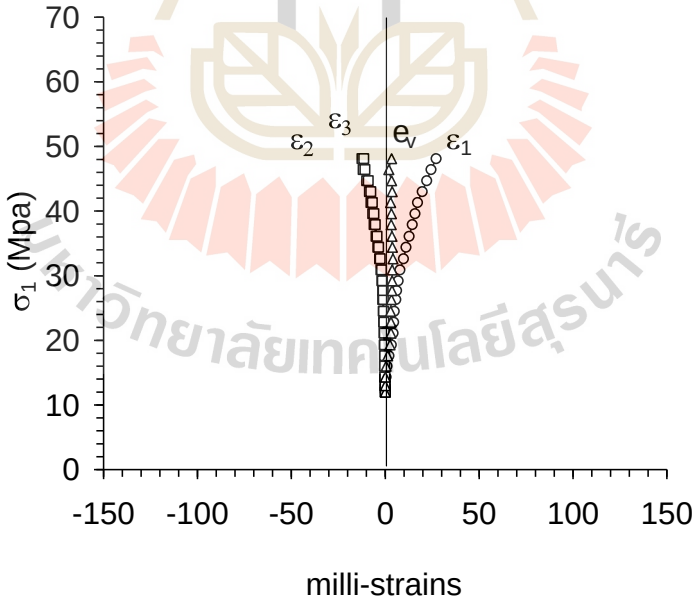

Figure A-12 Stress-strain curves of salt tested under σ_2 temperatures = σ_3 = 12 MPa, $\partial\sigma_1/\partial t$ = 0.001MPa/s and temperatures is 303 K.

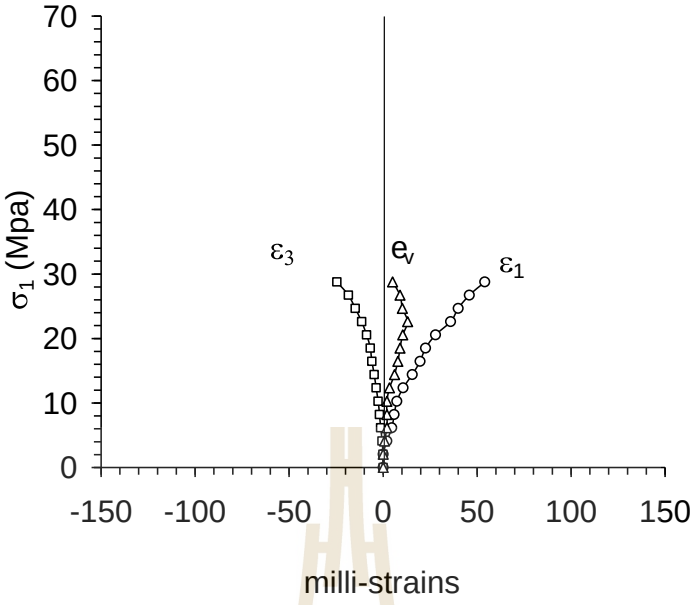

Figure A-13 Stress-strain curves of salt tested under σ_2 temperatures = σ_3 = 0 MPa, $\partial\sigma_1/\partial t$ = 0.1MPa/s and temperatures is 343 K.

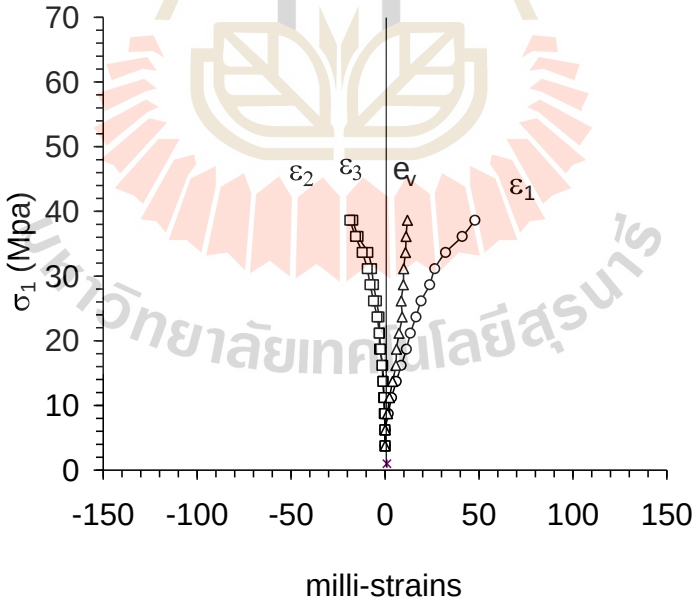

Figure A-14 Stress-strain curves of salt tested under σ_2 temperatures = σ_3 = 3 MPa, $\partial\sigma_1/\partial t$ = 0.1MPa/s and temperatures is 343 K.

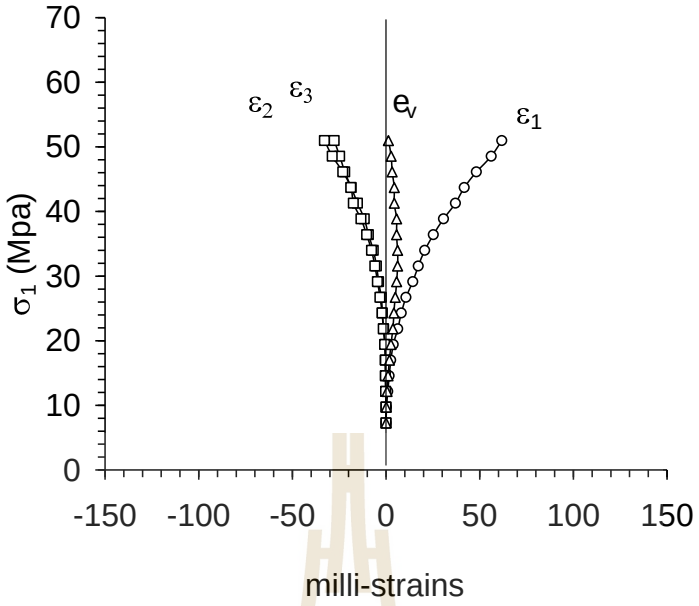

Figure A-15 Stress-strain curves of salt tested under σ_2 temperatures = σ_3 = 7 MPa, $\partial\sigma_1/\partial t$ = 0.1MPa/s and temperatures is 343 K.

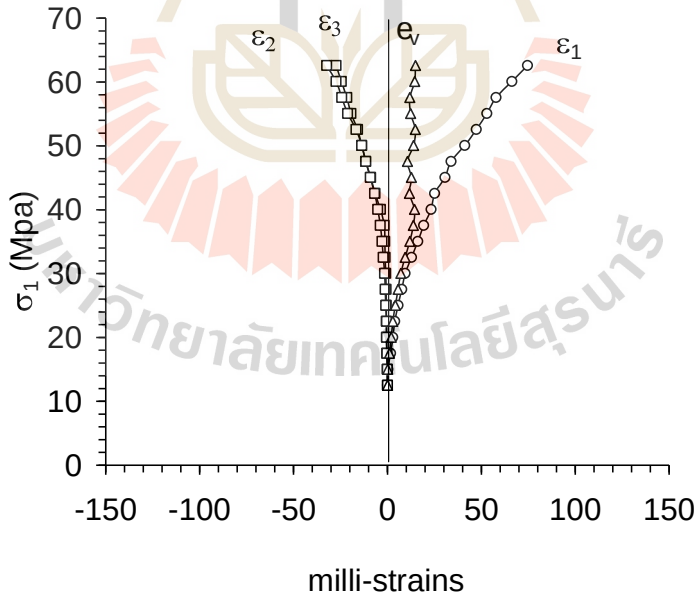

Figure A-16 Stress-strain curves of salt tested under σ_2 temperatures = σ_3 = 12 MPa, $\partial\sigma_1/\partial t$ = 0.1MPa/s and temperatures is 343 K.

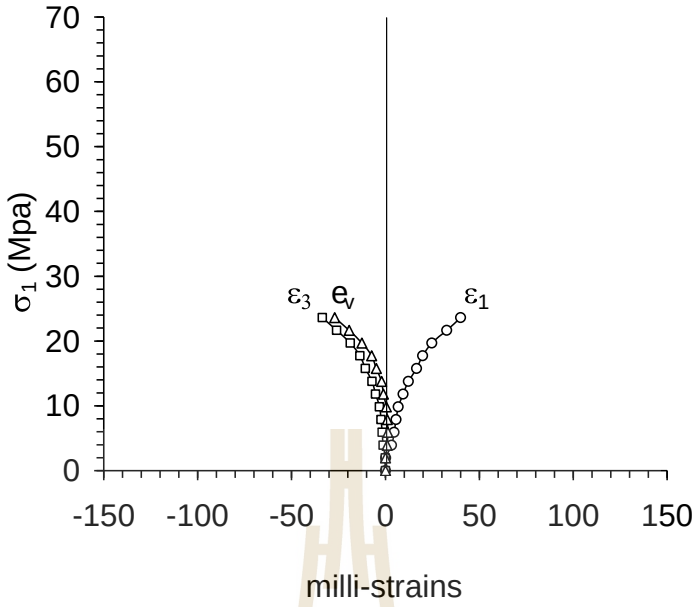

Figure A-17 Stress-strain curves of salt tested under σ_2 temperatures = σ_3 = 0 MPa, $\partial\sigma_1/\partial t$ = 0.01MPa/s and temperatures is 343 K.

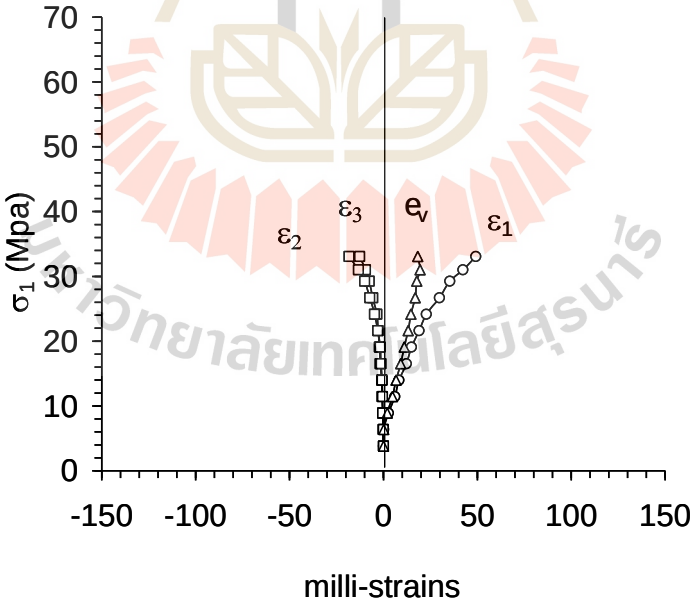

Figure A-18 Stress-strain curves of salt tested under σ_2 temperatures = σ_3 = 3 MPa, $\partial\sigma_1/\partial t$ = 0.01MPa/s and temperatures is 343 K.

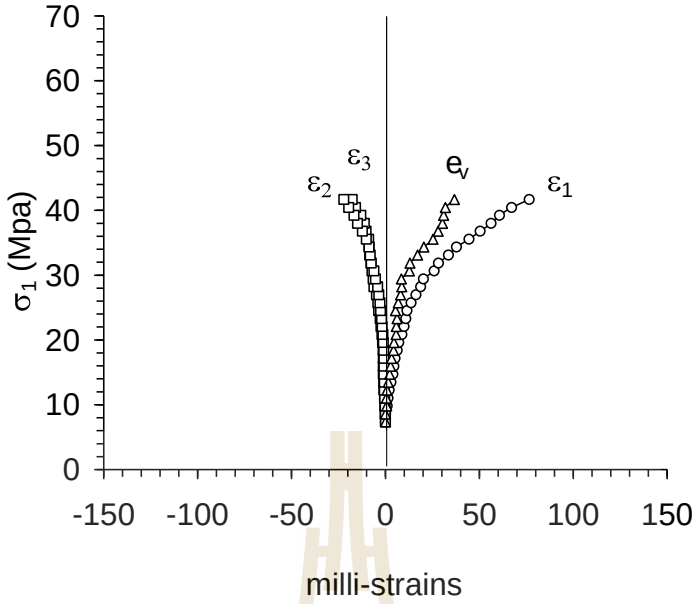

Figure A-19 Stress-strain curves of salt tested under σ_2 temperatures = σ_3 = 7 MPa, $\partial\sigma_1/\partial t$ = 0.01MPa/s and temperatures is 343 K.

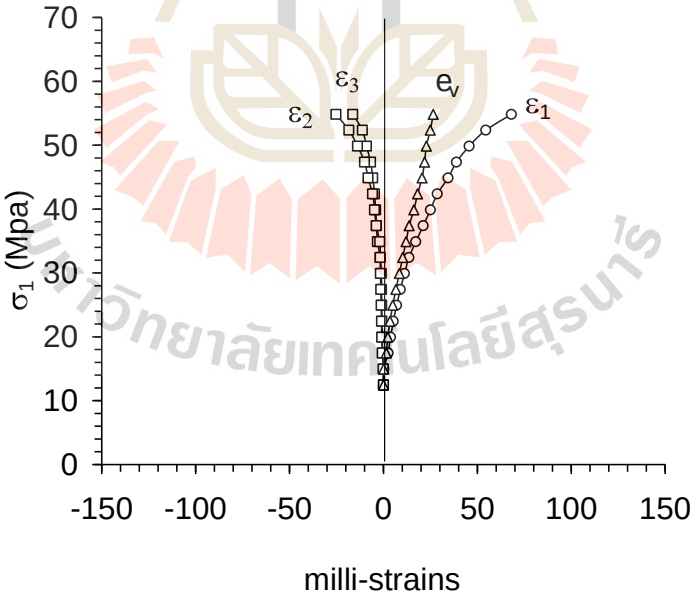

Figure A-20 Stress-strain curves of salt tested under σ_2 temperatures = σ_3 = 12 MPa, $\partial\sigma_1/\partial t$ = 0.01MPa/s and temperatures is 343 K.

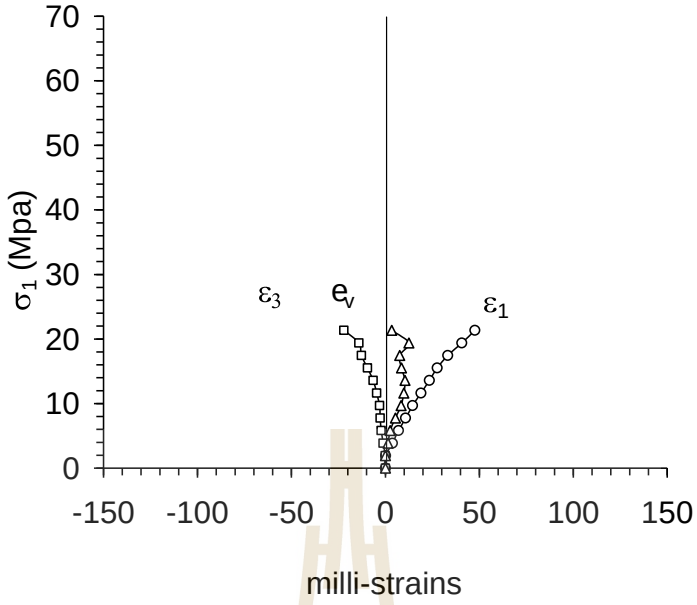

Figure A-21 Stress-strain curves of salt tested under σ_2 temperatures = σ_3 = 0 MPa, $\partial\sigma_1/\partial t$ = 0.001MPa/s and temperatures is 343 K.

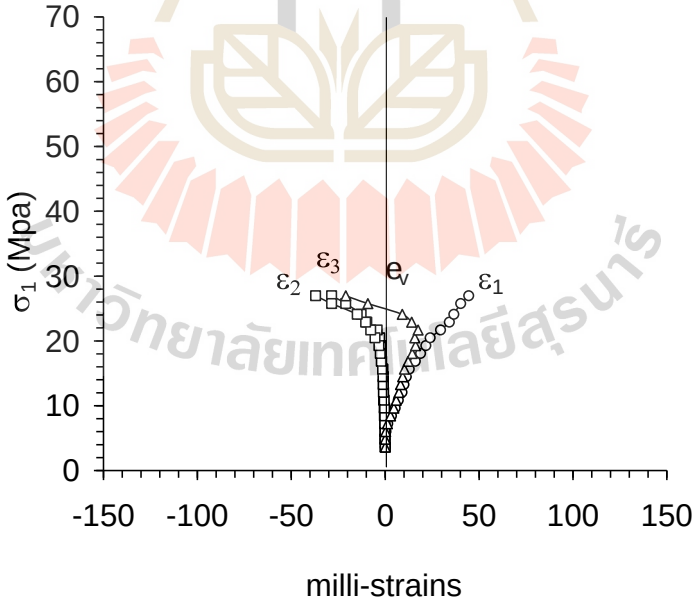

Figure A-22 Stress-strain curves of salt tested under σ_2 temperatures = σ_3 = 3 MPa, $\partial\sigma_1/\partial t$ = 0.001MPa/s and temperatures is 343 K.

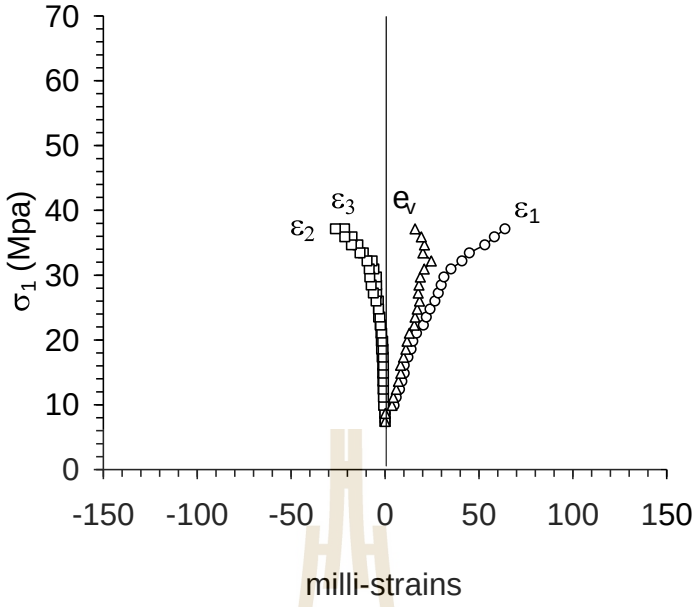

Figure A-23 Stress-strain curves of salt tested under σ_2 temperatures = σ_3 = 7 MPa, $\partial\sigma_1/\partial t$ = 0.001MPa/s and temperatures is 343 K.

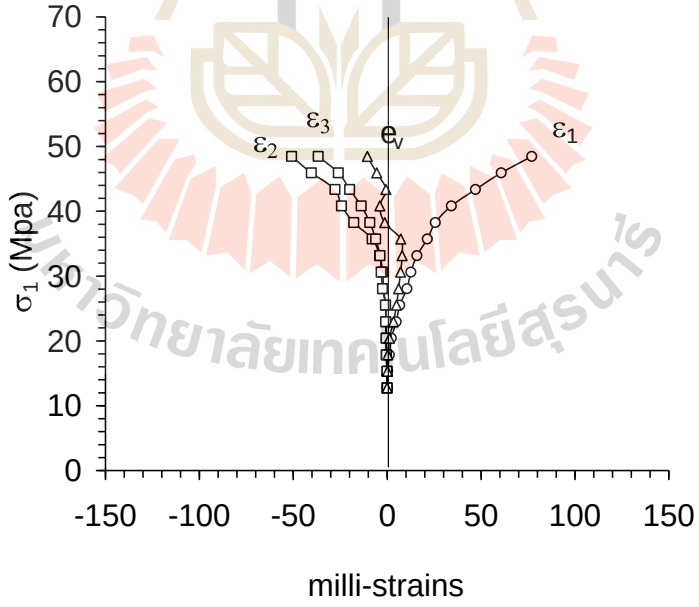

Figure A-24 Stress-strain curves of salt tested under σ_2 temperatures = σ_3 = 12 MPa, $\partial\sigma_1/\partial t$ = 0.001MPa/s and temperatures is 343 K.

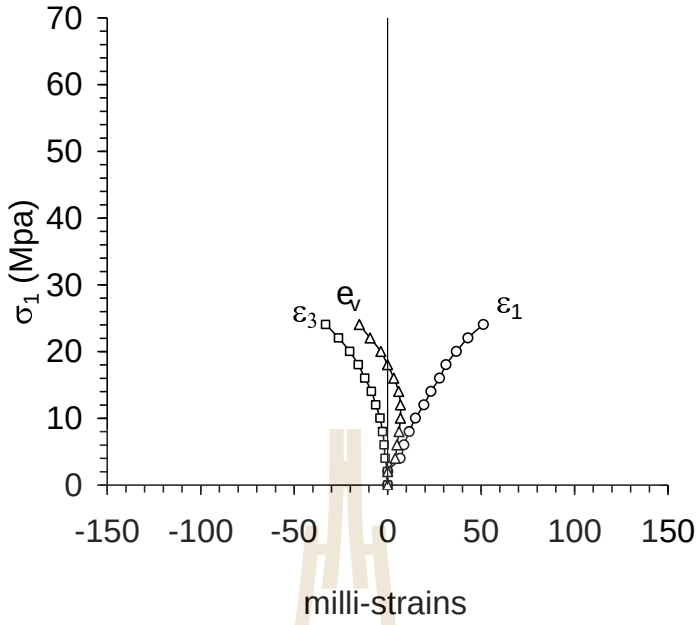

Figure A-25 Stress-strain curves of salt tested under σ_2 temperatures = σ_3 = 0 MPa, $\partial\sigma_1/\partial t$ = 0.1MPa/s and temperatures is 373 K.

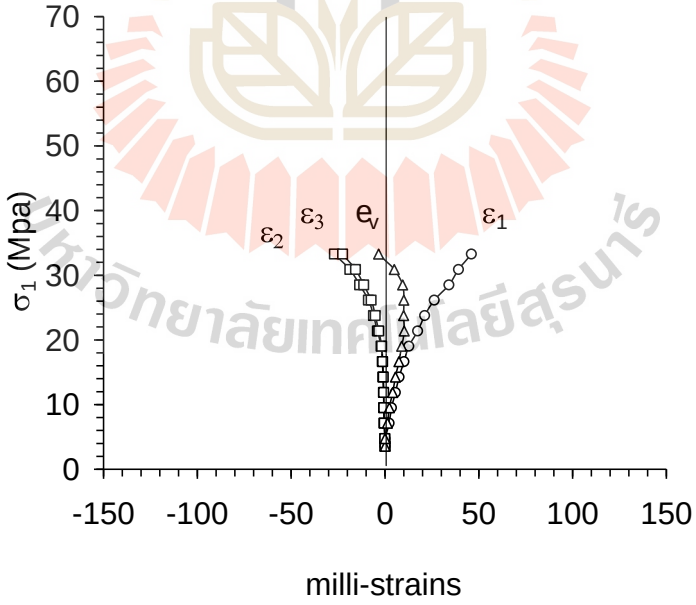

Figure A-26 Stress-strain curves of salt tested under σ_2 temperatures = σ_3 = 3 MPa, $\partial\sigma_1/\partial t$ = 0.1MPa/s and temperatures is 373 K.

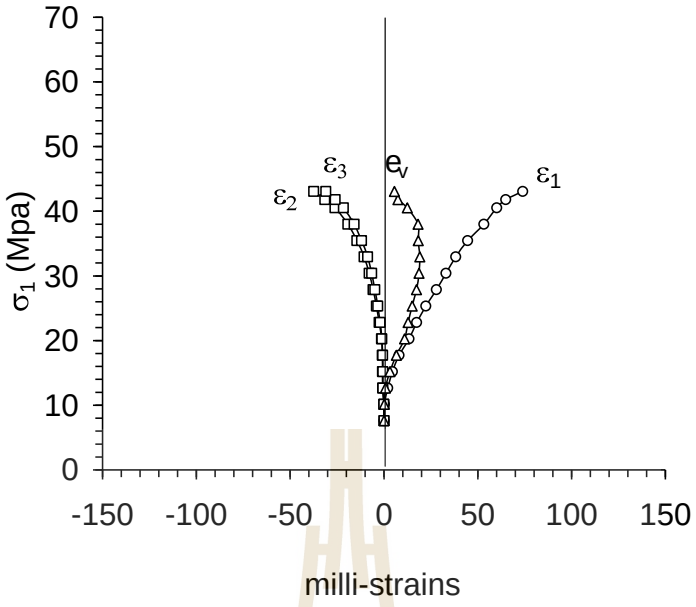

Figure A-27 Stress-strain curves of salt tested under σ_2 temperatures = σ_3 = 7 MPa, $\partial\sigma_1/\partial t$ = 0.1MPa/s and temperatures is 373 K.

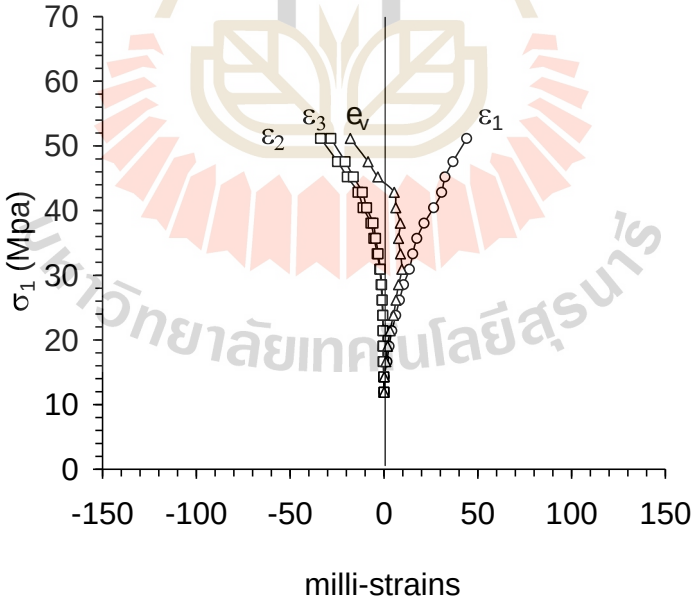

Figure A-28 Stress-strain curves of salt tested under σ_2 temperatures = σ_3 = 12 MPa, $\partial\sigma_1/\partial t$ = 0.1MPa/s and temperatures is 373 K.

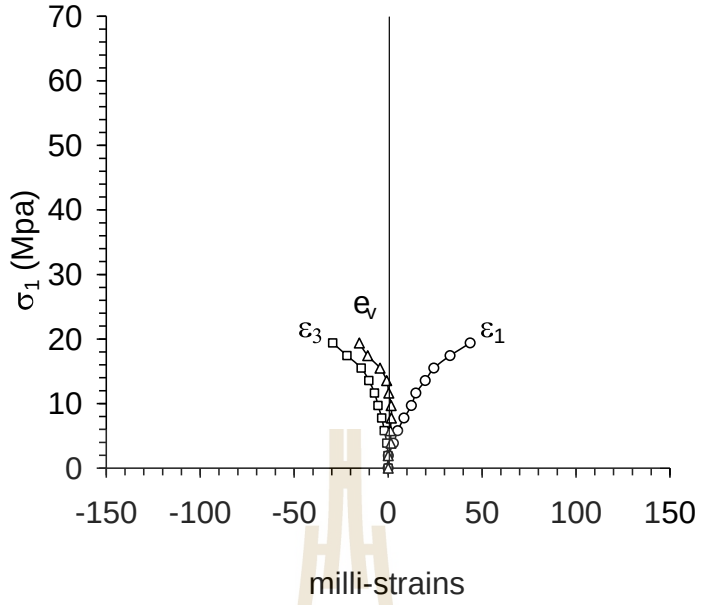

Figure A-29 Stress-strain curves of salt tested under σ_2 temperatures = σ_3 = 0 MPa, $\partial\sigma_1/\partial t$ = 0.01MPa/s and temperatures is 373 K.

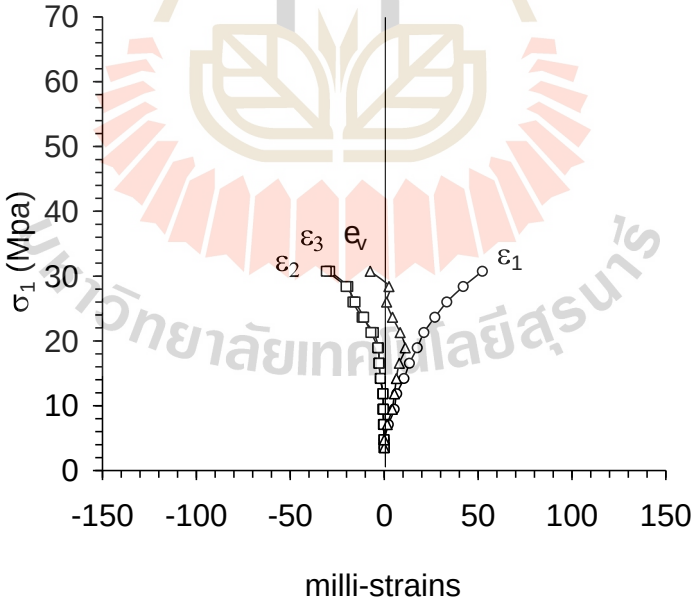

Figure A-30 Stress-strain curves of salt tested under σ_2 temperatures = σ_3 = 3 MPa, $\partial\sigma_1/\partial t$ = 0.01MPa/s and temperatures is 373 K.

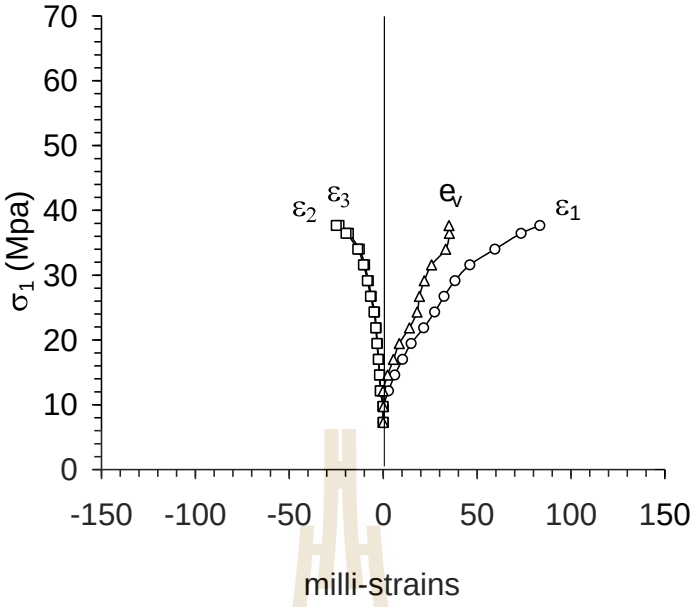

Figure A-31 Stress-strain curves of salt tested under σ_2 temperatures = σ_3 = 7 MPa, $\partial\sigma_1/\partial t$ = 0.01MPa/s and temperatures is 373 K.

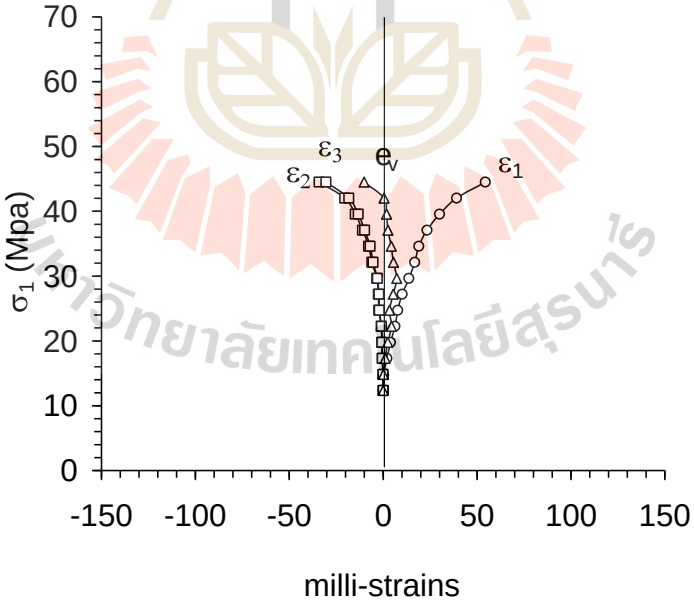

Figure A-32 Stress-strain curves of salt tested under σ_2 temperatures = σ_3 = 12 MPa, $\partial\sigma_1/\partial t$ = 0.01MPa/s and temperatures is 373 K.

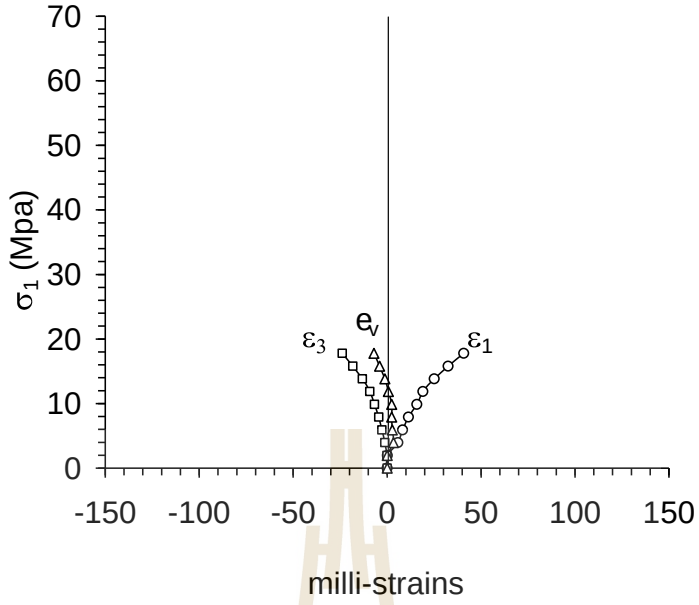

Figure A-33 Stress-strain curves of salt tested under σ_2 temperatures = σ_3 = 0 MPa, $\partial\sigma_1/\partial t$ = 0.001MPa/s and temperatures is 373 K.

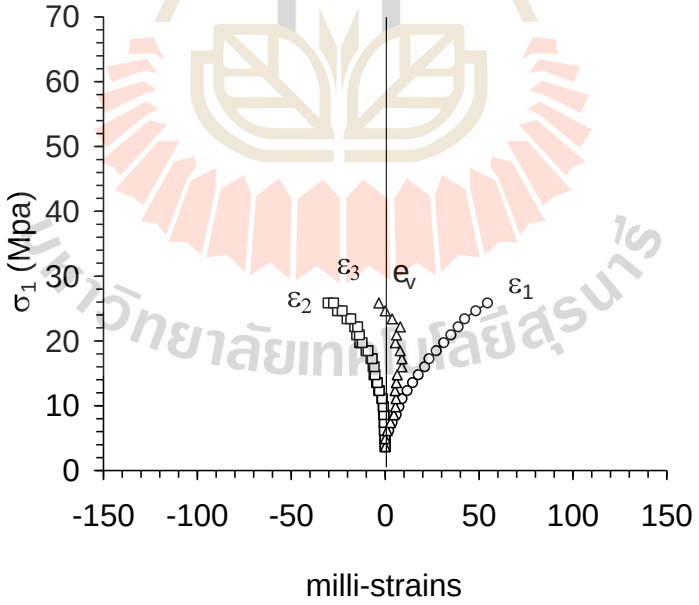

Figure A-34 Stress-strain curves of salt tested under σ_2 temperatures = σ_3 = 3 MPa, $\partial\sigma_1/\partial t$ = 0.001MPa/s and temperatures is 373 K.

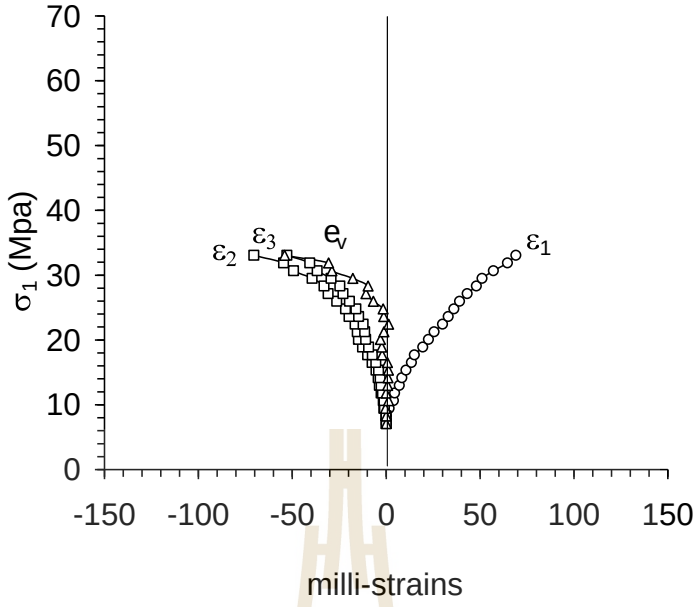

Figure A-35 Stress-strain curves of salt tested under σ_2 temperatures = σ_3 = 7 MPa, $\partial\sigma_1/\partial t$ = 0.001MPa/s and temperatures is 373 K.

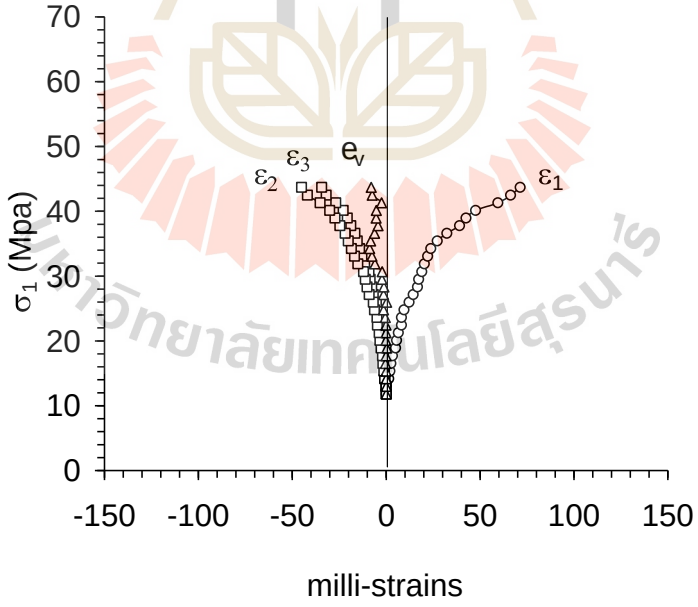

Figure A-36 Stress-strain curves of salt tested under σ_2 temperatures = σ_3 = 12 MPa, $\partial\sigma_1/\partial t$ = 0.001MPa/s and temperatures is 373 K.

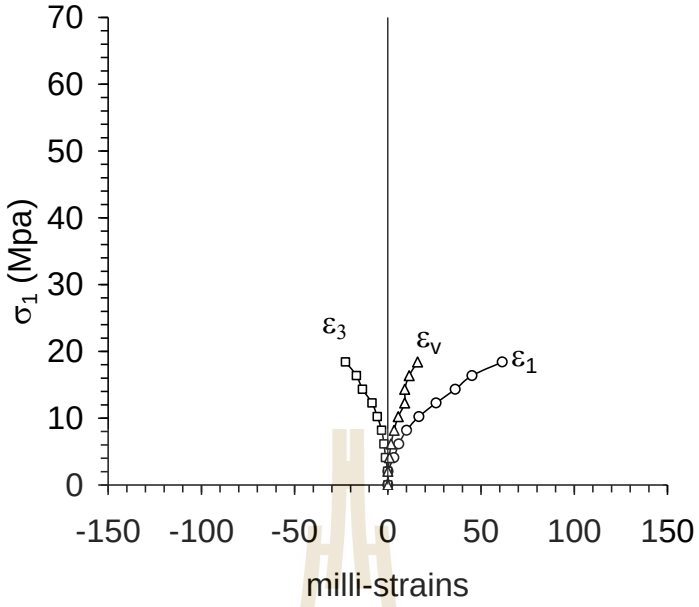

Figure A-37 Stress-strain curves of salt tested under σ_2 temperatures = σ_3 = 0 MPa, $\partial\sigma_1/\partial t$ = 0.1MPa/s and temperatures is 423 K.

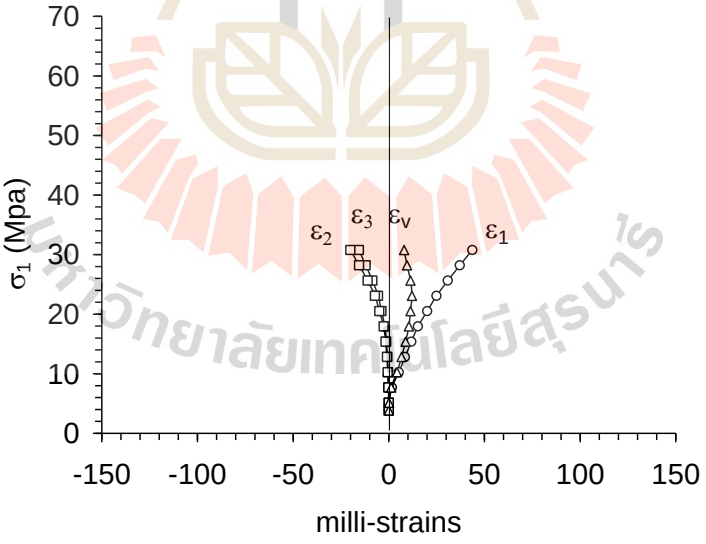

Figure A-38 Stress-strain curves of salt tested under σ_2 temperatures = σ_3 = 3 MPa, $\partial\sigma_1/\partial t$ = 0.1MPa/s and temperatures is 423 K.

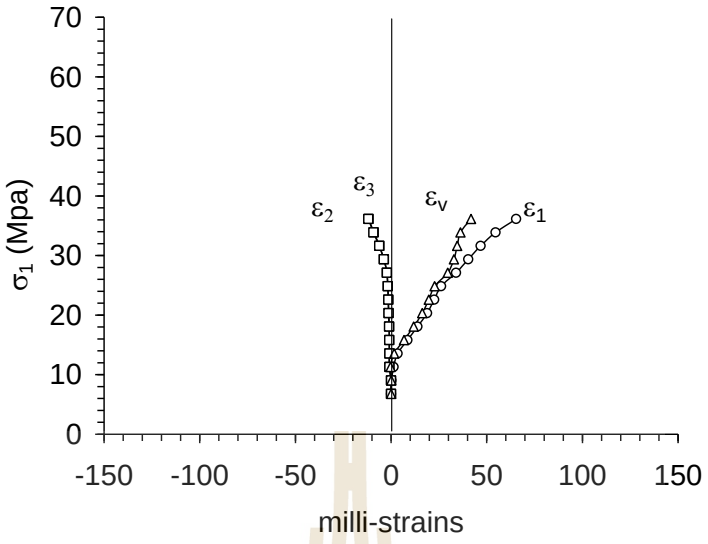

Figure A-39 Stress-strain curves of salt tested under σ_2 temperatures = σ_3 = 7 MPa, $\partial\sigma_1/\partial t$ = 0.1MPa/s and temperatures is 423 K.

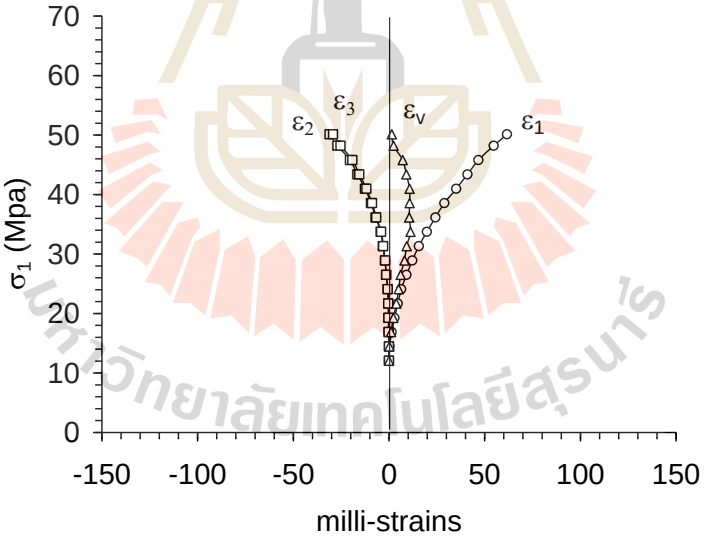

Figure A-40 Stress-strain curves of salt tested under σ_2 temperatures = σ_3 = 12 MPa, $\partial\sigma_1/\partial t$ = 0.1MPa/s and temperatures is 423 K.

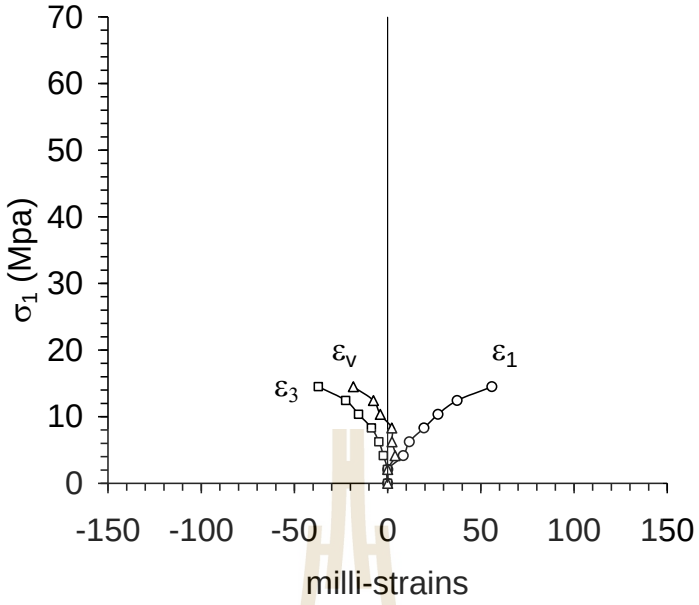

Figure A-41 Stress-strain curves of salt tested under σ_2 temperatures = σ_3 = 0 MPa, $\partial\sigma_1/\partial t$ = 0.01MPa/s and temperatures is 423 K.

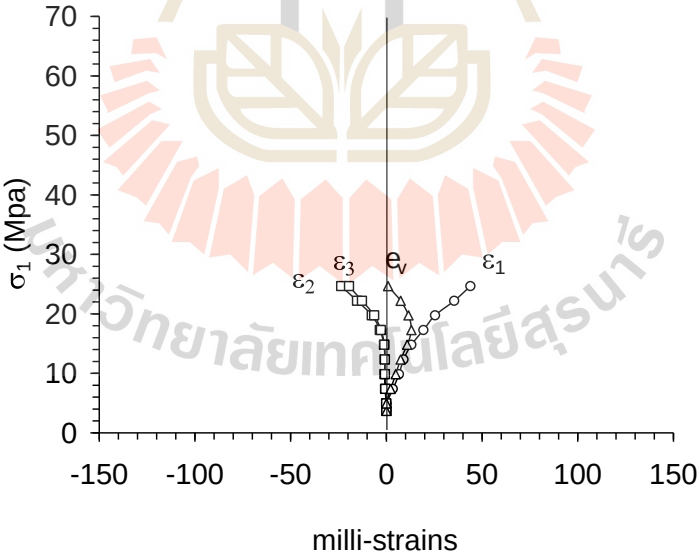

Figure A-42 Stress-strain curves of salt tested under σ_2 temperatures = σ_3 = 3 MPa, $\partial\sigma_1/\partial t$ = 0.01MPa/s and temperatures is 423 K.

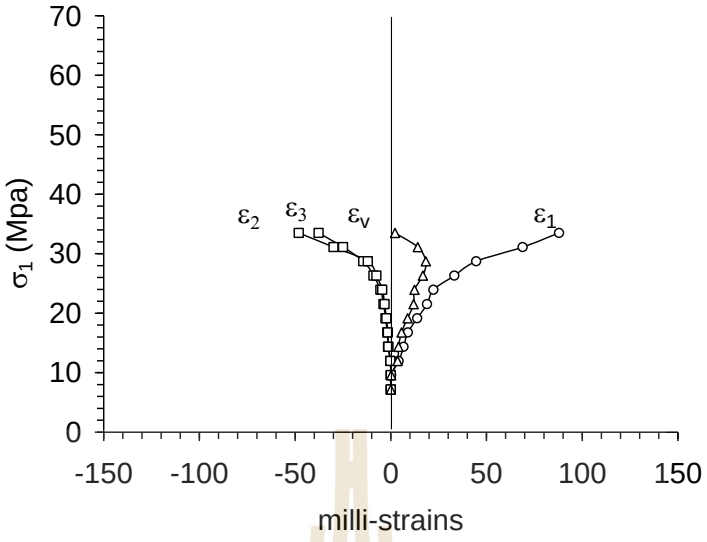

Figure A-43 Stress-strain curves of salt tested under σ_2 temperatures = σ_3 = 7 MPa, $\partial\sigma_1/\partial t$ = 0.01MPa/s and temperatures is 423 K.

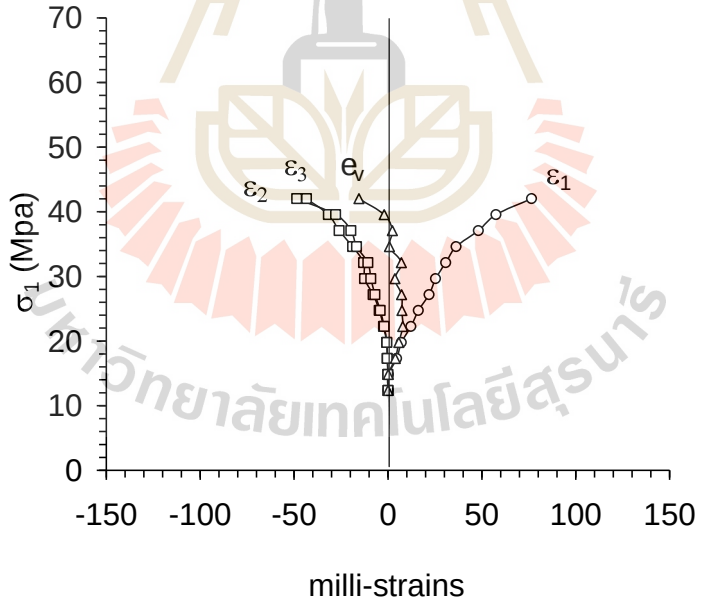

Figure A-44 Stress-strain curves of salt tested under σ_2 temperatures = σ_3 = 12 MPa, $\partial\sigma_1/\partial t$ = 0.01MPa/s and temperatures is 423 K.

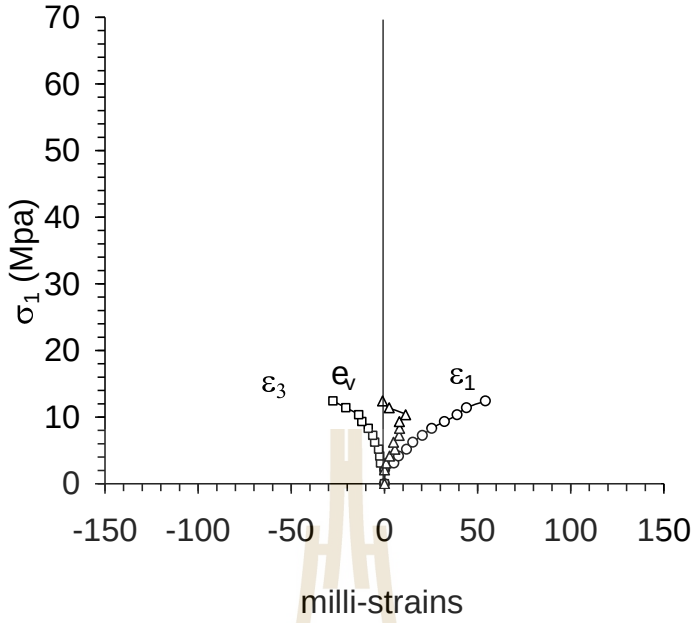

Figure A-45 Stress-strain curves of salt tested under σ_2 temperatures = σ_3 = 0 MPa, $\partial\sigma_1/\partial t$ = 0.001MPa/s and temperatures is 423 K.

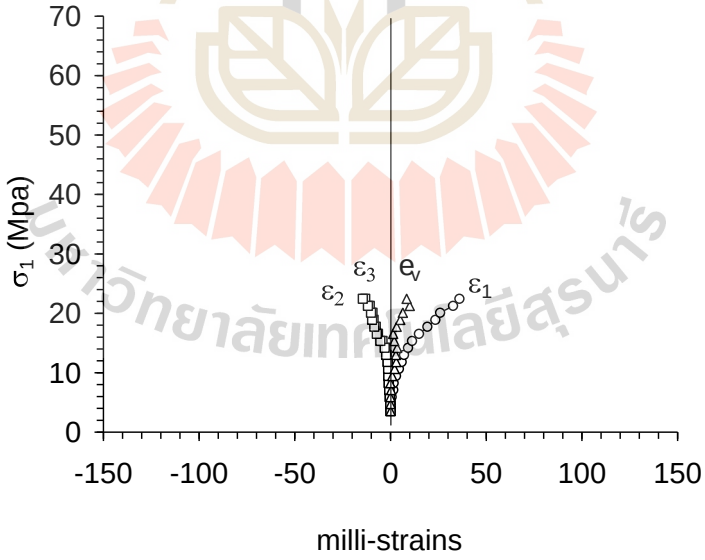

Figure A-46 Stress-strain curves of salt tested under σ_2 temperatures = σ_3 = 3 MPa, $\partial\sigma_1/\partial t$ = 0.001MPa/s and temperatures is 423 K.

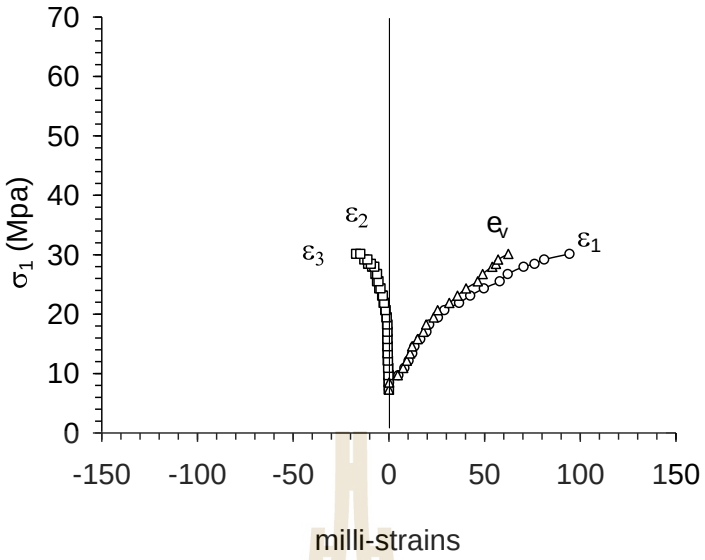

Figure A-47 Stress-strain curves of salt tested under σ_2 temperatures = σ_3 = 7 MPa, $\partial\sigma_1/\partial t$ = 0.001MPa/s and temperatures is 423 K.

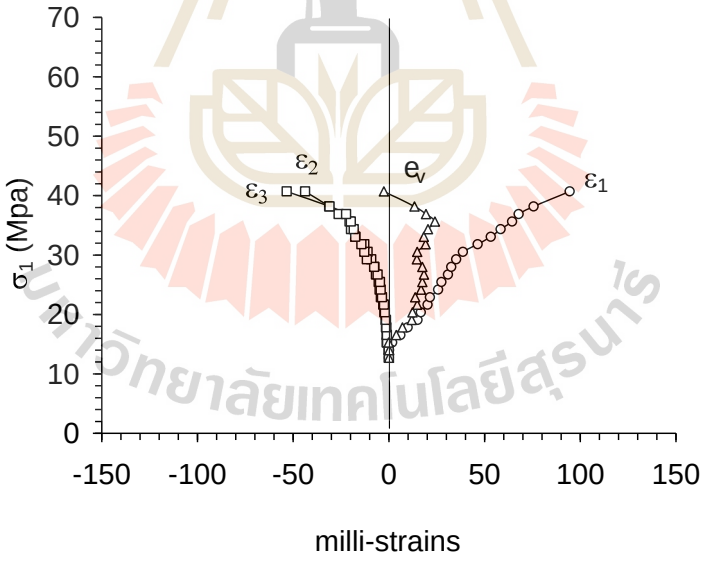

Figure A-48 Stress-strain curves of salt tested under σ_2 temperatures = σ_3 = 12 MPa, $\partial\sigma_1/\partial t$ = 0.001MPa/s and temperatures is 423 K.

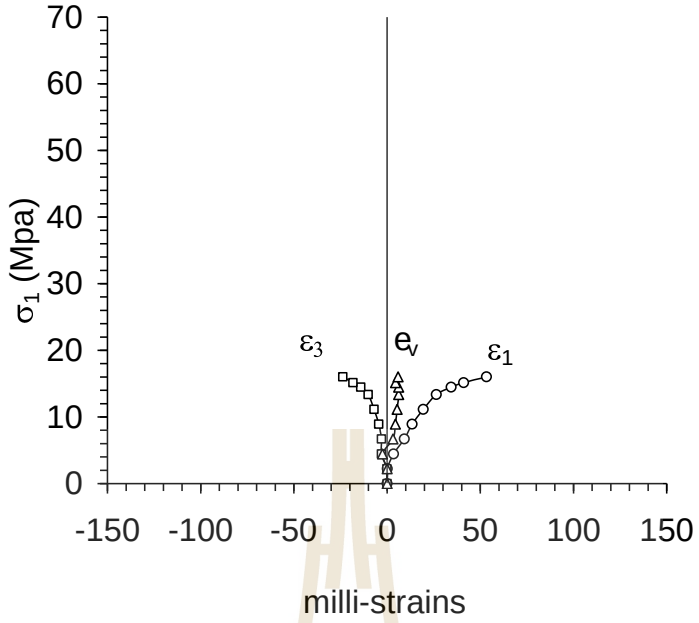

Figure A-49 Stress-strain curves of salt tested under σ_2 temperatures = σ_3 = 0 MPa, $\partial\sigma_1/\partial t$ = 0.1MPa/s and temperatures is 473 K.

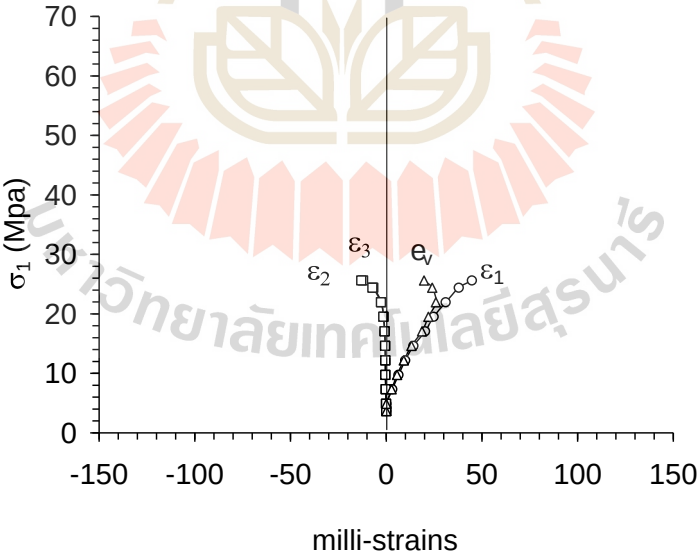

Figure A-50 Stress-strain curves of salt tested under σ_2 temperatures = σ_3 = 3 MPa, $\partial\sigma_1/\partial t$ = 0.1MPa/s and temperatures is 473 K.

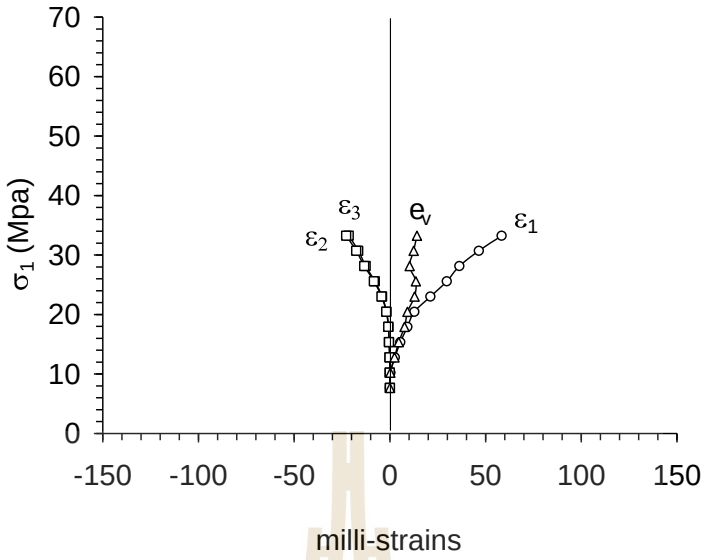

Figure A-51 Stress-strain curves of salt tested under σ_2 temperatures = σ_3 = 7 MPa, $\partial\sigma_1/\partial t$ = 0.1MPa/s and temperatures is 473 K.

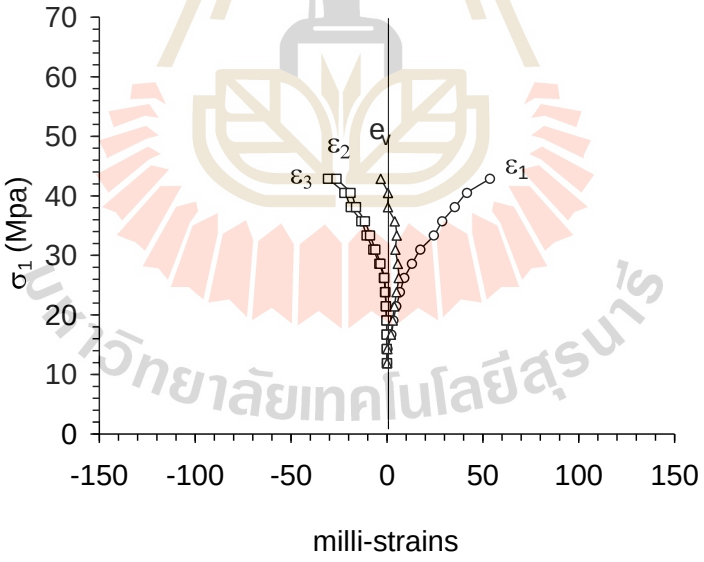

Figure A-52 Stress-strain curves of salt tested under σ_2 temperatures = σ_3 = 12 MPa, $\partial\sigma_1/\partial t$ = 0.1MPa/s and temperatures is 473 K.

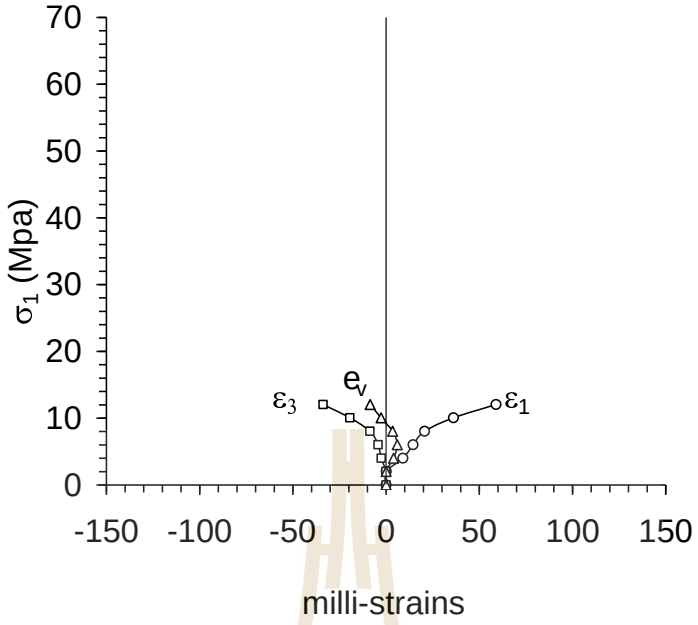

Figure A-53 Stress-strain curves of salt tested under σ_2 temperatures = σ_3 = 0 MPa, $\partial\sigma_1/\partial t$ = 0.01MPa/s and temperatures is 473 K.

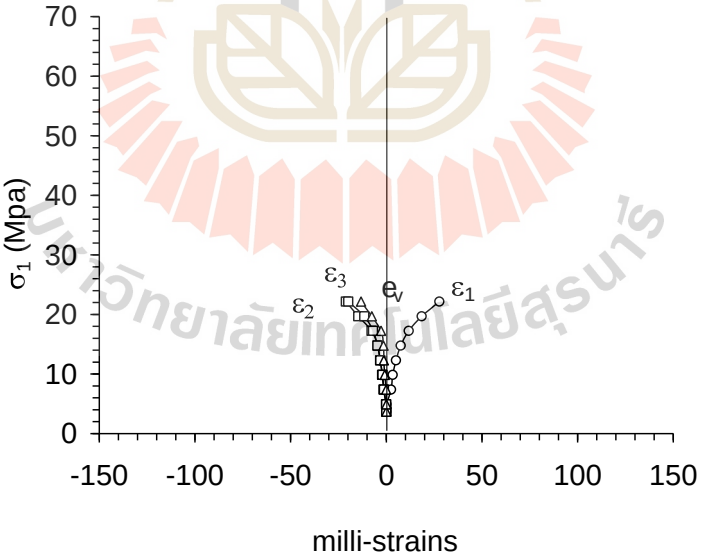

Figure A-54 Stress-strain curves of salt tested under σ_2 temperatures = σ_3 = 3 MPa, $\partial\sigma_1/\partial t$ = 0.01MPa/s and temperatures is 473 K.

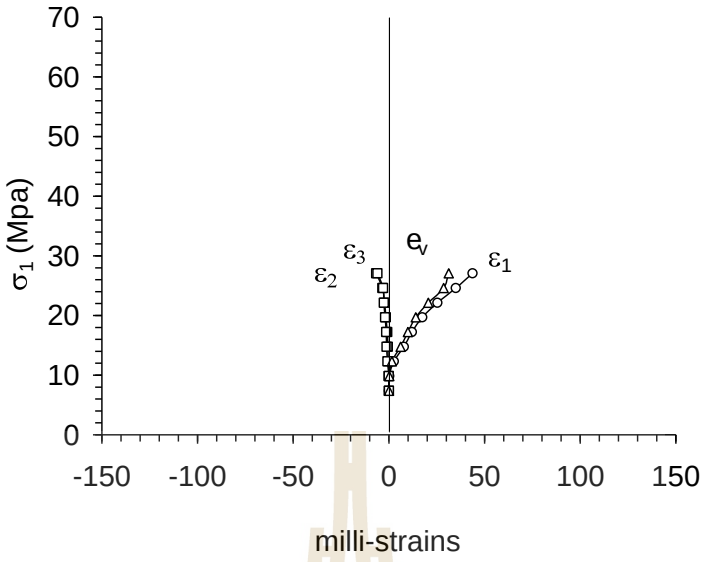

Figure A-55 Stress-strain curves of salt tested under σ_2 temperatures = σ_3 = 7 MPa, $\partial\sigma_1/\partial t$ = 0.01MPa/s and temperatures is 473 K.

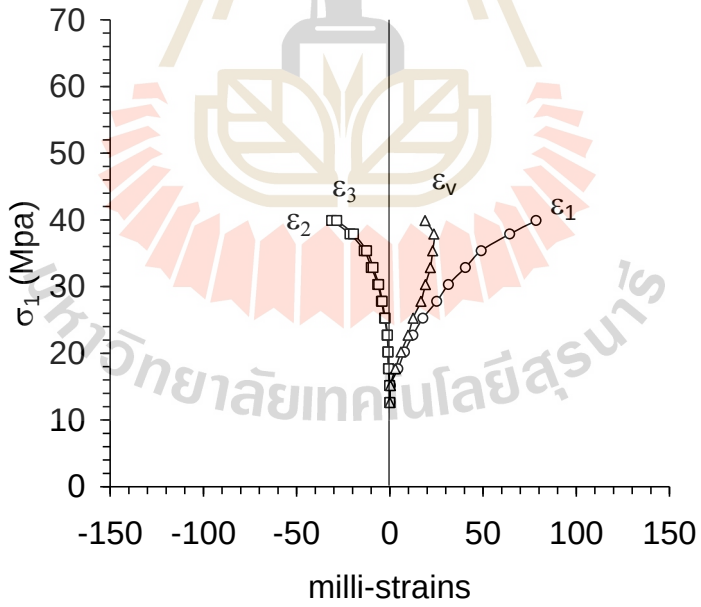

Figure A-56 Stress-strain curves of salt tested under σ_2 temperatures = σ_3 = 12 MPa, $\partial\sigma_1/\partial t$ = 0.01MPa/s and temperatures is 473 K.

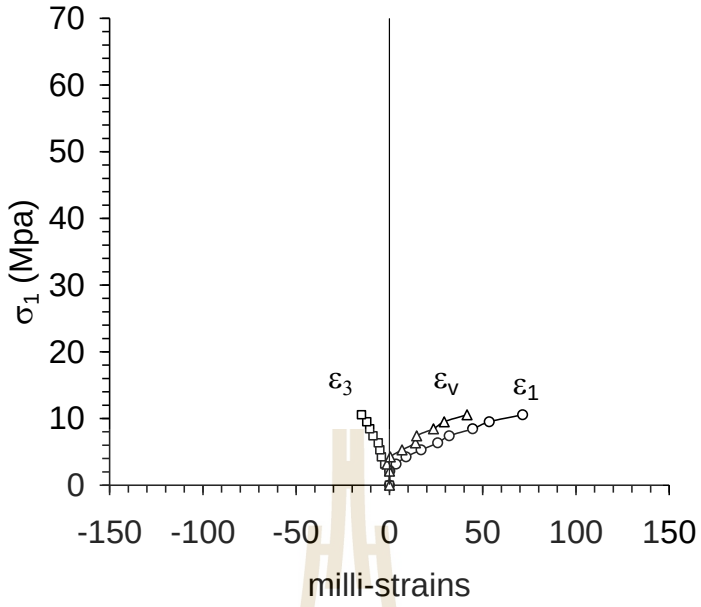

Figure A-57 Stress-strain curves of salt tested under σ_2 temperatures = σ_3 = 0 MPa, $\partial\sigma_1/\partial t$ = 0.001MPa/s and temperatures is 473 K.

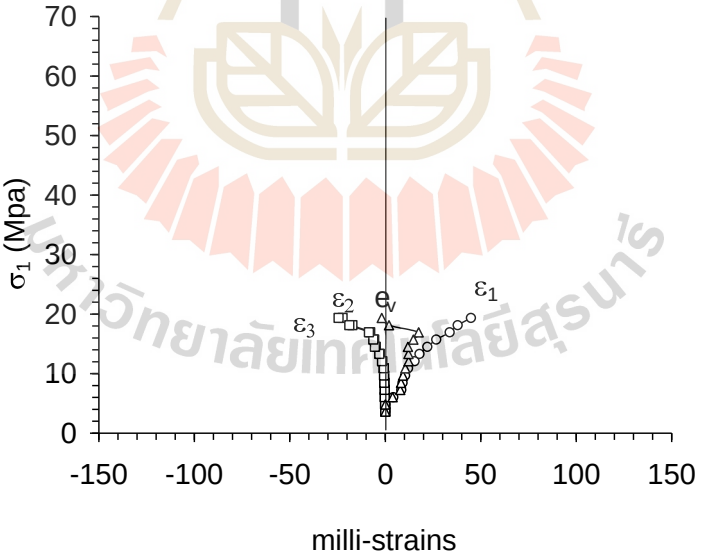

Figure A-58 Stress-strain curves of salt tested under σ_2 temperatures = σ_3 = 3 MPa, $\partial\sigma_1/\partial t$ = 0.001MPa/s and temperatures is 473 K.

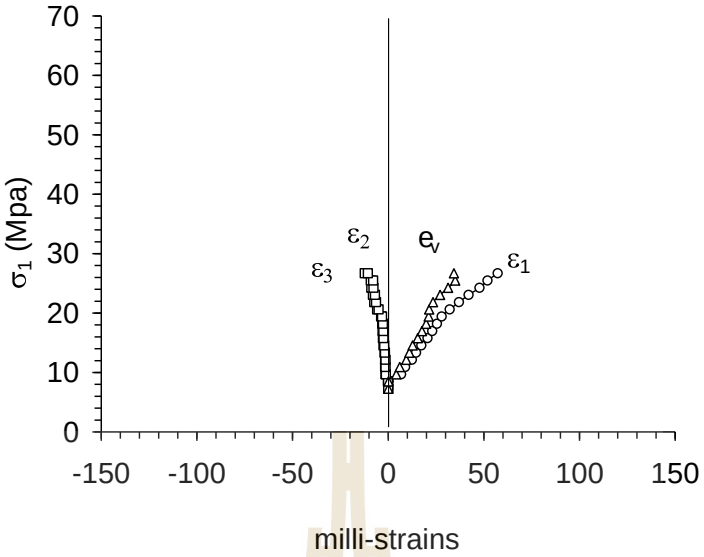

Figure A-59 Stress-strain curves of salt tested under σ_2 temperatures = σ_3 = 7 MPa, $\partial\sigma_1/\partial t$ = 0.001MPa/s and temperatures is 473 K.

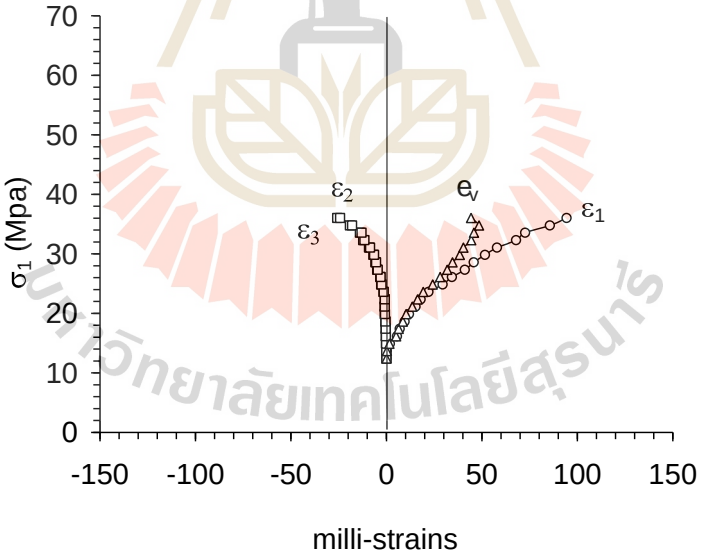

Figure A-60 Stress-strain curves of salt tested under σ_2 temperatures = σ_3 = 12 MPa, $\partial\sigma_1/\partial t$ = 0.001MPa/s and temperatures is 473 K.

BIOGRAPHY

Mr. Komkrit Phatthaisong was born on January 15, 1988 in Nakhon Ratchasima province, Thailand. He received his Bachelor's Degree in Engineering (Geotechnology) from Suranaree University of Technology in 2009 and Master's degree in 2011. After that, he continued to study with Philosophy's degree in the Geological Engineering Program, Institute of Engineering, Suranaree University of Technology. During graduation, 2011-2015, he was a part time worker in position of research assistant at the Geomechanics Resaerch Unit, Institute of Engineering, Suranaree University of Technology.